

Factors influencing the uptake and fate of metallic nanoparticles in filter-feeding bivalves

Matthew Scott Hull

Dissertation submitted to the faculty of the Virginia Polytechnic Institute and State University in
partial fulfillment of the requirements for the degree of

Doctor of Philosophy
In
Civil and Environmental Engineering

Peter J. Vikesland (Committee Chair)
Nancy G. Love (Committee Co-Chair)
Michael F. Hochella, Jr.
Linsey C. Marr
Madeline E. Schreiber

August 11, 2011
Blacksburg, VA 24061

Keywords: *Corbicula fluminea*, gold nanoparticles, iron nanoparticles, nanomaterials,
nanotechnology, filter-feeders, aquatic biota, persistence, fate and transport, quantum dots, iron
nanoparticles

Copyright © 2011 Matthew S. Hull

Factors influencing the uptake and fate of metallic nanoparticles in filter-feeding bivalves

Matthew Scott Hull

ABSTRACT

Metallic nanoparticles (MetNPs) with unique nanoscale properties, including novel optical behavior and superparamagnetism, are continually being developed for biomedical and industrial applications. In certain biomedical applications where extended blood half-lives are required, MetNPs are surface-functionalized using polymers, proteins, and other stabilizing agents to facilitate their resistance to salt-induced aggregation. Given their colloidal stability in high ionic-strength matrices, functionalized MetNPs are anticipated to be persistent aquatic contaminants. Despite their potential environmental significance, the persistence of surface-functionalized MetNPs as individually-stabilized nanoparticles in aquatic environments is largely unknown. Further, few studies have investigated the fundamental factors that influence MetNP uptake and fate/transport processes in ecologically susceptible aquatic biota, such as filter-feeding bivalves, which ingest and accumulate a broad range of dissolved- and particulate-phase contaminants.

The present study describes a comprehensive approach to prepare and rigorously characterize MetNP test suspensions to facilitate fundamental examinations of nanoparticle uptake and fate/transport processes in freshwater and marine bivalves. We demonstrate the importance of accurately characterizing test suspensions in order to better understand MetNP persistence as individually-stabilized nanoparticles within aquatic test media, and define an optical-activity metric suitable for quantifying and comparing the persistence of variable MetNP formulations as National Nanotechnology Initiative (NNI) definable nanoscale materials. We also show that individually-stabilized MetNPs of variable elemental composition, particle

diameter, and surface coating are accessible to bivalves in both freshwater and marine environments. Clearance rates for MetNPs are positively related to the diameter and initial concentration of MetNP suspensions. The observed size-dependence of particle filtration rates facilitates ‘size-selective biopurification’ of particle suspensions with nanoscale resolution, and may have applicability in future sustainable nanomanufacturing processes. Filtered MetNPs are retained for extended periods post-exposure primarily within the bivalve digestive tract and digestive gland, but migration to other organ systems was not observed. Clusters of MetNPs were recovered in concentrated form from excreted feces, suggesting that biotransformation and biodeposition processes will play an important role in transferring MetNPs from the water column to benthic environments.

DEDICATION

Dedicated to Sherry, Evan, and Olivia—thank you for your love and support these past four years, and the countless sacrifices you've made so that I can have this opportunity. Hopefully now I can help create a lifetime of opportunities for you.

Acknowledgements

I am grateful to so many who made it possible for me to undertake doctoral research at Virginia Tech: to Peter Vikesland, my advisor, mentor, and friend—thank you for your guidance and patience, and for creating a research environment that values personal growth, exploration, and fundamental understanding; special thanks to Nancy Love, my committee co-chair who first convinced me to leave the comforts of industry to pursue doctoral research; to Mike Hochella, whose enthusiasm for science and compassion for people have been inspiring; and to committee members Linsey Marr and Maddy Schreiber whose encouragement and critical research insights have been invaluable these past four years.

Without money there is, sadly, no research, so I express much gratitude to the National Science Foundation IGERT and Environmental Engineering programs, the Center for Environmental Implications of Nanotechnology (CEINT) at Duke University, and the VT Institute for Critical Technology and Applied Science (ICTAS) for generous funding support.

I am grateful to the core faculty, fellows, and administrators of the VT Civil and Environmental Engineering (CEE) Department and the VT EIGER program for creating so many opportunities for interdisciplinary research and professional development. Special thanks are owed to Betty Wingate, Beth Lucas, Mary Hunter, and Bonnie Franklin in CEE, and Ellen Mathena in the Department of Geosciences, for countless hours ‘behind the scenes’ in support of the CEE Environment and Water Resources (EWR) and VT EIGER programs, respectively. Thanks to Julie Petruska, Autumn Timpano, Dawn Maxey, and Carol Johnson for ensuring the function and safety of our research facilities. Thank you to past and present labmates in the ICTAS Environmental Nanoscience Laboratory, particularly Weinan Leng, Beth Diesel, Wendell

Khunjar, Xiaojun Chang, Will Miles, Andy Whelton, Becky Halvorson, Matt Chan, and Krista Rule. Special thanks to an extraordinary group of undergraduate research assistants: Jason Jones, Katie Gloe, Austin Wray, Paul LeBel, and Caitlin Proctor. Thank you to my collaborators and friends across the VT campus: Kathy Lowe, Rich Davis, Mitsu Muryama, Steve McCartney, John McIntosh, and Marion Ehrich.

Many thanks to collaborators who have not only made important contributions to my dissertation research, but who have become dear friends along the way: Irvin Schultz and Mark Jones at Pacific Northwest National Laboratory Marine Sciences Laboratory; *Merci beaucoup!* to my wonderful hosts and research collaborators at the CEREGE in Aix en Provence, France, Drs. Jerome Rose, Perrine Chaurand, Melanie Auffan, and Jean-Yves Bottero; thank you to Alan Kennedy and Jeffrey Steevens of the US Army Corps of Engineers; and a special thanks to Rob MacCuspie, Elijah Petersen, and Vincent Hackley of the National Institute for Standards and Technology (NIST).

A special thank you to my parents, Charles and Sandra Hull, who taught me the value of hard work and compassion towards others, and who inspired my initial pursuits into research that might one day help others.

And finally, thank you to my amazing wife, Sherry, and to our children Evan and Olivia. Your patience and understanding during the many hours I've spent away from you have been humbling. During the times I doubted myself and struggled to find meaning, you were always there for me—supporting me, loving me, and charting the course with perfect clarity.

TABLE OF CONTENTS

Chapter 1. Introduction.....	1
1.1 Background.....	1
1.2 Research Objectives.....	2
1.3 Dissertation Outline.....	3
1.4 Literature Review.....	4
1.5 References.....	10
Chapter 2. Comparative Evaluation of Gold Nanoparticle Aggregation by UV-Vis Spectroscopy and Dynamic Light Scattering.....	17
2.1 Abstract.....	17
2.2 Introduction.....	18
2.3 Experimental Section.....	20
2.4 Results and Discussion.....	23
2.5 Acknowledgements.....	38
2.6 Supporting Information.....	39
2.7 References.....	39
Chapter 3. Quantifying the persistence of noble metallic nanoparticles (MetNPs) in aqueous matrices.....	43
3.1 Abstract.....	43
3.2 Introduction.....	44
3.3 Experimental Section.....	50
3.4 Results and Discussion.....	54
3.5 Acknowledgments.....	65
3.6 References.....	66
Chapter 4. Filter-feeding bivalves store and biodeposit colloiddally stable gold nanoparticles.....	70
4.1 Abstract.....	70
4.2 Introduction.....	71
4.3 Experimental Section.....	72
4.4 Results and Discussion.....	77
4.5 Acknowledgments.....	88
4.6 Supporting Information.....	89
4.7 References.....	96
Chapter 5. Uptake and retention of metallic nanoparticles in the Mediterranean mussel (<i>Mytilus galloprovincialis</i>).....	101
5.1 Abstract.....	101
5.2 Introduction.....	102
5.3 Experimental Section.....	107
5.4 Results and Discussion.....	112
5.5 Acknowledgments.....	122
5.6 References.....	123
Chapter 6. Conclusions.....	127
6.1 Conclusions and Implications.....	127

6.2	A Simplified Conceptual Framework for Bivalve-Mediated Uptake and Fate/ Transport of MetNPs	132
6.3	Summary and Future Work	133
6.4	References	135

LIST OF FIGURES

Chapter 2. Comparative Evaluation of Gold Nanoparticle Aggregation by UV-Vis Spectroscopy and Dynamic Light Scattering	17
Figure 2-1. Effects of primary particle diameter on the aggregation of (a) 7.8, (b) 15, (c) 36, and (d) 46 nm citrate-AuNP at mass-normalized concentrations of 10 mg L ⁻¹ as Au in the presence of varying concentrations of MgSO ₄	25
Figure 2-2. Aggregation rate constants determined by time-resolved DLS for AuNP are a function of particle diameter and salt concentration. Comparison of aggregation rate constants for 7.8, 15, 36 and 46 nm cit-AuNP without (a) and with (b) surface area normalization.	28
Figure 2-3. Aggregation rate constants normalized by particle number (a) and surface area (b), and plotted as a function of primary particle diameter ($d_{TEM, nm}$) for cit-AuNPs added to varying concentrations of MgSO ₄	29
Figure 2-4. TEM images of (a) 7.8 nm, (b) 15 nm, (c) 36 nm, and (d) 46 nm citrate-AuNP exposed to 0.5 mM MgSO ₄ for 24 h. Scale bars are 100 nm.	30
Figure 2-5. Effects of nanoparticle concentration (10 vs. 40 mg L ⁻¹ as Au) on aggregation kinetics of 46 nm cit-AuNP in (a) 1.2 and (b) 2 mM MgSO ₄	31
Figure 2-6. Matrix showing changes in the UV-Vis spectra of four different sizes of cit-AuNP at normalized mass concentration of 10 mg L ⁻¹ as Au after 60 minutes in MgSO ₄ concentrations of 0.5 to 1.0 mM. Note: The $t = 0$ scan is black in color and denoted by a black arrow; final scans ($t = 60$ min.) are light blue in color.	33
Figure 2-7. Relationship between hydrodynamic diameter ($Z_{Avg, nm}$) and absorbance at the LSPR band (Abs_{LSPR}) for 46 nm cit-AuNP (at a mass concentration of 10 mg L ⁻¹ as Au) across a range of MgSO ₄ concentrations. Panels (a) and (b) show the relative change in $Z_{Avg, nm}$ as measured by DLS and $Abs_{LSPR1}:Abs_{LSPR2}$ as measured by UV-Vis spectroscopy (and normalized against t_0 values), respectively, across a range of MgSO ₄ concentrations over time. Note, the vertical dotted line across panels (a) and (b) denotes the first 8 min. of the experiment, which is explained in greater detail in Fig. 2-8. Panel (c) shows the inverse, concentration-dependent relationship between Abs_{LSPR} and $Z_{Avg, nm}$	35
Figure 2-8. Comparison of aggregation regimes separated by the dashed line in Fig. 2-7 and defined by (a) decreasing interparticle distance and (b) increasing cluster size.	37
Figure 2-S1. TEM image showing the spherical and semi-spherical (ellipsoidal) geometry of citrate-AuNP ($d_{TEM} = 46$ nm). Perpendicular dashed lines denote the lateral and longitudinal dimensions of select particles.	39
Chapter 3. Quantifying the persistence of noble metallic nanoparticles (MetNPs) in aqueous matrices	43

Figure 3-1. Conceptual figure illustrating the relationship between nanoparticle persistence in biological or environmental aqueous matrices and unique nanoscale activity..... 49

Figure 3-2. Results of TR-UV-Vis analysis of a 15 nm citrate-AuNP suspension (30 mg L⁻¹ as Au) in 750 μM MgSO₄ for 60 min. illustrating the relationship between Abs_{LSPR1} and Abs_{LSPR2}. Abs_{LSPR1} is determined based on the location of the primary LSPR band for the pristine MetNP suspension; Abs_{LSPR2} is selected based on the unique plasmonic behavior (typically, a bathochromic or red-shift of the LSPR) displayed by the MetNP suspension upon aggregation in a particular medium. 56

Figure 3-3. Comparison of time required for the Abs_{LSPR1}:Abs_{LSPR2} ratio to decrease 50% for 15 nm cit-AuNP in 225 mM MgSO₄ or CaSO₄. 57

Figure 3-4. Panels a-d (top) show 3D plots summarizing the effect of varying electrolyte composition on the UV-Vis spectral properties of 15 nm cit-AuNP during 12 h incubation with 200 mM (a) MgSO₄, (b) CaSO₄, (c) CaCl₂, and (d) mixed CaCl₂ and NaCl concentration. Corresponding plots showing the change in the LSPR_{1, λ=520 nm} to LSPR_{2, λ=600 nm} ratio for each electrolyte are also shown (bottom)..... 59

Figure 3-5. Comparison of TR-UV-Vis spectral plots for six different MetNP suspensions mixed with EPA MHS. MetNP concentrations were normalized at 10 mg L⁻¹ as M⁺. Abs_{LSPR1} and Abs_{LSPR2} for individual MetNP suspensions are noted on the spectral plots..... 62

Figure 3-6. Comparison of the LSPR half-lives of six MetNPs with differing surface coatings in EPA MHS freshwater..... 64

Chapter 4. Filter-feeding bivalves store and biodeposit colloiddally stable gold nanoparticles 70

Figure 4-1. (a-c) TEM images of 7.8, 15, and 46 nm AuNP—in each panel, scale bars denote 100 nm; insets show particles at increased magnification. (d) Plot showing the average water column concentration of 7.8, 15, and 46 nm BSA-AuNP expressed in terms of Au mass concentration (mg L⁻¹) from 0 to 180 h (solid lines denote the average water column [Au] in negative controls—no clams present—as determined from Abs_{LSPR}), and (e) corresponding plot of the log-transformed data (and 95% confidence intervals) for the linear clearance phase (from 48 to 120 h). (f) Plot of the average water column concentration of 46 nm BSA-AuNP as a function of [Au] at t₀ and time exposed to *C. fluminea*; and (g) plot of the linear phase of BSA-AuNP clearance (and 95% confidence intervals). Fitting of these data was used to determine first-order rate constants for clearance of BSA-AuNP as a function of primary particle size and [Au] concentration at t₀.78

Figure 4-2. (a) A μ-XRF image of an HMDS-fixed *C. fluminea* specimen exposed to 46 nm BSA-AuNP for 180 h. Siphons, which were rich with Fe, are colored blue; Au-rich regions in the intestine and at the anus are colored green. The body of the organism is encircled by a dashed line and the locations of the siphons and foot are noted; a dashed rectangle surrounds the digestive gland—additional analysis of the digestive gland and organism cross-sections are provided in the Supporting Information (Figure 4-S8). (b) Semi-quantitative data of the elemental composition of samples were collected by μ-XRF spot-analysis of the *C. fluminea*

specimen shown in panel (a), with numbers 1-5 corresponding to the Au-rich locations noted on the μ -XRF image. Plots showing (c) the relative Au composition (%) of HMDS-fixed *C. fluminea* as determined by μ -XRF and (d) Au body burden (mg Au kg⁻¹ wet tissue weight) as determined by ICP-MS of acid-digested tissue as a function of time (0 to 345 h) and primary particle size of BSA-AuNP—7.8, 15, and 46 nm. The vertical dashed lines at 180 h (panels c and d) indicate the point at which *C. fluminea* were rinsed and transferred from the BSA-AuNP test suspensions to fresh EPA MHS water and allowed to depurate their gut contents..... 85

4-3. TEM images showing structures recovered from feces egested by *C. fluminea* following exposure to BSA-AuNP at 2 mg L⁻¹ as [Au]: (a) cluster of AuNP that are less spherical and less uniform in size than the 46 nm BSA-AuNP that were originally dosed to clams; (b, c) two different types of aggregate structures recovered from the same fecal sample; (d) STEM image of low electron-density fecal material containing clusters of 15 nm AuNP (white circle added to indicate one cluster); (e) Hi-Res TEM and (f) EDX indicating that particles recovered from feces of clams exposed to 15 nm BSA-AuNP at 2 mg L⁻¹ are spherical, crystalline, uniform in size, and comprised primarily of Au..... 88

Figure 4-S1. Plots of UV-Vis spectra showing the time-dependent (0 to 180 h) decrease in absorbance intensity at Abs_{SPR} for 7.8 nm, 15 nm, and 46 nm BSA-AuNP suspensions in the presence of *C. fluminea*. Initial concentrations of BSA-AuNP were mass normalized to 2 mg L⁻¹ as [Au]..... 90

Figure 4-S2. Extinction spectra for the Au ion and 7.8, 15, and 46 nm gold nanoparticles.91

Figure 4-S3. Characteristic changes in absorbance spectra and the location or height of Abs_{SPR} over time due to (a) aggregation in EPA MHS after 120 min versus (b) particle clearance by a filter-feeding bivalve. The arrow denotes the location of a new absorption band that forms upon aggregation of AuNP, but is not evident when AuNP are cleared from suspensions via biological filtration..... 92

Figure 4-S4. Plot showing first-order rate constants for clearance of BSA-AuNP as a function of primary particle diameter. 92

Figure 4-S5. UV-Vis spectra showing the time-dependent decrease in absorbance intensity of the SPR band of three sizes of BSA-AuNP—prepared individually and in combination as a ‘cocktail’ at a concentration of 15 mg L⁻¹ as [Au]—in the presence of *C. fluminea*..... 93

Figure 4-S6. (a) Plot of the mean blue shift \pm SD (n = 3) observed for the SPR band of the cocktail in the presence and absence of clams and (b) the predicted change in the respective contributions of each size of particle to the overall composition of the cocktail based on the size-dependent clearance rates. Beyond 96 h, the composition of 46 nm BSA-AuNP was below detection limits..... 94

Figure 4-S7. Comparison of average SPR band shift for BSA-AuNP cocktails from the size-selective uptake experiment (with and without clams) and the experiment with cocktails prepared at the particle size composition and total [Au] predicted from the size-selective uptake experiment. 95

Figure 4-S8. (a) μ -XRF image of *C. fluminea* tissue cross-sections showing the internalization of Au (light areas surrounded by dashed boxes) within the digestive tract; (b) synchrotron-based μ -XRF (LUCIA beamline) Au map of a cross-section of the *C. fluminea* digestive gland..... 95

Chapter 5. Uptake and retention of metallic nanoparticles in the Mediterranean mussel (*Mytilus galloprovincialis*) 101

Figure 5-1. a) Suspensions of FeNP stabilized with PEG (left) and unstabilized (right) prepared in SW—note the visible aggregates forming in the unstabilized FeNP suspension on the right; b) TEM image of PEG-FeNP. 109

Figure 5-2. Manufacturer-reported information for Invitrogen Qdot® ITK 655 quantum dots: a) TEM image of core-shell Qdot® nanoparticles at 200,000x magnification—scale bar = 20 nm. b) Schematic of Qdot® conjugate structure..... 109

Figure 5-3. Experimental set-up for water column exposures. 111

Figure 5-4. Uptake of 50 nm PEG-FeNPs by mussels. a) Pre-exposure evaluation of PEG-FeNP stability in SW. Total Fe was measured after PEG-FeNPs were isolated magnetically. b) Loss of Fe from water column after the addition of mussels to beakers (white squares, n = 3). Shell only beakers are black squares. Banded mussels (to prevent filtering) are represented by the black triangles. c) Fe measured in water column during depuration. After exposure, mussels were washed in clean SW and placed in new beakers with clean SW. 114

Figure 5-5. Levels of Fe in a) digestive gland and carcass at termination and after 18 and 73 h (n = 3), and b) hemolymph immediately following uptake plus 73 and 140 h depuration in fresh seawater. Note that most of the Fe, >90% of what was initially added to the exposure water is retained in the digestive gland. Very little Fe, 2-4 %, is retained in the remaining carcass. 115

Figure 5-6. Loss of Fe from SW after adding mussels (white squares, n = 3). 117

Figure 5-7. Total Fe in digestive gland and carcass following termination of mussel exposures to HA-FeNP. 118

Figure 5-8. a) Pre-exposure tests for PEG-Qdot stability in solution as determined by levels of Cd. b) Uptake of PEG-Qdots into mussels (white squares n = 4). Beakers with only mussel shells are black squares (n = 2). c) PEG-Qdots in water during depuration. After exposure, mussels were washed in SW and placed in new beakers with fresh SW..... 119

Figure 5-9. (left) PEG-Qdots in the digestive gland and remaining carcass after 72 h depuration. (right) % of PEG-Qdots in the tissue relative to the total loss of Cd from the exposure beaker. 120

Figure 5-10. Depuration of Cd measured in hemolymph upon exposure termination and after 24 and 72 h depuration in fresh SW. 121

Chapter 6. Conclusion127

Figure 6-1. Simplified conceptual framework for bivalve-mediated uptake and fate/transport of MetNPs in aquatic systems.133

LIST OF TABLES

Chapter 2. Comparative Evaluation of Gold Nanoparticle Aggregation by UV-Vis Spectroscopy and Dynamic Light Scattering	17
Table 2-1. Summary of size and particle number and surface area concentrations for four sizes of cit-AuNP.....	24
Chapter 3. Quantifying the persistence of noble metallic nanoparticles (MetNPs) in aqueous matrices	43
Table 3-1. Summary of Au and AgNP suspensions prepared for the development and evaluation of a persistence metric for optically active MetNPs.....	52
Chapter 4. Filter-feeding bivalves store and biodeposit colloidally stable gold nanoparticles	70
Table 4-S1. Characteristics of BSA-AuNP. Size of primary particles on a TEM grid ($n \geq 100$) is expressed as the median value of the size determined using ImagePro and as the diameter predicted by Haiss et al. using the location and height of the surface Plasmon resonance (SPR) band. ¹ Mean effective hydrodynamic diameter (Z_{ave} , nm), polydispersity index (PDI), electrophoretic mobility (mm cm (Vs)^{-1}), and location of the SPR band as measured in EPA moderately hard reconstituted water (EPA MHS).....	96

ATTRIBUTION

Chapter 1. Introduction

M. Hull and P. Vikesland wrote the paper

Chapter 2. Comparative Evaluation of Gold Nanoparticle Aggregation by UV-Vis Spectroscopy and Dynamic Light Scattering

M. Hull and P. Vikesland conceived and designed experiments

M. Hull performed the experiments

M. Hull, R. MacCuspie and P. Vikesland analyzed the data

M. Hull, R. MacCuspie and P. Vikesland wrote the paper

M. Hull, R. MacCuspie and P. Vikesland critically reviewed and edited the manuscript

Chapter 3. Quantifying the persistence of noble metallic nanoparticles (MetNPs) in aqueous matrices

M. Hull and P. Vikesland conceived and designed experiments

M. Hull performed the experiments

M. Hull, R. MacCuspie and P. Vikesland analyzed the data

M. Hull, R. MacCuspie and P. Vikesland wrote the paper

M. Hull, R. MacCuspie and P. Vikesland critically reviewed and edited the manuscript

Chapter 4. Filter-feeding bivalves store and biodeposit colloidally stable gold nanoparticles

**Reproduced with permission from Environmental Science and Technology. Hull, M.S., Chaurand, P., Rose, J., Auffan, M., Bottero, J-Y., Jones, J.C., Schultz, I.R., Vikesland, P.J. 2011. Filter-feeding bivalves store and biodeposit colloidally stable gold nanoparticles. 45 (15), 6592-6599. Copyright © 2011 American Chemical Society*

M. Hull, P. Chaurand, J. Rose and P. Vikesland conceived and designed experiments

M. Hull, P. Chaurand and J. Jones performed the experiments

M. Hull, P. Chaurand, J. Rose, M. Auffan, J.Y. Bottero, I. Schultz and P. Vikesland analyzed the data

M. Hull, P. Chaurand, and P. Vikesland wrote the paper

M. Hull, P. Chaurand, P. Vikesland, J. Rose, M. Auffan, J.Y. Bottero, and I. Schultz critically reviewed and edited the manuscript

Chapter 5. Uptake and retention of metallic nanoparticles in the Mediterranean mussel (*Mytilus galloprovincialis*)

I. Schultz conceived and designed experiments

M. Hull and I. Schultz performed the experiments

M. Hull, I. Schultz and P. Vikesland analyzed the data

M. Hull, I. Schultz and P. Vikesland wrote the paper

M. Hull, I. Schultz and P. Vikesland critically reviewed and edited the manuscript

Chapter 6. Conclusion

M. Hull and P. Vikesland wrote the paper

Chapter 1. Introduction

1.1 Background

Similar to what has been observed with pharmaceuticals and personal care products (PPCPs),¹ consumer use and disposal of ‘bionanomaterials’ — nanomaterials functionalized with biological carriers such as proteins, oligonucleotides, and cell-penetrating peptides² — will inevitably result in their discharge to municipal wastewater treatment systems and ultimately to aquatic ecosystems.^{3,4} Among other functions, biological carriers enhance the stability of nanoparticles in high ionic strength solutions, such as blood,⁵ which in turn may lead to increased persistence of individual nanoscale particles in natural waters. The stability and persistence of nanoscale particles will affect their fate and transport upon entering aquatic systems,⁴ wherein they may be ingested, accumulated, and transformed by biota.⁶ Many questions remain as to the toxicity of nanoscale materials and their transformation products. Some studies report that nanoparticles induce toxicity,⁷ whereas others suggest that they may promote positive health outcomes, such as prolonging the life of brain cells.⁸ One concern, however, is that a majority of the studies published to date have focused on the use of nanomaterials that are readily available from commercial sources (e.g., C₆₀, ZnO), but lack surface modifications (e.g., polymer-coatings, biological carriers) that are critical to end-use applications of these materials. In terms of their fate and transport in aquatic systems, particularly marine environments, these simplified forms of nanomaterials differ considerably from the functionalized materials incorporated into commercial products and that ultimately will be released into the environment.⁹ Accordingly, an improved understanding of the uptake and fate of bionanomaterials in biological and environmental systems is especially critical. In this effort, we determined how key characteristics of nanoscale materials—size, shape, and surface chemistry—influence uptake and fate in two

species of bivalves—*Corbicula fluminea* [Müller, 1774] and *Mytilus galloprovincialis* [Lamarck, 1819]. *Corbicula fluminea* is ubiquitous in streams and rivers across the US and around the world, and is often employed for biomonitoring of contaminants in freshwater environments.¹⁰ *Mytilus galloprovincialis*, which is also known as the ‘blue’ or ‘Mediterranean’ mussel, is a marine mussel found primarily in the low intertidal zones of rocky coastlines around the world. In some regions, *M. galloprovincialis* is harvested or cultivated for human consumption. We expect that uptake of nanoscale particles by filter-feeding bivalves will be a function of the type of biological carrier molecule used to functionalize the particle as well as particle size, shape, and composition.

1.2 Research Objectives

We investigated the influence of size and surface chemistry on the uptake and biological fate and transport of metallic nanoparticles (MetNPs) in filter-feeding bivalves. An important objective of our work was to prepare well-characterized nanoparticle test suspensions and apply complementary characterization techniques that facilitated understanding of nanoparticle disposition in exposure media and within bivalve test organisms and biodeposited feces. This comprehensive approach was warranted at the time this dissertation research was undertaken since much of the published literature offered limited understanding of the relationships between physicochemical properties of nanoscale particles and their uptake by aquatic biota. In particular, many of these studies failed to describe the persistence of nanoscale test materials in exposure media as individually stabilized nanoscale particles. In theory, the existence of nanoscale materials as either individually-stabilized, monodisperse particles or as clusters or aggregates of varying size and shape would likely have significant effects on the nature of

nanoparticle interactions with biological and environmental systems. Thus, our research objectives were focused on investigating the validity of the following hypotheses:

Hypothesis 1: Integrated characterization techniques are necessary to evaluate the stability and persistence of MetNP suspensions in aquatic media, and to enable effective interpretation of the bioavailability of nanoscale particles to filter-feeding biota.

Hypothesis 2: Uptake of MetNP by filter-feeding bivalves should be modulated by particle size, with larger particles being cleared from suspension more rapidly than smaller particles.

Hypothesis 3: Biological fate and transport of MetNPs in filter-feeding bivalves should follow established bivalve models and MetNPs should localize primarily in the gills, mantle, and digestive gland.

Hypothesis 4: Biodeposition will factor prominently in the transference of MetNPs from the water column to the benthic zone, and patterns of uptake and biodeposition may be useful for biomonitoring of AuNP as well as other nanoparticles discharged to aquatic systems.

1.3 Dissertation Outline

This dissertation contains a total of six chapters including this introductory chapter. **Chapter 2** describes our efforts to apply integrated characterization techniques, specifically time-resolved- dynamic light scattering (DLS) and UV-vis spectroscopy, to evaluate the aggregation kinetics of variably sized citrate-stabilized gold nanoparticles (cit-AuNP) in electrolyte solutions that are relevant to understanding nanoparticle disposition in freshwater exposure media. **Chapter 3** presents a novel UV-Vis based metric that is useful for quantifying and comparatively evaluating the colloidal persistence of optically active metallic nanoparticles.

Chapter 4 describes a comprehensive evaluation of the uptake and biodeposition of variably-sized gold nanoparticles stabilized with the protein bovine serum albumin (BSA-AuNP) by the Asian clam (*Corbicula fluminea*), and leverages what we have learned from nanoparticle suspension preparation and characterization to enhance our understanding of how individually stabilized nanoparticles are processed by aquatic filter-feeders. **Chapter 5** describes research undertaken to investigate how applicable our research findings with *C. fluminea* and BSA-AuNP are to *M. galloprovincialis* and MetNPs. **Chapter 6** presents our general conclusions regarding the persistence of MetNPs in aquatic systems with a specific emphasis on the factors influencing MetNP uptake and fate in filter-feeding bivalves.

1.4 Literature Review

Hundreds of consumer products are currently available that incorporate engineered nanomaterials as a means of improving performance or production efficiency, and thousands of other nano-enabled products are expected to enter commercial markets over the next decade.¹¹ As a result of its rapid integration into existing and emerging products, nanotechnology is expected to represent a >\$2 Trillion per year global economic impact by 2015.¹² Given the size of this market and ongoing concerns about the environmental fate of nanomaterials,¹³⁻¹⁵ a wide-ranging effort has been undertaken to understand the potential consequences of unanticipated releases of nanomaterials to the environment. Recent reports have definitively shown that engineered nanomaterials can be transported in the environment,¹⁶ can be taken up by cells,¹⁷⁻²⁰ and can subsequently elicit toxic effects.¹⁹ Characterization of the fundamental phenomena responsible for these processes is ongoing.⁹ One concern, however, is that a majority of the studies published to date have focused on the use of simplified forms of nanomaterials (e.g., C₆₀,

ZnO) that are readily available from commercial suppliers. These nanomaterials may not reflect the functionalized products that will ultimately be employed by industry and that will be released into the environment. Of particular concern are those nanomaterials that are specifically designed for biomedical applications. In many cases, these materials are surface-functionalized such that they have enhanced aqueous solubility²¹ and have the ability to cross cellular membranes.²² These characteristics suggest these materials will have very different fates than many of the nanomaterials studied to date.

Engineered bionanomaterials integrated with biological carrier molecules such as proteins, polymers, DNA, and cell penetrating peptides, are expected to be among the first, most broadly applied, and—because some are designed to pass through cellular membranes—potentially the most ecologically significant forms of nanotechnology-enabled materials. Similar to what has been observed with pharmaceuticals and personal care products (PPCPs),^{1, 23} consumer or medical practitioner use and disposal of nano-enabled pharmaceuticals may result in the discharge of bionanomaterials to municipal wastewater treatment systems and, ultimately, to aquatic ecosystems. Accordingly, an improved understanding of the uptake and fate of bionanomaterials in biological and environmental systems is especially critical.

Bivalves as sentinel organisms for emerging contaminants. Freshwater and marine bivalves are widely used as biological sentinels to detect and monitor a broad spectrum of environmental contaminants including metals,²⁴ persistent organic pollutants,²⁵⁻²⁷ biocides,²⁸ asbestos fibers,^{29, 30} bacteria,³¹ and protozoan parasites.³²⁻³⁵ Given their functional roles in aquatic ecosystems as water column and sediment filter feeders, bivalves are susceptible to adverse effects from environmental contaminants and are especially useful as keystone or indicator species for measuring pollutant contamination of aquatic systems.¹⁰ Furthermore,

because they contain significant quantities of lipid material ($\approx 10\%$ on a dry weight basis³⁶) that readily accumulates environmental contaminants, post-exposure analysis of bivalve tissue can often be used to establish a forensic record of environmental exposures.

For more than 25 years, researchers have used the freshwater bivalve, *Corbicula fluminea* (Müller) as a bioindicator of water pollution. *C. fluminea*, originating in Asia, has progressively colonized waterways throughout the U.S. and Europe and is a major component of the freshwater benthic community worldwide. As a filter-feeding organism, *C. fluminea* is exposed to contaminants that can accumulate within its tissue: heavy metals,²⁴ PCBs,²⁵⁻²⁷ and asbestos fibers.^{29, 30, 37} *C. fluminea* has the highest filtration rate of all freshwater bivalves and filters approximately 45 L water g^{-1} dry weight day^{-1} .²⁷ This exceptionally high filtration rate ($\approx 20\times$ higher than the filtration rate for the marine clam *Macoma balthica*²⁷) facilitates the potential accumulation of trace level pollutants within *C. fluminea* and is one reason that *C. fluminea* is often used as a sentinel organism.

The uptake of particulate pollutants by *C. fluminea* and *M. galloprovincialis*, similar to what is observed with other aquatic bivalves, occurs when the organism filter- or deposit-feeds. Deposit-feeding, which primarily occurs through ciliary action of the clam foot (e.g., pedal feeding), and filter-feeding are equally important as sources for the uptake of deposit-associated PCBs²⁷ and other environmental contaminants. Regardless of the mechanism by which particles are ingested, however, they are transferred and processed by the same pathways inside the bivalve.³⁸ In general, these pathways involve the internalization of particulate material via endocytosis and the distribution of material to internal organs and interstitial connective tissue via hemolymph traveling through the unconstrained circulatory system of the bivalve.^{39, 40} The hemolymph, or blood, bathes all of the internal organs before ultimately returning to the heart by

way of the sinuses and gills.³⁹

Metallic nanoparticles. Metallic nanoparticles (MetNPs) are a class of engineered nanomaterials defined by their metallic composition and which are among the most readily manufactured and useful nanoscale materials currently in production.⁴¹ Included within the class of MetNPs are iron oxide nanoparticles (FeOxNPs) with novel superparamagnetic behavior,⁴² the semiconducting quantum dots (Qdots) with precisely tunable optical properties,⁴³ and a broad spectrum of metal and metal oxide nanoparticles comprised of, for example, noble metals including platinum, silver, and gold.⁴⁴ Of this diverse array of MetNPs, gold nanoparticles (AuNPs) have arguably attracted the greatest attention for their unique combination of novel plasmonic behavior, ease of synthesis, stability, and accessibility.⁴⁵⁻⁴⁷ Colloidal gold is inert and often used for the production of biologically compatible nanoparticle carriers.⁴⁸⁻⁵⁰ Spherical gold nanoparticles can be synthesized at diameters ranging from < 2 nm to > 200 nm. The combination of precisely controlled size and facile surface chemistry have enhanced the utility of gold nanoparticles in a broad range of life sciences and pharmaceutical applications. Further, gold nanoparticles are an ideal model material for the proposed study because it can be used to produce a range of different nanoparticle geometries—spheres, rods, rice, prisms, cubes, and many others—that facilitate testing of the effects of shape on uptake and toxicity of bionanomaterials.⁵¹ Finally, the natural abundance of gold in environmental samples and biological tissue is extremely low and thus background influences on analytical measurements are negligible.

Bionanomaterials. As defined herein, bioconjugated nanoparticles or ‘bionanomaterials’ are nanoparticles that have been functionalized such that their transport in blood and across cell membranes is enhanced. Bionanomaterials are currently being developed for applications such

as drug⁵² and gene⁵³ delivery, cancer therapies,^{54, 55} and immunostaining.⁵⁶ There are several bionanomaterials, such as Doxil⁵⁷ and Abraxane⁵⁸ that are being actively marketed for therapeutic use and many additional bionanomaterials are in clinical testing such as Cycloset⁵⁹ and Genexol-PM.⁶⁰

The key to the development of medically useful bionanomaterials is the application of surface chemistries that enable the nanoparticles to remain stabilized in blood and to bypass biological barriers that might remove the material or otherwise alter its active form. Within the human body, unfunctionalized nanoparticles are subject to opsonization wherein opsonin proteins bind to the nanoparticles and mediate their recognition and removal by macrophages. In contrast, functionalized bionanomaterials can evade opsonins and increase *in vivo* circulation half-lives considerably. Ongoing studies seek to develop nanoparticle surface chemistries that enable the particles to readily cross biological membranes and precisely deliver pharmaceuticals and other payloads inside cells. Examples of such approaches include surface functionalization with polyethylene glycol (PEG; 1-mecaptoundec-11-yl-tetraethylene glycol),⁶¹ oligonucleotide modification,^{62, 63} peptide functionalization,^{64, 65} or protein conjugation using, for example, bovine serum albumin (BSA).⁶⁶

PEG functionalization. Functionalization of nanoparticles with an FDA approved PEG monolayer (e.g., PEGylation) produces bionanomaterials that are resistant to aggregation under physiological conditions. Random coiling of the PEG molecules is thought to hinder protein adsorption and thus PEG functionalization enhances nanoparticle opsonin evasion.^{61, 67} The opsonin resistance of PEGylated nanomaterials enables extended blood circulation times⁶¹ and thus a number of PEGylated nanomaterials are being tested as drug delivery agents.⁴⁵ Interestingly, in spite of widespread acceptance of their potential utility for drug delivery, Natio

et al.⁶⁸ recently documented that PEGylated gold nanoparticles are not taken up by HeLa cells. In contrast, other studies have shown their uptake,^{69, 70} albeit with different cell types.

BSA conjugation. Bovine serum albumin (BSA) is widely used as a carrier protein for immunoassays and a broad range of biochemical applications. Li-Mei et al.⁷¹ reported the stabilization of gold nanoparticles through surface charge interactions with BSA. Despite the fact that it is negatively charged at pH 7, BSA preferentially binds to negatively charged surfaces. Brewer et al.⁷² suggested that in the presence of citrate, a stabilizing agent used often during citric-acid reduction synthesis of Au nanoparticles (e.g., Turkevich et al.⁷³), BSA binds to Au nanoparticles by an electrostatic mechanism involving salt-bridges between the citrate present on the gold surface and the 60 surface lysine groups present on the surface of BSA. Gold nanoparticles coated with BSA have been used frequently for cell-targeting applications and thus may be expected to penetrate the cellular matrices of bivalve test organisms.

Bionanomaterial fate in *C. fluminea* and *M. galloprovincialis*. Current understanding of the potential fate of engineered nanomaterials within *Corbicula* and *Mytilus*, as well as other filter-feeding bivalves is limited. A recent study,⁷⁴ however, suggests that nanomaterials can be taken up by bivalves and can accumulate within them. Using the blue mussel, *Mytilus edulis*, Koehler et al.⁷⁴ showed that glass wool nanofibrils (a nonengineered nanomaterial) are taken up when the mussels are raised on beds of untreated glass wool fibers. These nanofibrils accumulated within endocytotic vesicles, lysosomes, mitochondria, and nuclei. Continual uptake of these nanomaterials resulted in large aggregates of ingested nanoparticles within the lysosomes that ultimately led to apoptosis due to decreased membrane stability. Although this is one of the few known studies examining nanoparticle uptake into bivalves, there are studies with asbestos,^{29, 30,}³⁷ protozoan parasites,³²⁻³⁴ bacteria,³⁹ and metal particles⁴⁰ that provide insight into the potential

fate of bionanomaterials in bivalves.

According to the current models for metal uptake in bivalves, specific tissues and organ systems are involved in uptake, storage, detoxification, and elimination of metals such as gold. The gills provide the key interface for uptake of dissolved metals. Some metals, such as Cd^{2+} may diffuse passively into the gills across Ca^{2+} channels.⁷⁵ Insoluble metal compounds, such as iron oxides, may be absorbed into the gills through a process known as pinocytosis.⁷⁶ This uptake mechanism may be especially relevant for solid bionanomaterials. From the gills, metals can be sequestered transitorily in epithelial lysosomes and calcified granules⁴⁰ or transported across epithelial cells to the blood and hemocytes.⁷⁷ However, metals may also bind to metallothioneines for rapid excretion.⁴⁰ The mantle provides another direct interface for the accumulation of metals such as Cd, Cu, Fe, Hg, and Zn in lysosomes.⁷⁸ Most particulate associated metals enter bivalves through the digestive tract and digestive gland⁷⁹ in conjunction with food particles or hemocytes that have phagocytosed metal-containing particles.⁴⁰ Conversely, bivalve gametes such as the gonad typically do not accumulate appreciable levels of metals relative to other tissue.^{40, 78} Given the findings of these previous studies, we hypothesize that if gold bionanomaterials are processed in accordance with established bivalve models, clusters of MetNPs should be localized primarily in the gills, mantle, digestive tract/gland, and hemocytes.

1.5 References

1. Daughton, C. G.; Ternes, T. A., Pharmaceuticals and personal care products in the environment: agents of subtle change? *Environmental Health Perspectives* **1999**, 107, 907-938.
2. Lin, J.; Zhang, H.; Chen, Z.; Zheng, Y., Penetration of lipid membranes by gold nanoparticles: insights into cellular uptake, cytotoxicity, and their relationship. *ACS Nano* **2010**, 4 (9), 5421-

5429.

3. Kim, B.; Park, C.; Muryama, M.; Hochella, M. J., Discovery and characterization of silver sulfide nanoparticles in final sewage sludge products. *Environmental Science & Technology* **2010**, *44* (19), 7509-7514.
4. Petosa, A.; Jaisi, D.; Quevedo, I.; Elimelech, M.; Tufenkji, N., Aggregation and deposition of engineered nanomaterials in aquatic environments: role of physicochemical interactions. *Environmental Science & Technology* **2010**, *44* (17), 6532-6549.
5. Yang, W.; Zhang, L.; Wang, S.; White, A.; Jiang, S., Functionalizable and ultra stable nanoparticles coated with zwitterionic poly(carboxybetaine) in undiluted blood serum. *Biomaterials* **2009**, *30* (29), 5617-5621.
6. Moore, M., Do nanoparticles present ecotoxicological risks for the health of the aquatic environment? *Environment International* **2006**, *32* (8), 967-976.
7. Pan, Y.; Leifert, A.; Ruau, D.; Neuss, S.; Bornemann, J.; Schmid, G.; Brandau, W.; Simon, U.; Jahnen-Dechent, W., Gold nanoparticles of diameter 1.4 nm trigger necrosis by oxidative stress and mitochondrial damage. *Small* **2009**, *5* (18), 2067-2076.
8. Chung, D., Nanoparticles have health benefits too. *New Scientist* **2003**, 179 (2410), 16.
9. Wiesner, M. R.; Lowry, G. V.; Alvarez, P.; Dionysiou, D.; Biswas, P., Assessing the risks of manufactured nanomaterials. *Environmental Science & Technology* **2006**, *40* (14), 4336-4345.
10. Doherty, F. G., The Asiatic clam, *Corbicula* spp, as a biological monitor in freshwater environments. *Environmental Monitoring and Assessment* **1990**, *15* (2), 143-181.
11. Woodrow Wilson International Center for Scholars. The Project on Emerging Nanotechnologies. (September 2011),
12. Lux Research. <https://portal.luxresearchinc.com/>.
13. Colvin, V. L., The potential environmental impact of engineered nanomaterials. *Nature Biotechnology* **2003**, *21*, 1166-1170.
14. Nel, A.; Xia, T.; Madler, L.; Li, N., Toxic potential of materials at the nanolevel. *Science* **2006**, *311* (5761), 622-627.
15. Oberdörster, G.; Oberdörster, E.; Oberdörster, J., Nanotoxicology: An emerging discipline evolving from studies of ultrafine particles. *Environmental Health Perspectives* **2005**, *113* (7), 823-839.
16. Lecoanet, H. F.; Bottero, J. Y.; Wiesner, M. R., Laboratory assessment of the mobility of nanomaterials in porous media. *Environmental Science & Technology* **2004**, *38* (19), 5164-5169.
17. Brayner, R.; Ferrari-Iliou, R.; Brivois, N.; Djediat, S.; Benedetti, M. F.; Fievet, F., Toxicological impact studies based on *Escherichia coli* bacteria in ultrafine ZnO nanoparticles colloidal medium. *Nano Letters* **2006**, *6* (4), 866-870.

18. Limbach, L. K.; Li, Y. C.; Grass, R. N.; Brunner, T. J.; Hintermann, M. A.; Muller, M.; Gunther, D.; Stark, W. J., Oxide nanoparticle uptake in human lung fibroblasts: Effects of particle size, agglomeration, and diffusion at low concentrations. *Environmental Science & Technology* **2005**, 39 (23), 9370-9376.
19. Xia, T.; Kovoichich, M.; Brant, J.; Hotze, M.; Sempf, J.; Oberley, T.; Sioutas, C.; Yeh, J. I.; Wiesner, M. R.; Nel, A. E., Comparison of the abilities of ambient and manufactured nanoparticles to induce cellular toxicity according to an oxidative stress paradigm. *Nano Letters* **2006**, 6 (8), 1794-1807.
20. Xia, T.; Kovoichich, M.; Liong, M.; Zink, J. I.; Nel, A. E., Cationic polystyrene nanosphere toxicity depends on cell-specific endocytic and mitochondrial injury pathways. *ACS Nano* **2008**, 2, 85-96.
21. Devalapally, H.; Chakilam, A.; Amiji, M. M., Role of nanotechnology in pharmaceutical product development. *Journal of Pharmaceutical Sciences* **2007**, 96, 2547-2565.
22. Teixido, M.; Giralt, E., The role of peptides in blood-brain barrier nanotechnology. *Journal of Peptide Science* **2008**, 14, 163-173.
23. Ternes, T. A., Pharmaceuticals and Metabolites as Contaminants of the Aquatic Environment. In *Pharmaceuticals and Personal Care Products in the Environment: Scientific and Regulatory Issues*, Daughton, C. G.; Jones-Lepp, T. L., Eds. ACS Books: Washington, D.C., 2001; Vol. Symposium Series 791, pp 39-54.
24. Croteau, M. N.; Luoma, S. N., Delineating copper accumulation pathways for the freshwater bivalve *Corbicula* using stable copper isotopes. *Environmental Toxicology and Chemistry* **2005**, 24 (11), 2871-2878.
25. Bjork, M.; Gilek, M., Efficiencies of polychlorinated biphenyl assimilation from water and algal food by the blue mussel (*Mytilus edulis*). *Environmental Toxicology and Chemistry* **1999**, 18 (4), 765-771.
26. Gustafsson, K.; Bjork, M.; Burreau, S.; Gilek, M., Bioaccumulation kinetics of brominated flame retardants (polybrominated diphenyl ethers) in blue mussels (*Mytilus edulis*). *Environmental Toxicology and Chemistry* **1999**, 18 (6), 1218-1224.
27. McLeod, P. B.; Luoma, S. N.; Luthy, R. G., Biodynamic modeling of PCB uptake by *Macoma balthica* and *Corbicula fluminea* from sediment amended with activated carbon. *Environmental Science & Technology* **2008**, 42, 484-490.
28. Champeau, O.; Narbonne, J. F. S., Effects of tributyltin and 17 beta-estradiol on immune and lysosomal systems of the Asian clam *Corbicula fluminea* (M.). *Environmental Toxicology and Pharmacology* **2006**, 21 (3), 323-330.
29. Belanger, S. E.; Cherry, D. S.; Cairns, J., Seasonal, behavioral and growth changes of juvenile *Corbicula fluminea* exposed to chrysotile asbestos. *Water Research* **1986**, 20 (10), 1243-1250.
30. Belanger, S. E.; Cherry, D. S.; Cairns, J.; McGuire, M. J., Using Asiatic clams as a biomonitor for chrysotile asbestos in public water supplies. *Journal American Water Works Association* **1987**, 79 (3), 69-74.

31. Blaise, C.; Trottier, S.; Gagne, F.; Lallement, C.; Hansen, P. D., Immunocompetence of bivalve hemocytes as evaluated by a miniaturized phagocytosis assay. *Environmental Toxicology* **2002**, 17 (3), 160-169.
32. Graczyk, T. K.; Cranfield, M. R.; Conn, D. B., In vitro phagocytosis of *Giardia duodenalis* cysts by hemocytes of the Asian freshwater clam *Corbicula fluminea*. *Parasitology Research* **1997**, 83 (8), 743-745.
33. Graczyk, T. K.; Fayer, R.; Cranfield, M. R.; Conn, D. B., In vitro interactions of Asian freshwater clam (*Corbicula fluminea*) hemocytes and *Cryptosporidium parvum* oocysts. *Applied and Environmental Microbiology* **1997**, 63 (7), 2910-2912.
34. Graczyk, T. K.; Fayer, R.; Lewis, E. J.; Farley, C. A.; Trout, J. M., In vitro interactions between hemocytes of the Eastern oyster, *Crassostrea virginica* Gmelin, 1791 and *Cryptosporidium parvum* oocysts. *Journal of Parasitology* **1997**, 83 (5), 949-952.
35. Miller, W. A.; Gardner, I. A.; Atwill, E. R.; Leutenegger, C. M.; Miller, M. A.; Hedrick, R. P.; Melli, A. C.; Barnes, N. M.; Conrad, P. A., Evaluation of methods for improved detection of *Cryptosporidium* spp. in mussels (*Mytilus californianus*). *Journal of Microbiological Methods* **2006**, 65 (3), 367-379.
36. Schwarzenbach, R. P.; Gschwend, P. M.; Imboden, D. M., *Environmental Organic Chemistry*. John Wiley and Sons, Inc.: New York, 2002.
37. Belanger, S. E.; Cherry, D. S.; Cairns, J., Uptake of chrysotile asbestos fibers alters growth and reproduction of Asiatic clams. *Canadian Journal of Fisheries and Aquatic Sciences* **1986**, 43 (1), 43-52.
38. Nichols, S. J.; Silverman, H.; Dietz, T. H.; Lynn, J. W.; Garling, D. L., Pathways of food uptake in native (Unionidae) and introduced (Corbiculidae and Dreissenidae) freshwater bivalves. *Journal of Great Lakes Research* **2005**, 31 (1), 87-96.
39. Canesi, L.; Gallo, G.; Gavioli, M.; Pruzzo, C., Bacteria-hemocyte interactions and phagocytosis in marine bivalves. *Microscopy Research and Technique* **2002**, 57 (6), 469-476.
40. Marigomez, I.; Soto, M.; Cajaraville, M. P.; Angulo, E.; Giamberini, L., Cellular and subcellular distribution of metals in molluscs. *Microscopy Research and Technique* **2002**, 56 (5), 358-392.
41. Feldheim, D.; Foss, C., *Metal nanoparticles: synthesis, characterization, and applications*. CRC Press: New York, 2002; p 352.
42. Gupta, A.; Gupta, M., Synthesis and surface engineering of iron oxide nanoparticles for biomedical applications. *Biomaterials* **2005**, 26 (18), 3995-4021.
43. Michalet, X.; Pinaud, F.; Bentolila, L.; Tsay, J.; Doose, S.; Li, J.; Sundaresan, G.; Wu, A.; Gambhir, S.; Weiss, S., Quantum dots for live cells, in vivo imaging, and diagnostics. *Science* **2005**, 307 (5709), 538-544.
44. Jain, P.; Huang, X.; El-Sayed, I.; El-Sayed, M., Noble metal on the nanoscale: optical and photothermal properties and some applications in imaging, sensing, biology, and medicine.

Accounts of Chemical Research **2008**, 41 (12), 1578-1586.

45. Cheng, Y.; Samia, A. C.; Meyers, J. D.; Panagopoulos, I.; Fei, B. W.; Burda, C., Highly efficient drug delivery with gold nanoparticle vectors for in vivo photodynamic therapy of cancer. *Journal of the American Chemical Society* **2008**, 130 (32), 10643-10647.
46. Daniel, M.; Astruc, D., Gold nanoparticles: assembly, supramolecular chemistry, quantum-size-related properties, and applications toward biology, catalysis, and nanotechnology. *Chemical Reviews* **2004**, 104 (1), 293-346.
47. Eustis, S.; El-Sayed, M., Why gold nanoparticles are more precious than pretty gold: noble metal surface plasmon resonance and its enhancement of the radiative and nonradiative properties of nanocrystals of different shapes. *Chemical Society Reviews* **2006**, 35, 209-217.
48. Connor, E. E.; Mwamuka, J.; Gole, A.; Murphy, C. J.; Wyatt, M. D., Gold nanoparticles are taken up by human cells but do not cause acute cytotoxicity. *Small* **2005**, 1 (3), 325-327.
49. Lewinski, N.; Colvin, V.; Drezek, R., Cytotoxicity of nanoparticles. *Small* **2008**, 4 (1), 26-49.
50. Shukla, R.; Bansal, V.; Chaudhary, M.; Basu, A.; Bhonde, R. R.; Sastry, M., Biocompatibility of gold nanoparticles and their endocytotic fate inside the cellular compartment: A microscopic overview. *Langmuir* **2005**, 21 (23), 10644-10654.
51. Chithrani, B. D.; Ghazani, A. A.; Chan, W. C. W., Determining the size and shape dependence of gold nanoparticle uptake into mammalian cells. *Nano Letters* **2006**, 6 (4), 662-668.
52. Popielarski, S. R.; Pun, S. H.; Davis, M. E., A nanoparticle-based model delivery system to guide the rational design of gene delivery to the liver. 1. Synthesis and characterization. *Bioconjugate Chemistry* **2005**, 16 (5), 1063-1070.
53. Bielinska, A. U.; Yen, A.; Wu, H. L.; Zahos, K. M.; Sun, R.; Weiner, N. D.; Baker, J. R.; Roessler, B. J., Application of membrane-based dendrimer/DNA complexes for solid phase transfection in vitro and in vivo. *Biomaterials* **2000**, 21 (9), 877-887.
54. El-Sayed, I. H.; Huang, X. H.; El-Sayed, M. A., Selective laser photo-thermal therapy of epithelial carcinoma using anti-EGFR antibody conjugated gold nanoparticles. *Cancer Letters* **2006**, 239 (1), 129-135.
55. Hainfeld, J. F.; Slatkin, D. N.; Smilowitz, H. M., The use of gold nanoparticles to enhance radiotherapy in mice. *Physics in Medicine and Biology* **2004**, 49 (18), N309-N315.
56. Alivisatos, A. P., Less is more in medicine - Sophisticated forms of nanotechnology will find some of their first real-world applications in biomedical research, disease diagnosis and, possibly, therapy. *Scientific American* **2001**, 285 (3), 66-73.
57. Coker, R. J.; James, N. D.; Stewart, J. S. W., Hepatic Toxicity of Liposomal Encapsulated Doxorubicin. *Lancet* **1993**, 341 (8847), 756-756.
58. Gradishar, W. J., Albumin-bound paclitaxel: a next-generation taxane. *Expert Opinion on Pharmacotherapy* **2006**, 7 (8), 1041-1053.

59. Schluep, T.; Hwang, J.; Cheng, J. J.; Heidel, J. D.; Bartlett, D. W.; Hollister, B.; Davis, M. E., Preclinical efficacy of the camptothecin-polymer conjugate IT-101 in multiple cancer models. *Clinical Cancer Research* **2006**, 12 (5), 1606-1614.
60. Kim, T. Y.; Kim, D. W.; Chung, J. Y.; Shin, S. G.; Kim, S. C.; Heo, D. S.; Kim, N. K.; Bang, Y. J., Phase I and pharmacokinetic study of Genexol-PM, a cremophor-free, polymeric micelle-formulated paclitaxel, in patients with advanced malignancies. *Clinical Cancer Research* **2004**, 10 (11), 3708-3716.
61. Owens, D. E.; Peppas, N. A., Opsonization, biodistribution, and pharmacokinetics of polymeric nanoparticles. *International Journal of Pharmaceutics* **2006**, 307 (1), 93-102.
62. Giljohann, D. A.; Seferos, D. S.; Patel, P. C.; Millstone, J. E.; Rosi, N. L.; Mirkin, C. A., Oligonucleotide loading determines cellular uptake of DNA-modified gold nanoparticles. *Nano Letters* **2007**, 7, 3818-3821.
63. Rosi, N. L.; Giljohann, D. A.; Thaxton, C. S.; Lytton-Jean, A. K. R.; Han, M. S.; Mirkin, C. A., Oligonucleotide-modified gold nanoparticles for intracellular gene regulation. *Science* **2006**, 312, 1027-1030.
64. de la Fuente, J. M.; Berry, C. C., Tat peptide as an efficient molecule to translocate gold nanoparticles into the cell nucleus. *Bioconjugate Chemistry* **2005**, 16 (5), 1176-1180.
65. Santra, S.; Yang, H.; Dutta, D.; Stanley, J. T.; Holloway, P. H.; Tan, W. H.; Moudgil, B. M.; Mericle, R. A., TAT conjugated, FITC doped silica nanoparticles for bioimaging applications. *Chemical Communications* **2004**, (24), 2810-2811.
66. Li-Mei, A.; Feng, G.; Bi-Feng, P.; Da-Xiang, C.; Hong-Chen, G., Interaction between gold nanoparticles and bovine serum albumin or sheep antirabbit immunoglobulin G., *Chinese Journal of Chemistry* **2006**, 24, 253-256.
67. Gref, R.; Luck, M.; Quellec, P.; Marchand, M.; Dellacherie, E.; Harnisch, S.; Blunk, T.; Muller, R. H., 'Stealth' corona-core nanoparticles surface modified by polyethylene glycol (PEG): influences of the corona (PEG chain length and surface density) and of the core composition on phagocytic uptake and plasma protein adsorption. *Colloids and Surfaces B-Biointerfaces* **2000**, 18 (3-4), 301-313.
68. Nativo, P.; Prior, I. A.; Brust, M., Uptake and intracellular fate of surface-modified gold nanoparticles. *Acs Nano* **2008**, ASAP article.
69. Paciotti, G. F.; Kingston, D. G. I.; Tamarkin, L., Colloidal gold nanoparticles: A novel nanoparticle platform for developing multifunctional tumor-targeted drug delivery vectors. *Drug Development Research* **2006**, 67 (1), 47-54.
70. Shenoy, D.; Little, S.; Langer, R.; Amiji, M., Poly(ethylene oxide)-modified poly(beta-amino ester) nanoparticles as a pH-sensitive system for tumor-targeted delivery of hydrophobic drugs: Part 2. In vivo distribution and tumor localization studies. *Pharmaceutical Research* **2005**, 22 (12), 2107-2114.
71. Li-Mei, A.; Feng, G.; Bi-Feng, P.; Da-Xiang, C.; Hong-Chen, G., Interaction between gold nanoparticles and bovine serum albumin or sheep antirabbit immunoglobulin G. *Chinese Journal*

- of Chemistry* **2006**, 24, 253-256.
72. Brewer, S. H.; Glomm, W. R.; Johnson, M. C.; Knag, M. K.; Franzen, S., Probing BSA binding to citrate-coated gold nanoparticles and surfaces. *Langmuir* **2005**, 21, 9303-9307.
 73. Turkevich, J.; Stevenson, P. C.; Hillier, J. A., Study of the nucleation and growth processes in the synthesis of colloidal gold. *Discuss. Faraday Soc.* **1951**, 11, 55-59.
 74. Koehler, A.; Marx, U.; Broeg, K.; Bahns, S.; Bressling, J., Effects of nanoparticles in *Mytilus edulis* gills and hepatopancreas - A new threat to marine life? *Marine Environmental Research* **2008**, 66 (1), 12-14.
 75. Roesijadi, G.; Unger, M. E., Cadmium uptake in gills of the mollusk *Crassostrea virginica* and inhibition by calcium-channel blockers. *Aquatic Toxicology* **1993**, 24 (3-4), 195-206.
 76. George, S.; Pirie, B.; TL, C., Adsorption, accumulation, and excretion of iron-protein complexes by *Mytilus edulis*. *Publication of the National Research Council of Canada* **1975**, 2, 887-900.
 77. Mason, A.; K, S., Interactions between metals and their distribution in tissues of *Littorine littorea* collected from clean and polluted sites. *Journal of Marine Biology Association UK* **1983**, 63, 661-672.
 78. Soto, M.; Cajaraville, M. P.; Marigomez, I., Tissue and cell distribution of copper, zinc and cadmium in the mussel, *Mytilus galloprovincialis*, determined by autometallography. *Tissue & Cell* **1996**, 28 (5), 557-568.
 79. Viarengo, A.; Pertica, M.; Canesi, L.; Biasi, F.; Cecchini, G.; Orunesu, M., Effects of heavy-metals on lipid-peroxidation in mussel tissues. *Marine Environmental Research* **1988**, 24 (1-4), 354-354.

Chapter 2. Comparative Evaluation of Gold Nanoparticle Aggregation by UV-Vis Spectroscopy and Dynamic Light Scattering

M. Hull^{1,2,3}, R. MacCuspie⁴, and P. Vikesland^{1,2,3}

¹Virginia Tech Department of Civil and Environmental Engineering, Blacksburg, VA, USA

²Virginia Tech Institute for Critical Technology and Applied Science (ICTAS) Center for Sustainable Nanomaterials (VT SuN), Blacksburg, VA, USA

³Center for the Environmental Implications of Nanotechnology (CEINT), Duke University, Durham, NC, USA

⁴National Institutes of Standards and Technology (NIST), Gaithersburg, MD, USA.

2.1 Abstract

Although the tendency for colloids to aggregate in high ionic strength media such as blood or high-hardness waters has been established for decades, few studies have attempted to relate alterations in aggregation state to changes in the localized surface plasmon resonance (LSPR) behavior of noble metallic nanoparticles. Herein, we employed time-resolved dynamic light scattering (TR-DLS) and time-resolved UV-Vis spectroscopy (TR-UV-Vis) to investigate kinetic changes in hydrodynamic diameter and LSPR behavior, respectively, for citrate-capped gold nanoparticles (cit-AuNP) with primary particle diameters of 7.8 ± 3.3 , 15 ± 6.8 , 36 ± 2.9 , and 46 ± 5.3 nm. Our results show that in a divalent electrolyte solution at a fixed ionic strength and a mass-normalized particle concentration of 10 mg L^{-1} (as Au) that aggregation rates for cit-AuNP increase with a decrease in primary particle diameter. The experimental results qualitatively

agree with DLVO theory, which predicts that a decrease in particle diameter will lower the interaction energy barrier, thus increasing the propensity for small particles to aggregate more rapidly than larger particles. Nanoparticle concentrations play an important role in governing aggregation behavior, however, and aggregation rates of large particles exceed those of smaller particles when nanoparticle concentrations are normalized by particle number. Upon surface area normalization, however, and under diffusion-limited conditions, the aggregation rate constants were effectively identical. The results of time-resolved UV-Vis spectroscopy, when interpreted in the context of Generalized Multiparticle Mie (GMM) theory, support the DLS results and show that interparticle distances derived from changes in LSPR behavior decrease at a rate inversely proportional to primary particle diameter. Collectively, these results can be used to define two distinct aggregation regimes—the first representing the initial decrease in interparticle spacing that occurs shortly after addition of electrolyte to an optically active metallic colloid, and the second occurring thereafter as a function of cluster growth—that can be effectively measured by the integration of TR-UV-Vis and TR-DLS, respectively.

2.2 Introduction

Noble metal nanoparticles exhibit unique optical behavior arising from the nanoscale phenomenon known as localized surface plasmon resonance (LSPR).¹ LSPR occurs when an externally applied resonant electromagnetic field induces the collective oscillation of the surface free electrons of a nanoparticle.² In the early 1900's, Mie described this phenomenon and its effect on the ultraviolet-visible (UV-Vis) absorption spectra of small metallic spheres surrounded by a dielectric medium.^{3, 4} The resonance condition for gold and silver nanospheres, which is a function of the dielectric constant of the medium, the size of the nanoparticle, and the dielectric

function of the metal, is satisfied at visible wavelengths of the electromagnetic spectrum.² For example, in water, the LSPR for ≈ 20 nm gold nanoparticles occurs at ≈ 520 nm, but as nanoparticle diameter increases to ≈ 100 nm, the LSPR band redshifts to ≈ 600 nm. Additionally, the presence of ions and surface coatings, such as proteins and polymers, affect the location and intensity of the LSPR because they modify the local dielectric in the vicinity of the nanoparticle surface.⁵

Redshifts of the LSPR can be indicative of aggregation processes.^{6, 7} As first described by Derjaguin, Landau, Verwey, and Overbeek (DLVO),^{8, 9} electrolyte-induced collapse of the electrostatic double layer surrounding charged particles leads to the coupling and subsequent aggregation of nanoparticle monomers. As the monomers form dimers and polymers, the growing nanoparticle clusters induce a red-shift in the LSPR band to a wavelength that is similar to that observed for large-diameter nanoparticle monomers or rod-like materials having an aspect ratio sufficient to create both transverse and longitudinal LSPR bands.¹⁰ Eventually, the LSPR band(s) are no longer observed as the growing clusters settle out of suspension and the novel optical activity of the once stable colloidal suspension is lost, in many cases, irreversibly.

Studies by numerous investigators have shown the tendency of nanoscale particles to form large clusters when introduced to biological media¹¹ or natural aquatic systems.^{12, 13} The extent of aggregation is dependent on a number of factors including particle concentration, media ionic composition and strength, pH, organic matter composition, and the presence of stabilizing surface coatings such as proteins and polymers.¹³⁻¹⁹ Previous studies examining nanoparticle aggregation kinetics have used either time-resolved dynamic light scattering (DLS) or UV-Vis spectroscopy (UV-Vis), yet markedly few studies have attempted to establish quantitative relationships between these complementary nanoparticle characterization techniques.²⁰

Integration of DLS and UV-Vis characterization of metal nanoparticles simultaneously addresses the issues of increasing cluster size as well as aggregation-induced changes in the position and shape of the LSPR band(s). By itself, DLS provides information on cluster size, yet provides no information about changes in the optical behavior of colloidal systems that stem from aggregation. In contrast, UV-Vis spectroscopy yields information that can be used to estimate the diameter, shape, and homogeneity of nanoparticle monomers of homogeneous size,²¹ but has limited utility in the characterization of extensively aggregated systems or heterodisperse colloidal suspensions.⁴ Recently, others have attempted to derive models that relate UV-Vis absorbance spectra to heterogeneous particle size distributions, which may have applicability for characterizing changes in aggregation state.⁴

Most studies of nanoparticle aggregation kinetics are limited in that they typically rely upon a single technique to evaluate the aggregation process. In the current study, we simultaneously utilized DLS and UV-Vis spectroscopy to examine the stability and LSPR activity of citrate-stabilized gold nanoparticles (cit-AuNP) as a function of primary particle diameter (d_{TEM}) in media of varying electrolyte composition. The combination of these highly complementary analytical techniques enable the identification of two distinct aggregation regimes characterized by i) an initial decrease in interparticle spacing and ii) cluster growth.

2.3 Experimental Section

Preparation of gold nanoparticle suspensions. Reagent-grade sodium citrate tribasic dihydrate, 99% ($\text{Na}_3\text{C}_6\text{H}_5\text{O}_7 \cdot 2\text{H}_2\text{O}$), sodium borohydride (98%; NaBH_4), and gold(III) chloride trihydrate ($\text{HauCl}_4 \cdot 3\text{H}_2\text{O}$) were obtained from Sigma-Aldrich (St. Louis, MO, USA). All reagents and nanoparticle suspensions were prepared in $>18 \text{ M}\Omega$ resistivity ultrapure water.

Citrate-capped gold nanoparticles (cit-AuNP) of 7.8 nm diameter were prepared using the method of Jana et al.²² Larger 15 nm cit-AuNP were prepared as described by Turkevich.²³ The seed-mediated process of Frens²⁴ was used to prepare cit-AuNP of 36 and 46 nm average primary particle diameter. Each suspension incorporated citrate as a reducing agent (or co-reducing agent) and surface stabilizer, as citrate is known to play an important role in determining the size and monodispersivity of gold nanoparticles by regulating the pH of the precipitation reaction.²⁵ All suspensions were filtered (0.2 μm sterile vacuum filter), transferred to a glass vial, and stored in the dark at 4 °C until use.

Characterization. All nanoparticle suspensions were characterized by UV-Vis spectroscopy, transmission electron microscopy (TEM), and dynamic light scattering. Primary particle size and morphology were determined using a Zeiss 10CA Transmission Electron Microscope equipped with a high resolution (1024 \times 1024 pixel format) MT Advantage GR/HR-B CCD Camera System (Advanced Microscopy Techniques Corp.). Voltage was kept at 60 kV for all samples. Samples were prepared by pipetting 10-20 μL of cit-AuNP suspension onto a carbon-coated copper TEM grid (Electron Microscopy Sciences) that was then air dried at room temperature. To assess the heterogeneity of the nanoparticle suspensions and to determine average primary particle diameters, electron micrographs were digitized and analyzed using ImagePro (MediaCybernetics, Bethesda, MD). Estimates of hydrodynamic diameter (Z-average) and electrophoretic mobility were obtained using a Malvern Zetasizer NanoZS (Malvern, UK). UV-Vis spectroscopy measurements were obtained using a Cary 5000 UV-Vis-NIR spectrophotometer (Agilent Technologies). Gold ion concentrations were measured using a Thermo Electron X-Series inductively coupled plasma-mass spectrometer (ICP-MS).²⁶ Samples

and calibration standards were prepared in a matrix of 2% aqua regia to minimize gold adsorption to sample tubing or internal instrument surfaces.

Evaluation of colloidal stability. The colloidal stability of the nanoparticle suspensions was evaluated in 0.5-30 mM solutions containing sodium bicarbonate (NaHCO_3), potassium chloride (KCl), magnesium sulfate (MgSO_4), calcium sulfate (CaSO_4), or calcium chloride (CaCl_2). Based on initial studies, and consistent with prevailing colloidal theory, the divalent cations Mg^{2+} and Ca^{2+} induced aggregation of the negatively charged cit-AuNP at lower concentrations than Na^+ . As a comprehensive investigation of the contributions of varying ions to aggregation kinetics was outside the scope of this manuscript, we focused our experiments primarily on one of the divalent cations, Mg^{2+} , and its effects on the aggregation kinetics of cit-AuNP of 7.8, 15, 36, and 46 nm diameter, as measured by the complementary techniques of DLS and UV-Vis spectroscopy. Others have previously performed extensive comparisons of how variations in salt identity affect nanoparticle aggregation rates.^{15, 18}

The colloidal stability of the nanoparticle suspensions was evaluated using both time-resolved DLS (TR-DLS) and time resolved UV-Vis spectroscopy (TR-UV-Vis). For DLS measurements, hydrodynamic diameter was monitored as a function of time and electrolyte concentration using the Malvern NanoZS. To evaluate colloidal stability by UV-Vis spectroscopy, the absorbance intensity of the localized surface plasmon resonance band (Abs_{LSPR}) of each AuNP suspension was monitored over time using either the kinetic ($\lambda = \text{LSPR}$) or kinetic scanning modes ($\lambda = 300\text{-}800$ nm) of the UV-Vis spectrophotometer. For all experiments, temperature was maintained at 25 °C by internal instrument controls. Experiments ranged in length from 10 to 60 minutes.

Size- and concentration-dependence of aggregation kinetics. Experiments were performed primarily at a mass-normalized cit-AuNP concentration of 10 mg L^{-1} as Au. However, to further investigate the effect of particle size on the aggregation kinetics, a sub-set of experiments was performed at cit-AuNP concentrations normalized at a particle number concentration of 4.5×10^{10} particles mL^{-1} . For this experiment, 15, 36 and 46 nm cit-AuNPs were used, as these three suspensions could be produced at similar particle number concentrations while present at a mass concentration sufficient for either UV-Vis or DLS measurement.

Suspensions were added to 1 cm cuvettes and then spiked with electrolyte solutions diluted in nanopure water at concentrations varying from 0.15 to 16 mM. After spiking cit-AuNP suspensions with an electrolyte, samples were quickly vortex-mixed and then immediately placed into either the DLS or UV-Vis instrument for kinetic studies. All studies were performed at 25 °C. Apparent initial aggregation rate constants, k_{11} , were determined based upon TR-DLS measurements of cluster size following electrolyte addition. These measurements were made for each cit-AuNP suspension across a range of MgSO_4 concentrations. The application of DLS to measure the time-dependent increase in hydrodynamic diameter of nanoparticle suspensions is well established.^{16, 18}

2.4 Results and Discussion

Characterization of cit-AuNP suspensions. TEM image analysis indicated that the mean primary particle diameters of cit-AuNP ($n > 100$) were 7.8 ± 3.3 , 15 ± 6.8 , 36 ± 2.9 , and 46 ± 5.3 nm. The corresponding hydrodynamic diameters (Z_{ave} , nm) determined by cumulant analysis of dynamic light scattering (DLS) correlelograms were 9.9 ± 0.2 , 18.9 ± 0.1 , 31.5 ± 0.2 nm, and 33.9 ± 0.1 nm, respectively. Particle diameters predicted based upon the position of the LSPR

band²¹ were 4.2, 11.4, 35.3 and 38.4 nm, each of which is in general agreement with the diameters measured by TEM and DLS (Table 2-1). For the largest particles, the discrepancy between the TEM and DLS determined diameters may be attributable in part to the fact that particles of this size are not perfectly spherical and instead exhibit an ellipsoidal shape (Figure 2-S1). Each type of particle was negatively charged at the pH of the electrolyte solution (pH = 7.8) with electrophoretic mobilities of -1.96 ± 0.07 , -2.05 ± 0.13 , -2.58 ± 0.19 , and $-1.71 \pm 0.01 \mu\text{m}\cdot\text{cm}(\text{V}\cdot\text{s})^{-1}$ for the 7.8, 15, 36, and 46 nm cit-AuNP, respectively. Corresponding zeta potentials were -25.0 ± 0.85 , -41.0 ± 1.04 , -32.9 ± 2.40 , and -27.2 ± 1.13 mV.

Table 2-1. Summary of size and particle number and surface area concentrations for four sizes of cit-AuNP.

ID	d_{TEM} (nm)	d_{DLS} (nm)	d_{LSPR} (nm)	N₀ (particles L⁻¹) for 10 mg L⁻¹ suspension	Surface area (m² L⁻¹) for 10 mg L⁻¹ suspension
7.8	7.8 ± 3.3	9.9 ± 0.2	4.2	2.09 × 10 ¹⁵	0.40
15	15 ± 6.8	18.9 ± 0.1	11.4	2.94 × 10 ¹⁴	0.21
36	36 ± 2.9	31.5 ± 0.2	35.3	3.67 × 10 ¹³	0.09
46	46 ± 5.3	33.9 ± 0.1	38.4	1.02 × 10 ¹³	0.07

Effects of cit-AuNP diameter on nanoparticle stability in a divalent electrolyte solution.

Addition of 0.5-1 mM MgSO₄ to 7.8, 15, 36, and 46 nm cit-AuNP suspensions rapidly caused formation of nanoparticle clusters with hydrodynamic diameters that approached 600 nm for the smallest and 100 nm for the largest nanoparticles, respectively. As shown in Figure 2-1, the aggregation kinetics of cit-AuNP were a function of the initial primary particle diameter with aggregation most rapid for 7.8 and 15 nm cit-AuNP under these test conditions. At MgSO₄ concentrations below 1 mM, the aggregation of 36 and 46 nm cit-AuNP was quite slow and generally insensitive to the hydrodynamic diameter. However, at a MgSO₄ concentration of 1 mM, 36 nm cit-AuNP aggregated more rapidly than 46 nm cit-AuNP.

Rate constants describing the initial aggregation kinetics were determined by fitting a linear curve to the hydrodynamic diameter data for $t < 20$ min. This timeframe was utilized in an effort to capture the early-stage aggregation kinetics. Our DLS instrument was not set-up to measure true initial aggregation rates (i.e., $t < 1$ min) and thus these rate constants should not be considered illustrative of the initial aggregation kinetics.

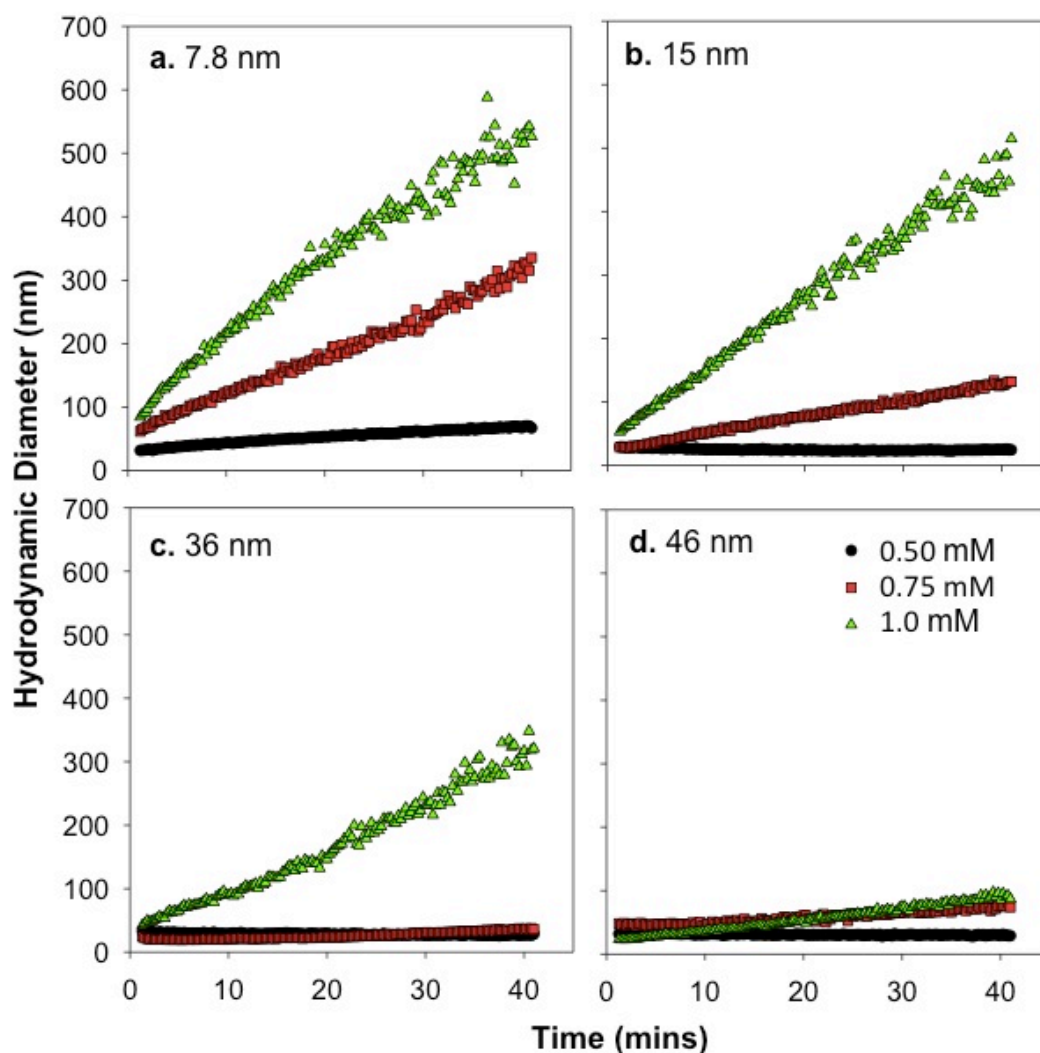


Figure 2-1. Effects of primary particle diameter on the aggregation of (a) 7.8, (b) 15, (c) 36, and (d) 46 nm cit-AuNP at mass-normalized concentrations of 10 mg L^{-1} as Au in the presence of varying concentrations of MgSO_4 .

As shown in Figure 2-2a, there is an inverse relationship between the initial primary particle diameter and the aggregation rate constant k_{11} . This trend is most obvious at 1000 μM , but is also apparent at the lower concentrations as well. Expectedly, as the electrolyte concentration was increased from 0.5 to 1 mM, k_{11} also increased. The observation that the aggregation rates of cit-AuNP are greater for smaller particles is consistent with results reported by He et al²⁷ for the aggregation of hematite nanoparticles with sizes of 12, 32, and 65 nm. In that study, as was observed here, the aggregation rates were inversely related to particle size.

The aggregation rate constant k_{11} describing the kinetics of nanoparticle aggregation can be described mathematically as (Eqn. 2-1):

$$k_{11} \propto \frac{1}{N_0} \left(\frac{dD_h(t)}{dt} \right)_{t \rightarrow 0} \quad 2-1$$

Based upon equation 2-1 it is apparent that the measured aggregation rate constant should be inversely dependent upon the particle number concentration. The experiments conducted to obtain the data summarized in Figures 2-1 and 2-2a were conducted under a mass normalized condition of 10 mg L⁻¹ as Au. Accordingly, the number concentrations for the suspensions ranged from 1.02×10^{13} to 2.09×10^{15} particles L⁻¹; and the estimated total surface area concentrations (assuming spherical particle geometries) ranged from 0.07 to 0.40 m² L⁻¹ (Table 2-1). In an attempt to account for the variability in surface area amongst the four particle sizes, we calculated surface area normalized rate constants k_{11}^* (Eqn. 2-2)

$$k_{11}^* = N_0 k_{11} (4\pi r^2) \quad 2-2$$

where N_0 is the particle number concentration (particles mL⁻¹); k_{II} is the aggregation rate constant; and r is the radius of a spherical nanoparticle based on d_{TEM} . The results of this calculation are plotted in Figure 2-2b and show that following surface area normalization, the effect of particle diameter on the aggregation rate constant is diminished, particularly at the highest MgSO₄ concentration of 1000 μM. At 750 μM MgSO₄, however, the surface area normalized rate constants remain positively related to particle diameter, suggesting that even after accounting for surface area effects, smaller particles aggregate more rapidly than larger ones. The fact that the largest particles aggregate more slowly may be at least partially attributable to the decrease in diffusion that occurs as a result of increasing particle radius, as demonstrated by the Stokes-Einstein equation (Eqn. 2-3):

$$D = \frac{k_B T}{6\pi \eta a} \quad 2-3$$

where k_B is the Boltzmann constant, T is the absolute temperature in degrees K, η is the fluid viscosity, and a is the particle radius.

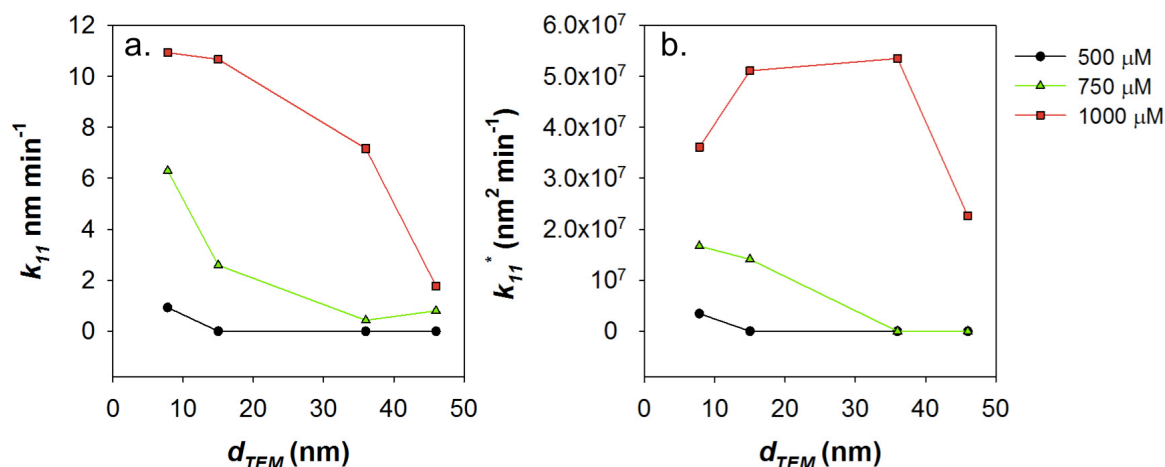


Figure 2-2. Aggregation rate constants determined by time-resolved DLS for AuNP are a function of particle diameter and salt concentration. Comparison of aggregation rate constants for 7.8, 15, 36 and 46 nm cit-AuNP without (a) and with (b) surface area normalization.

To further evaluate the effects of primary particle diameter on the measured aggregation rates, an experiment was conducted using 15, 36, and 46 nm cit-AuNP suspensions prepared at a normalized particle number concentration of 4.5×10^{10} particles mL⁻¹. Particle number concentrations were determined as described previously by Haiss et al.²¹ and were obtained by diluting suspensions with an appropriate volume of double-deionized water until the desired N_0 concentrations were obtained. Five different MgSO₄ concentrations were investigated: 700, 800, 900, 1000, and 2000 μ M. We selected this range to improve resolution of aggregation kinetics around the 750 μ M concentration that induced aggregation in the previous experiment, as well as to ensure that diffusion-limited conditions were met. At normalized N_0 , the 46 nm cit-AuNP particles aggregated more rapidly than the smaller 15 and 36 nm particles due to the increase in available surface area, which can be estimated based on the measured d_{TEM} and the assumption of spherical particle geometry (Figure 2-S1). Based on this simple assumption, a single 46 nm cit-AuNP has nearly twice the geometric surface area of a 36 nm cit-AuNP, and nearly ten times the surface area of a 15 nm cit-AuNP. Similarly, the aggregation rate constant k_{11} for 46 nm cit-

AuNP is more than double that of the 36 nm particles, and nearly ten times that of the 15 nm cit-AuNP (Figure 2-3a). As noted by others, the effect of surface area on aggregation kinetics is consistent with DLVO theory.²⁷ A plot of the surface area normalized aggregation rate constants k_{11}^* versus d_{TEM} shows that similar to the results presented in Figure 2-2, the effect of particle diameter on the aggregation rate constant is diminished at an $MgSO_4$ concentration of 2000 μM (Figure 2-3b). As $MgSO_4$ concentration is increased to 5000 μM (diffusion-limited conditions), the aggregation rate constants are negatively related to d_{TEM} , suggesting that after accounting for surface area effects, aggregation rates are driven primarily by the increased rate of diffusion of smaller particles predicted by the Stokes-Einstein equation.

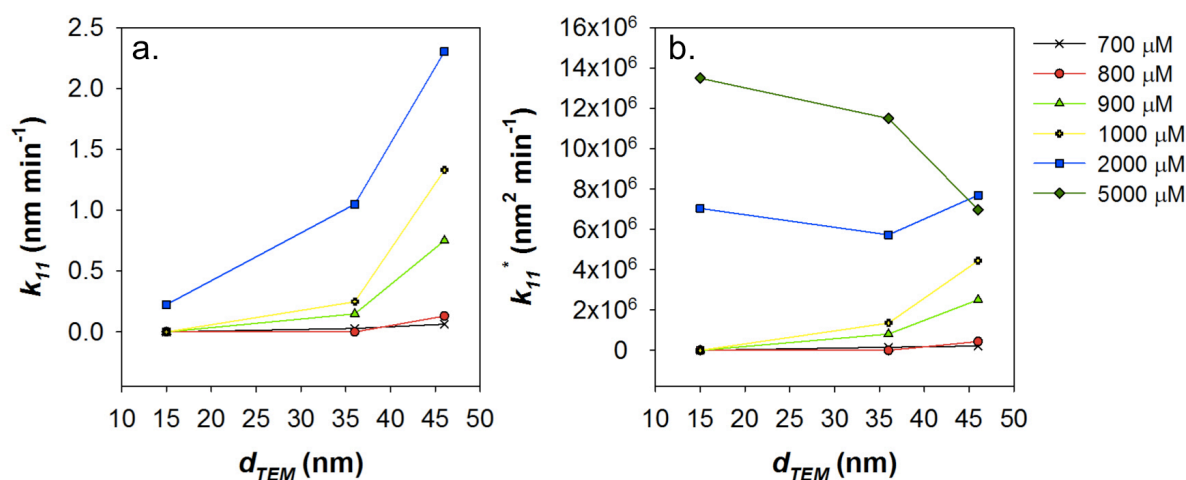


Figure 2-3. Aggregation rate constants normalized by particle number (a) and surface area (b), and plotted as a function of primary particle diameter ($d_{TEM, nm}$) for cit-AuNPs added to varying concentrations of $MgSO_4$.

In addition to aggregating more rapidly than the other three sizes of cit-AuNP, the smallest particles (7.8 nm) also formed the largest nanoparticle clusters as determined by DLS (Figure 2-1) and as suggested by TEM (Figure 2-4). As shown in Figure 2-4, TEM image analysis of the varying sizes of cit-AuNP incubated with 0.5 mM $MgSO_4$ over 24 h generally support the DLS

results by demonstrating that 7.8 nm cit-AuNP formed micron-sized clusters, whereas the 15, 36, and 46 nm particles were more likely to form sub-micron clusters. *Note: TEM grids were prepared by air-drying of cit-AuNP suspensions, so some drying-induced aggregation is apparent in Figure 2-4; clusters formed due to drying can be distinguished from irreversibly-formed aggregates due to the absence of ‘necks’ linking multiple particles.*

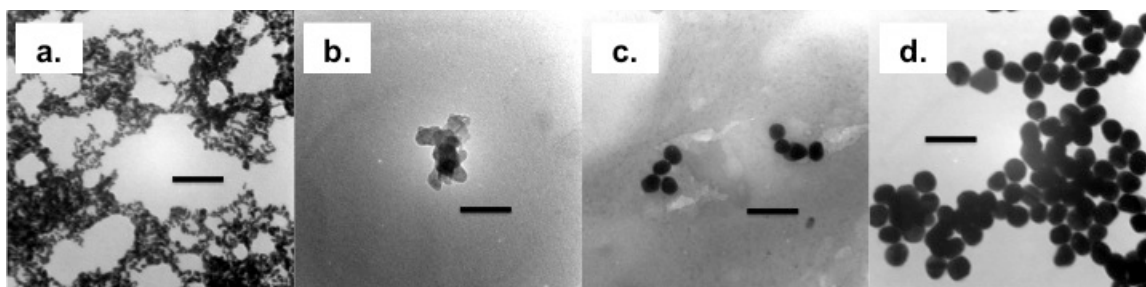


Figure 2-4. TEM images of (a) 7.8 nm, (b) 15 nm, (c) 36 nm, and (d) 46 nm citrate-AuNP exposed to 0.5 mM MgSO₄ for 24 h. Scale bars are 100 nm.

Past authors²⁷ noted that the change in the aggregation rate with particle size is consistent with Derjaguin-Landau-Verwey-Overbeek (DLVO) theory, which predicts that smaller particles are more likely to aggregate due to the increased specific surface area and total surface energy that accompany a decrease in particle size. As particle size decreases, the activation energy barrier responsible for separating particles and maintaining a stabilized system is reduced, leading to rapid aggregation.

One limitation of DLVO theory is that it does not account for the effects of particle concentration on the measured aggregation rates. Instead, DLVO simply describes the interaction energies between two surfaces of prescribed geometry. A change in particle concentration, however, does significantly alter the measured kinetics of aggregation. As illustrated in Figure 2-5, the effects of nanoparticle concentration on the aggregation kinetics diminish with an

increase in electrolyte concentration. Upon addition of a 1.2 mM MgSO_4 solution, the aggregation rate of 46 nm cit-AuNP at 10 mg L^{-1} as Au mass concentration is markedly reduced relative to the same particles added at a mass concentration of 40 mg L^{-1} (Figure 2-5a). When the divalent electrolyte concentration is increased to 2 mM, however, the aggregation rates of 46 nm cit-AuNP are similar at both 10 and 40 mg L^{-1} nanoparticle concentrations (Figure 2-5b).

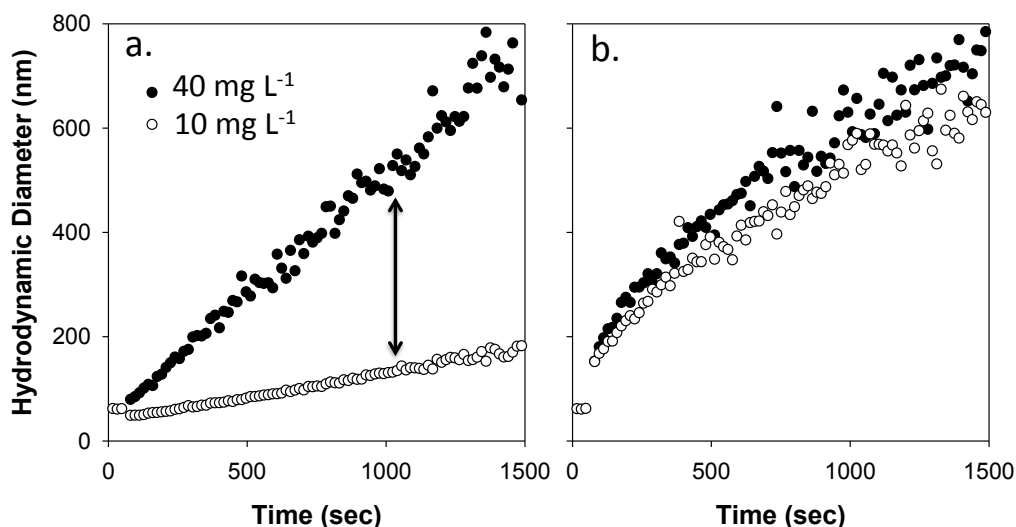


Figure 2-5. Effects of nanoparticle concentration (10 vs. 40 mg L^{-1} as Au) on aggregation kinetics of 46 nm cit-AuNP in (a) 1.2 and (b) 2 mM MgSO_4 .

Relationship between cit-AuNP aggregation and LSPR behavior. Aggregation events between particles induce electrodynamic interactions that result in changes to the LSPR band. We measured these changes as a function of particle diameter and divalent electrolyte concentration using TR-UV-Vis spectroscopy. The results of these experiments, shown in Figure 2-6, support the findings of our TR-DLS and TEM studies by showing that characteristic changes in the LSPR behavior of Au nanoparticles—i.e., weakening of the primary plasmon band and the appearance of a second, redshifted plasmon band—are more pronounced for smaller particles. Further, our TR-UV-Vis results can be explained through a modification of

classical Mie theory known as Generalized Multiparticle Mie (GMM) theory.²⁸⁻³⁰ When present as highly dispersed, stable colloids, spherical Au nanoparticles exhibit a distinct resonance peak attributable to quadrupole plasmon excitation of single metallic spheres that can be predicted by traditional Mie theory. When Au colloids become destabilized (i.e., the repulsion barrier is overcome as described by DLVO), distances between neighboring particles decrease until individual particles begin to couple and ultimately form large clusters. As interparticle distance decreases to less than $\approx 4\times$ the particle radius, the primary resonance peak weakens and a secondary peak, attributable to the dipole plasmon resonance of coupled Au nanoparticles, appears at a longer, redshifted wavelength. At this point, the single-sphere assumption of classical Mie theory is no longer valid and more advanced interpretations of optical behavior are required. The secondary LSPR peak intensifies as the interparticle distance approaches zero, where it reaches its maximum. Ultimately, all indications of the colloids' LSPR activity are lost as the aggregating particles reach a size and mass that is sufficient to induce settling.

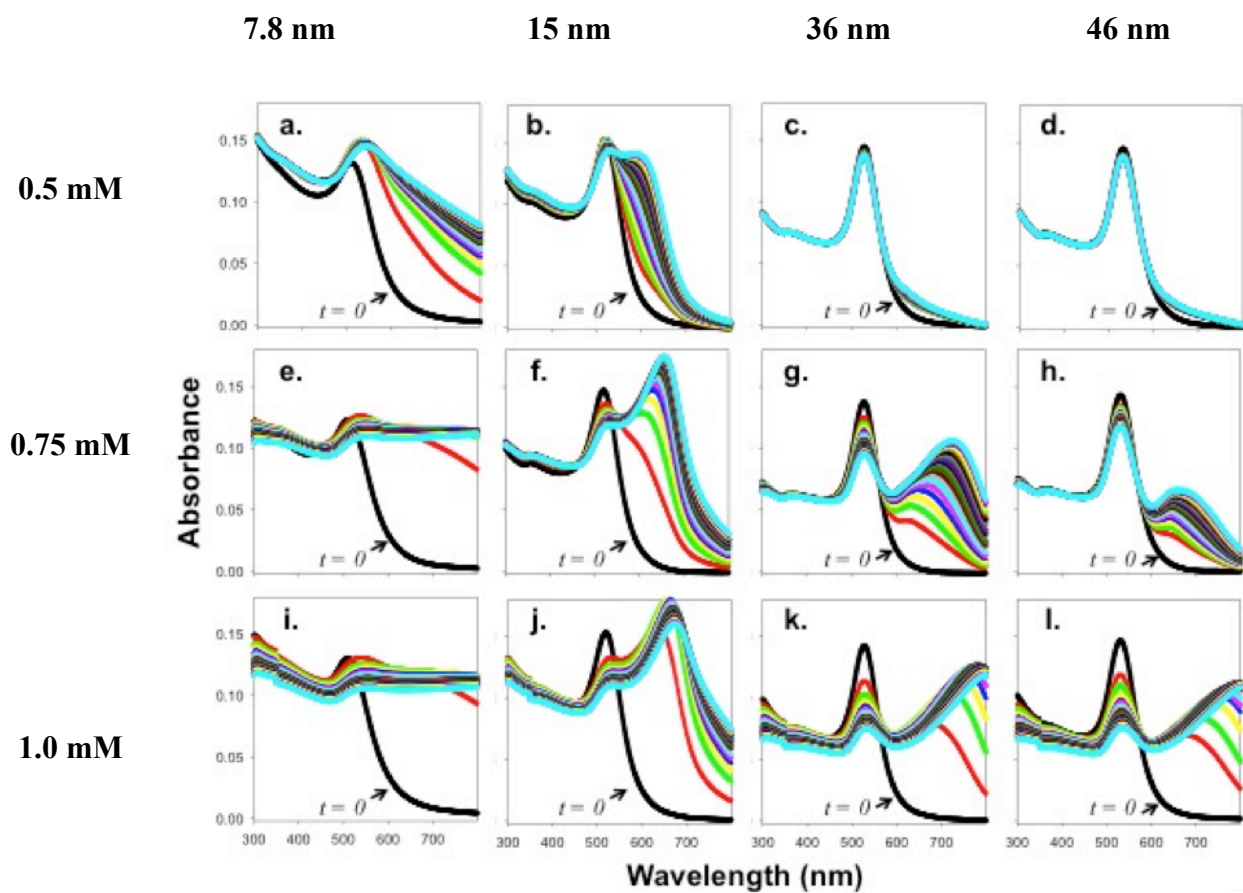


Figure 2-6. Matrix showing changes in the UV-Vis spectra of four different sizes of cit-AuNP at normalized mass concentration of 10 mg L^{-1} as Au after 60 minutes in MgSO₄ concentrations of 0.5 to 1.0 mM. Note: The $t = 0$ scan is black in color and denoted by a black arrow; final scans ($t = 60 \text{ min.}$) are light blue in color.

Relationship between UV-Vis spectra and hydrodynamic diameter. Although past studies have investigated the aggregation of metallic nanoparticles using DLS or UV-Vis separately,^{7, 31, 32} relatively few have attempted to relate the results obtained by the two complementary techniques. To our knowledge no studies have compared DLS and UV-Vis results obtained during an aggregation process. In their study evaluating the interaction of differentially surface-functionalized gold nanoparticles with organic matter, Diegoli et al. did report that DLS and TEM measures of particle diameter as a function of pH and surface coating were in good general agreement with results obtained by UV-Vis spectroscopy.⁶ Doak et al⁴ investigated the effect of variable particle diameter (1 to 10 nm radius) on the single particle absorbance spectra of gold nanoparticles and observed good semi-quantitative fits of DLS-determined size distributions to UV-Vis absorbance spectra.

Comparing aggregation rates determined by DLS with those obtained by UV-Vis spectroscopy may offer important insights into aggregation processes, particularly changes in interparticle distances and to a lesser extent, the localized dielectric environment surrounding particles, that occur prior to the formation and subsequent growth of nanoparticle clusters. To relate DLS and UV-Vis based measures of cit-AuNP aggregation, we mixed 46 nm cit-AuNP with MgSO₄ at concentrations ranging from 0 to 4 mM, and then compared observed and initial optical absorbance values at the LSPR band ($Ab_{LSPR,obs}:Ab_{LSPR,init}$ ratio) to relative changes in hydrodynamic diameter ($Z_{Avg,obs}/Z_{Avg,init}$) as measured by TR-UV-Vis and TR-DLS, respectively. As shown in Figure 2-7, a strong negative correlation exists between Ab_{LSPR} and Z_{Avg} , indicating that a decrease in Ab_{LSPR} measured by UV-Vis is a highly sensitive predictor of increasing cluster size as determined by DLS.

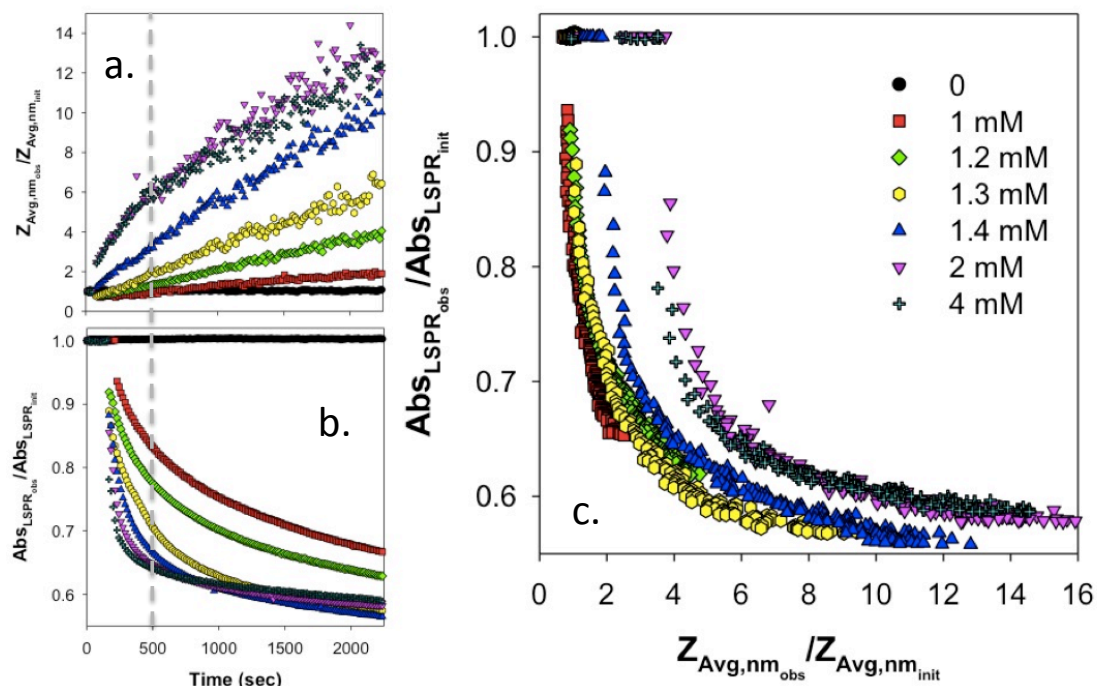


Figure 2-7. Relationship between hydrodynamic diameter ($Z_{Avg,nm}$) and absorbance at the LSPR band (Abs_{LSPR}) for 46 nm cit-AuNP (at a mass concentration of 10 mg L^{-1} as Au) across a range of $MgSO_4$ concentrations. Panels (a) and (b) show the relative change in $Z_{Avg,nm}$ as measured by DLS and $Abs_{LSPR1}:Abs_{LSPR2}$ as measured by UV-Vis spectroscopy (and normalized against t_0 values), respectively, across a range of $MgSO_4$ concentrations over time. Note, the vertical dotted line across panels (a) and (b) denotes the first 8 min. of the experiment, which is explained in greater detail in Fig. 2-8. Panel (c) shows the inverse, concentration-dependent relationship between Abs_{LSPR} and $Z_{Avg,nm}$.

The dashed line at 500 sec in Figure 2-7a,b separates two distinct aggregation regimes that can be defined based on the time required to achieve the maximum response measured by UV-Vis (change in LSPR) or DLS (increase in $Z_{ave,d}$) over the duration of the assay. These regimes are illustrated conceptually in Figure 2-8. Regime 1 (Figure 2-8a) describes the decrease in interparticle distance that precedes cluster formation. For optically active metallic nanoparticles, this regime can be effectively examined by the TR-UV-Vis technique, which reaches >90% of its maximum response within the first eight minutes of the experiment for these conditions. Since the shift of the LSPR measured by TR-UV-Vis is at its maximum when interparticle distance is at its minimum,²⁹ we can conclude that within this initial eight minute

period interparticle spacing has effectively been reduced to ‘zero’ and the majority of free cit-AuNP monomers present in the pristine suspension are now components of dimers and growing multi-particle clusters. At this point, the efficacy of the TR-UV-Vis technique is reduced and the value of the TR-DLS technique becomes more apparent. The remaining duration of the experiment represents Regime 2 (Figure 2-8b), which describes the subsequent increase in cluster size that occurs after interparticle distances have reached ‘zero’ and cluster growth continues to occur. As shown in Figure 2-7a, Regime 2 represents a significant period of the aggregation process as cluster size more than doubles based on hydrodynamic diameter. For the 46 nm cit-AuNP, diffusion-limited conditions are met at 2 mM MgSO₄, as there is little change in the TR-UV-Vis and TR-DLS responses between 2 and 4 mM MgSO₄ (Figure 2-8)

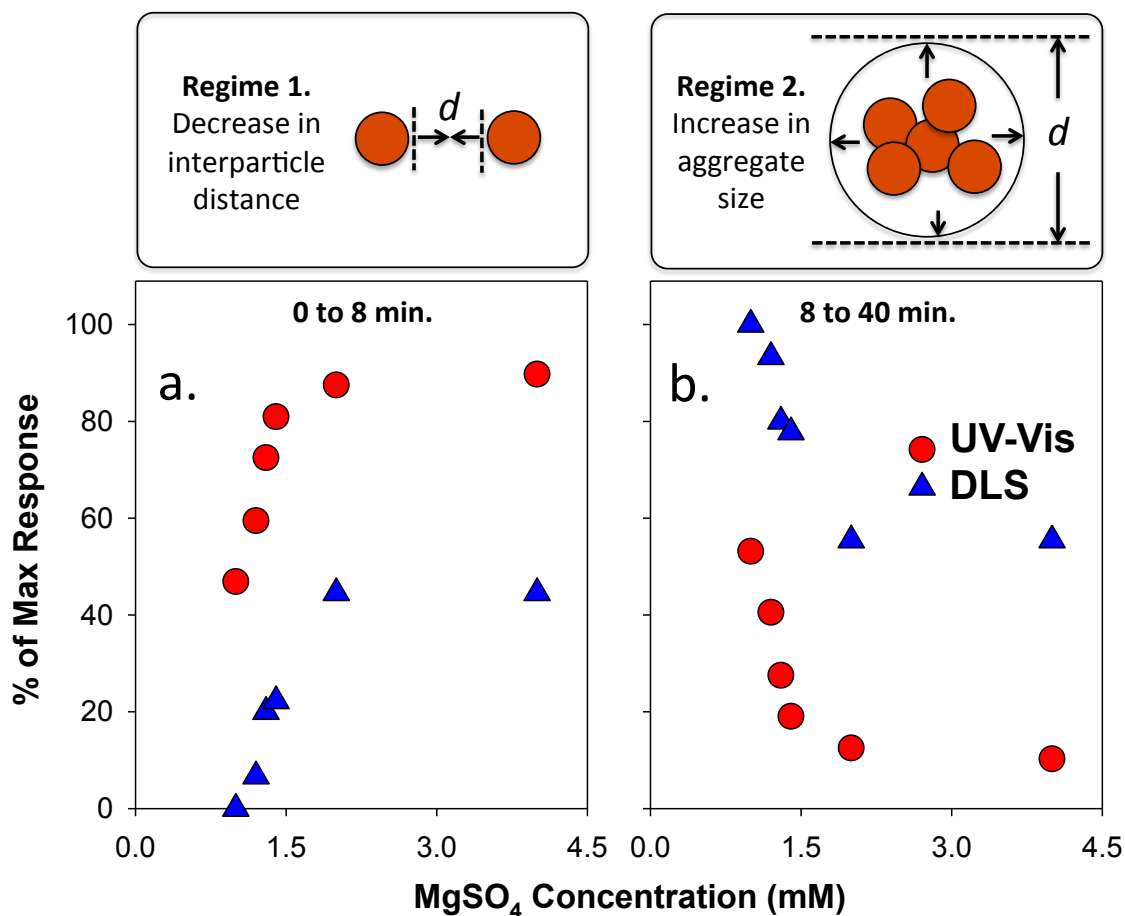


Figure 2-8. Comparison of aggregation regimes separated by the dashed line in Fig. 2-7 and defined by (a) decreasing interparticle distance and (b) increasing cluster size.

In summary, we show that in a divalent electrolyte solution at a fixed ionic strength and mass-normalized particle concentrations (10 mg L^{-1} as Au) that aggregation rates for cit-AuNP increase with a decrease in primary particle diameter. The experimental results qualitatively agree with DLVO theory, which predicts that a decrease in particle diameter will lower the interaction energy barrier, thus increasing the propensity for small particles to aggregate more rapidly than larger particles. Nanoparticle concentrations play an important role in governing aggregation behavior, however, and aggregation rates of large particles exceed those of smaller particles when nanoparticle concentrations are normalized by particle number. Upon surface area

normalization, however, and under diffusion-limited conditions, aggregation rate constants are effectively identical. Results of time-course UV-Vis spectroscopy, when interpreted in the context of Generalized Multiparticle Mie (GMM) theory, support DLS results and show that interparticle distances derived from changes in LSPR behavior decrease at a rate inversely proportional to primary particle diameter. Collectively, these results can be used to define two distinct aggregation regimes—the first (Regime 1) representing the initial decrease in interparticle spacing that occurs shortly after addition of electrolyte to an optically active metallic colloid, and the second (Regime 2) occurring thereafter as a function of cluster growth—that can be effectively measured by the integration of TR-UV-Vis and TR-DLS, respectively. These results have important implications on the characterization of optically active metallic nanoparticles in biological and environmental systems, where aggregation processes may alter environmental fate and transport, biological uptake, or particle interactions with cellular machinery.

2.5 Acknowledgments

We are grateful for funding from the US National Science Foundation (BES 0853989) and the Virginia Tech Institute for Critical Technology and Applied Science. This material is based upon work supported by the National Science Foundation (NSF) and the Environmental Protection Agency (EPA) under NSF Cooperative Agreement EF-0830093, Center for the Environmental Implications of NanoTechnology (CEINT). Any opinions, findings, conclusions or recommendations expressed in this material are those of the authors and do not necessarily reflect the views of the NSF or the EPA. This work has not been subjected to EPA review and no official endorsement should be inferred.

2.6 Supporting Information

Characterization: d_{TEM} and d_{DLS} discrepancy

For the largest particles ($d_{TEM} = 46$ nm), a discrepancy between the TEM and DLS determined diameters may be attributable in part to the fact that some particles of this size are not perfectly spherical and instead exhibit a semi-spherical or ellipsoidal shape (Figure 2-S1).

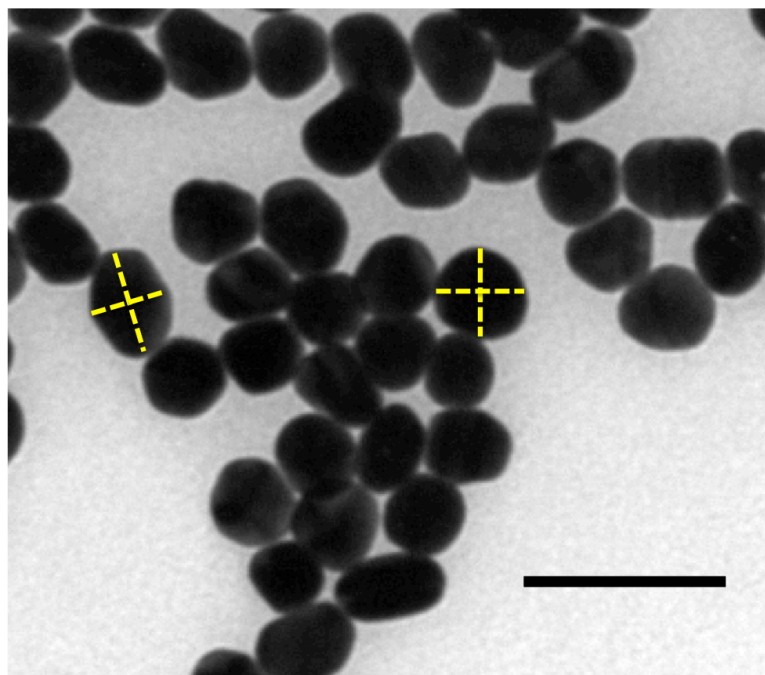


Figure 2-S1. TEM image showing the spherical and semi-spherical (ellipsoidal) geometry of citrate-AuNP ($d_{TEM} = 46$ nm). Perpendicular dashed lines denote the lateral and longitudinal dimensions of select particles.

2.7 References

1. Willets, K.; Van Duyne, R., Localized surface plasmon resonance spectroscopy and sensing *Annu Rev Phys Chem* **2007**, 58, 267-297.
2. Nehl, C.; Hafner, J., Shape-dependent plasmon resonance of gold nanoparticles. *Journal of Materials Chemistry* **2008**, 18, 2415-2419.

3. Mie, G., Beiträge zur optic trüber medien, speziell kolloidaler metallösungen. *Ann Phys* **1908**, 330, 377-445.
4. Doak, J.; Gupta, R.; Manivannan, K.; Ghosh, K.; Kahol, P., Effect of particle size distributions on absorbance spectra of gold nanoparticles. *Physica E* **2010**, 42, 1605-1609.
5. Krasovskii, V.; Nagovitsyn, I.; Chudinova, G.; Savranskii, V.; Karavanskii, V., Interaction of gold nanoparticles with bovine serum albumin. *Bulletin of the Lebedev Physics Institute* **2007**, 34 (11), 321-324.
6. Diegoli, S.; Manciulea, A.; Begum, S.; Jones, I.; Lead, J.; Preece, J., Interaction between manufactured gold nanoparticles and naturally occurring organic macromolecules. *Science of the Total Environment* **2008**, 402, 51-61.
7. Kim, T.; Lee, C.-H.; Joo, S.-W.; Lee, K., Kinetics of gold nanoparticle aggregation: experiments and modeling. *Journal of Colloid and Interface Science* **2008**, 318, 238-243.
8. Derjaguin, B.; Landau, L., Theory of the stability of strongly charged lyophobic sols and of the adhesion of strongly charged particles in solutions of electrolytes. *Acta Physico Chemica URSS* **1941**, 14, 633.
9. Verwey, E.; Overbeek, J., *Theory of the stability of lyophobic colloids*. Elsevier: Amsterdam, 1948.
10. Link, S.; El-Sayed, M., Spectral properties and relaxation dynamics of surface plasmon electronic oscillations in gold and silver nanodots and nanorods. *Journal of Physical Chemistry B* **1999**, 103, 8410-8426.
11. Mornet, S.; Vasseur, S.; Grasset, F.; Duguet, E., Magnetic nanoparticle design for medical diagnosis and therapy. *Journal of Materials Chemistry* **2004**, 14, 2161-2175.
12. Brant, J.; Lecoanet, H.; Wiesner, M., Aggregation and deposition characteristics of fullerene nanoparticles in aqueous systems. *Journal of Nanoparticle Research* **2005**, 7 (4-5), 545-553.
13. Labille, J.; Brant, J., Stability of nanoparticles in water. *Nanomedicine* **2010**, 5 (6), 985-998.
14. Chen, K.; Elimelech, M., Influence of humic acid on the aggregation kinetics of fullerene (C60) nanoparticles in monovalent and divalent electrolyte solutions. *J. Colloid Interface Sci.* **2007**, 309, 126-134.

15. Chen, K.; Mylon, S.; Elimelech, M., Aggregation kinetics of alginate-coated hematite nanoparticles in monovalent and divalent electrolytes. *Environmental Science & Technology* **2006**, 40 (5), 1516-1523.
16. Holthoff, H.; Egelhaaf, S.; Borkovec, M.; Schurtenberger, P.; Sticher, H., Coagulation rate measurements of colloidal particles by simultaneous static and dynamic light scattering. *Langmuir* **1996**, 12, 5541-5549.
17. Mulvihill, M.; Habas, S.; Plante, I.; Wan, J.; Mokari, T., Influence of size, shape, and surface coating on the stability of aqueous suspensions of CdSe nanoparticles. *Chemistry of Materials* **2010**, 22, 5251-5257.
18. Mylon, S.; Chen, K.; Elimelech, M., Influence of natural organic matter and ionic composition on the kinetics and structure of hematite colloid aggregation: implications to iron depletion in estuaries. *Langmuir* **2004**, 20, 9000-9006.
19. Yang, Y.; Matsubara, S.; Nogami, M.; Shi, J., Controlling the aggregation behavior of gold nanoparticles. *Materials Science and Engineering B* **2007**, 140, 172-176.
20. MacCuspie, R., Colloidal stability of silver nanoparticles in biologically relevant conditions. *Journal of Nanoparticle Research* **2010**, Online first.
21. Haiss, W.; Thanh, N.; Aveyard, J.; Fernig, D., Determination of size and concentration of gold nanoparticles from UV-Vis spectra. *Analytical Chemistry* **2007**, 79, 4215-4221.
22. Jana, N.; Gearheart, L.; Murphy, C., Wet chemical synthesis of high aspect ratio cylindrical gold nanorods. *J. Phys. Chem. B* **2001**, 105, 4065-4067.
23. Turkevich, J.; Stevenson, P. C.; Hillier, J. A., Study of the nucleation and growth processes in the synthesis of colloidal gold. *Discuss. Faraday Soc.* **1951**, 11, 55-59.
24. Frens, G., Controlled nucleation for the regulation of the particle size in monodisperse gold suspensions. *Nature Physical Science* **1973**, 241, 20-22.
25. Ji, X.; Song, X.; Li, J.; Bai, Y.; Yang, W.; Peng, X., Size control of gold nanocrystals in citrate reduction: the third role of citrate. *J. Am. Chem. Soc.* **2007**, 129 (45), 13939-13948.
26. USEPA, 600/4-91-010 Methods for the determination of metals in environmental samples. **1991**.
27. He, T.; Wan, J.; Tokunaga, T., Kinetic stability of hematite nanoparticles: the effect of particle sizes. *Journal of Nanoparticle Research* **2008**, 10, 321-332.

28. Xu, Y.; Gustafson, B., A generalized multiparticle Mie-solution: further experimental verification. *Journal of Quantitative Spectroscopy and Radiative Transfer* **2001**, 70 (4-6), 395-419.
29. Zhong, Z.; Patskovskyy, S.; Bouvrette, P.; Luong, J.; Gedanken, A., The surface chemistry of Au colloids and their interactions with functional amino acids. *Journal of Physical Chemistry B* **2004**, 108 (13), 4046-4052.
30. Xu, Y., Electromagnetic scattering by an aggregate of spheres: far field. *Applied Optics* **1997**, 36 (36), 9496-9508.
31. Storhoff, J.; Lazarides, A.; Mucic, R.; Mirkin, C.; Letsinger, R.; Schatz, G., What controls the optical properties of DNA-linked gold nanoparticle assemblies. *Journal of the American Chemical Society* **2000**, 122 (19), 4640-4650.
32. Burns, C.; Spindel, W.; Puckett, S.; Pacey, G., Solution ionic strength effect on gold nanoparticle solution color transition. *Talanta* **2006**, 69 (4), 873-876.

Chapter 3. Quantifying the persistence of noble metallic nanoparticles (MetNPs) in aqueous matrices

M.S. Hull^{1,2,3}, R.I. MacCuspie⁴, and P.J. Vikesland^{1,2,3}

¹Virginia Tech, Department of Civil and Environmental Engineering, Blacksburg, Virginia, USA

²Virginia Tech Institute for Critical Technology and Applied Science (ICTAS)

³Center for the Environmental Implications of Nanotechnology (CEINT)

⁴Nanomechanical Properties Group, Ceramics Division, National Institute of Standards and Technology, Gaithersburg, MD, USA

3.1 Abstract

Currently no information is available to describe the persistence of nanoscale materials in biological and environmental systems. Herein, we define an approach to quantify the persistence of noble metallic nanoparticles (MetNPs) in aqueous matrices in a context relevant to the National Nanotechnology Initiative's (NNI) definition of nanoscale materials: *at least one dimension of 1 to 100 nm and novel properties stemming from small size*. Our approach is based upon spectral monitoring of the bathochromic shift and subsequent loss of the localized surface plasmon resonance (LSPR) behavior of MetNPs, which is a unique nanoscale phenomenon attributable to the existence of free, unaggregated nanoparticles in suspension. Previously, we used time-resolved UV-Vis spectroscopy (UV-Vis) and Dynamic Light Scattering (DLS) to demonstrate that changes in LSPR behavior are related to a) an increase in the size of MetNP clusters and b) the loss of unique nanoscale optical properties. The current study examines the

use of LSPR activity monitoring as an approach to quantify the half-lives of nanoscale gold and silver MetNPs in aqueous systems. The applicability of this approach to quantify the persistence of gold and silver nanoparticles with common surface coatings and in different aquatic media is considered. Our results have implications on the development of metrics to characterize the persistence of noble metal nanoparticles in biological and environmental systems.

3.2 Introduction

Progress on engineering and manufacturing diverse forms of nanoscale materials and their subsequent integration into consumer products continues to advance rapidly. Estimates suggest that as of 2010, over 1300 products identified as containing nanoscale materials are commercially available, while less than 100 were available in 2005.¹ Although these numbers are estimates based on manufacturer-reported information, they suggest a clear trend in the growing significance of nanoscale technologies worldwide. Amidst widespread development and commercialization of emerging nanotechnologies have come calls from stakeholders to increase funding for research on nanoscale hazards,² and to bolster regulatory oversight of products integrating engineered nanomaterials.³ In many cases, particularly in the European Union and in the United States, these calls have been met with increased support for research investigating the interactions of nanoscale materials with biological and environmental systems.⁴ Regulatory responses have ranged from federal implementation of voluntary reporting schemes for nanomanufacturers^{5, 6} to stringent local requirements for entities engaged in nanotechnology-related activities.⁷

One class of nanoscale materials being broadly incorporated into commercial products is noble metallic nanoparticles (MetNPs), which includes gold and silver nanoparticles (AuNP and AgNP, respectively). Cancer therapies based on AuNP are currently in clinical trials,⁸ and AgNPs have been incorporated in a growing number of consumer products due to their well-established antimicrobial properties.^{9, 10} A feature that makes MetNPs attractive for commercial use, particularly for bioimaging and biosensing applications, is that many MetNPs possess unique optical behavior arising from a nanoscale phenomenon known as localized surface plasmon resonance (LSPR). This phenomenon occurs “when an electromagnetic field drives the collective oscillations of a nanoparticle’s free electrons into resonance.”¹¹ Mie described this effect in the early 1900’s for small metallic spheres surrounded by a dielectric medium.¹² The resonance condition for gold and silver nanospheres, which is fixed by the relationship between the dielectric constant of the surrounding medium and the dielectric function of the metal, is satisfied at visible wavelengths of the electromagnetic spectrum.¹¹ In water, the LSPR wavelength for ≈ 20 nm gold spheres occurs at 520 nm, but as the diameter increases to ≈ 100 nm, the LSPR wavelength bathochromically shifts (i.e., red-shifts) to ≈ 600 nm.

Red-shifts of the LSPR band are also indicative of aggregation processes, as has been demonstrated previously.^{13, 14} In these studies, as first described by Derjaguin, Landau, Verwey, and Overbeek (DLVO),^{15, 16} electrolyte-induced collapse of the electrostatic double layer repelling charged particles leads to the coupling and subsequent aggregation of gold nanoparticle monomers. As the monomers form dimers and polymers, the growing clusters induce a red-shift in the LSPR that is similar to that observed for large-diameter monomers. Eventually, the LSPR

is no longer observed as the growing clusters settle out of suspension and the novel optical activity of the once stable colloidal suspension is lost, in many cases, irreversibly.

Quantification of the persistence of chemicals in biological and environmental compartments plays an important role in risk assessment and the subsequent determination of a chemical agent's hazard potential.^{17, 18} Traditionally, half-life, or the time required for a chemical to decrease to half of its initial concentration or activity, has been used to quantify the persistence of compounds, and ultimately, to determine the need for regulatory instruments that mitigate human or environmental harm. In most instances, a compound's half-life—whether in the environment or in a specific biological compartment—is:

- i. based on degradation or loss of some measurable physicochemical property,¹⁹ and
- ii. facilitates some process of ranking and prioritization based either on efficacy (e.g., pharmaceuticals¹⁹) or hazard potential (i.e., pollutants¹⁹).

Engineered nanomaterials pose unique challenges to defining persistence in biological or environmental media. Exactly how does one define the half-life or persistence of a nanoscale particle? The added elements of size, three-dimensional structure, and novel behavior stemming from these physico-chemical properties add complexity to efforts focused on determining nanoparticle persistence. To illustrate this point, consider that the persistence of engineered nanomaterials can be defined by several different approaches including:

- i. *dissolution*, or the ratio of the respective dissolved and condensed phases relative to some initial condition;
- ii. *stability*, or the existence of the material in dispersed or colloidal form; and
- iii. *activity*, or the loss of the material's unique nanoscale behavior.

Given our current understanding of nanoscale materials, there is no clear approach as to how best to quantify the persistence of nanoscale particles in biological and environmental media. Dissolution, destabilization, and the subsequent loss of activity are all expected to play a role in altering the extent to which a particular nanoscale material conforms with the NNI definition of a nanoparticle—“*at least one dimension of 1-100 nm and novel behavior arising from existence at this size scale.*”²⁰

Dissolution and stability, respectively, serve as indicators of whether or not the dimensions of a particular nanomaterial meet the 1-100 nm specification of the NNI—for example, a particle dissolves to its ionic components (<1 nm) or an assemblage of particles aggregate irreversibly to form a larger structure (>100 nm). Nanoparticle dissolution, has proven to be a challenge to analytically quantify given the difficulties associated with distinguishing dissolved species from the smallest (e.g., 1-5 nm) nanoscale particulates,²¹ which may pose some of the most worrisome human and environmental health and safety concerns.²² Some progress has been made towards characterizing the dissolution behavior of silver nanoparticles by integrating techniques such as field flow fractionation with ICP-MS.²³ Liu and Hurt²⁴ examined the dissolution of ‘ion-free’ nanosilver colloids in aqueous systems and concluded that both thermodynamic analysis and kinetic measurements suggest that silver nanoparticles will not be

persistent under typical environmental conditions, particularly in the presence of oxygen. Still, challenges remain in precisely separating dissolved versus particulate forms of certain nanoscale materials, and while silver nanoparticles are expected to dissociate quite rapidly, MetNPs comprised of more inert metals like gold are likely to be much more persistent under ambient environmental and biological conditions.

Activity serves as an indicator of the extent to which a nanomaterial continues to possess unique nanoscale properties, such as novel optical or electromagnetic behavior. Unique LSPR activity is amongst the novel properties that have attracted interest in the use of MetNPs, particularly AuNPs and AgNPs, in a range of biological sensing²⁵ and therapeutic applications.²⁶ While these unique optical properties lend certain utility in such applications, they also provide an indicator of unique nanoscale activity that may be suitable for monitoring the persistence of MetNPs as NNI-defined nanoparticles in biological systems and the environment (Figure 3-1). Changes in the unique LSPR properties of MetNPs have been studied extensively, but to our knowledge, the loss of LSPR behavior has not yet been proposed as a means to quantify the MetNP persistence. As illustrated conceptually in Figure 3-1, the persistence of MetNPs in a biological or environmental system can be described by a sequence of steps beginning with destabilization and subsequent sedimentation of a pristine MetNP suspension. Eventually, or in some cases simultaneously, MetNP suspensions may undergo chemical dissolution resulting in the release of metal ions. Throughout this process, a MetNP suspension undergoes changes in a) size—aggregation or an increase in size, and/or dissolution or a reduction in size, and b) unique nanoscale activity. At some point, the MetNP suspension will no longer conform to the NNI definition of a nanoscale material as the measured particle size may be <1 nm (dissolved metal

ions) or >100 nm (sedimenting MetNP clusters) and novel nanoscale properties will no longer be measurable (e.g., loss of LSPR behavior). While loosely clustered MetNP monomers can be suspended by agitation through, for example, shaking and sonication, the disaggregation of aggregated MetNPs has not been reported previously.

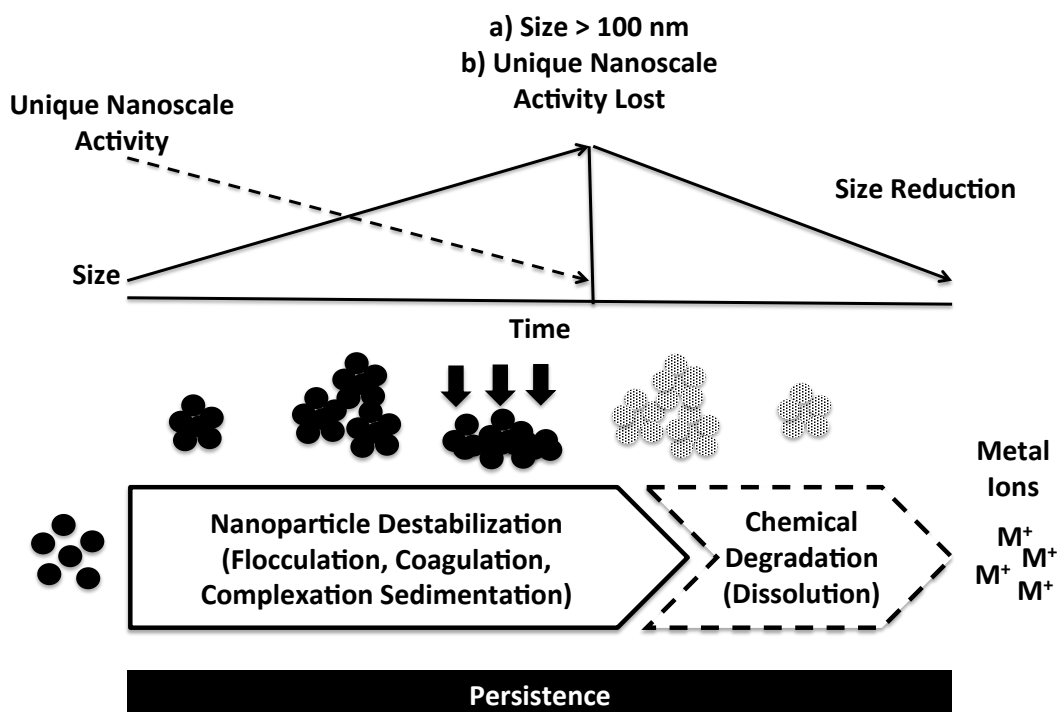


Figure 3-1. Conceptual figure illustrating the relationship between nanoparticle persistence in biological or environmental aqueous matrices and unique nanoscale activity.

Previously, we simultaneously utilized time-resolved DLS and UV-Vis spectroscopy to examine the stability and LSPR activity of citrate-stabilized gold nanoparticles (cit-AuNP) as a function of primary particle diameter (d_{TEM}) in media of varying electrolyte composition. The current study examines the applicability of monitoring the LSPR activity of gold and silver MetNPs as one approach to quantify the half-lives of nanoscale materials in aqueous systems.

3.3 Experimental Section

Preparation of MetNP suspensions. A total of six MetNP suspensions differing in noble metal composition (Au or Ag), primary particle diameter, and surface coating were prepared as summarized in Table 3-1. Reagent-grade sodium citrate tribasic dihydrate, 99% ($\text{Na}_3\text{C}_6\text{H}_5\text{O}_7 \cdot 2\text{H}_2\text{O}$), sodium borohydride (98%; NaBH_4), gold(III) chloride trihydrate ($\text{HAuCl}_4 \cdot 3\text{H}_2\text{O}$), silver nitrate, polyvinyl pyrrolidone (PVP), polyethylene glycol (PEG), ethylenediaminetetraacetic acid (EDTA), and bovine serum albumin (BSA) were obtained from Sigma-Aldrich (St. Louis, MO, USA). All reagents and nanoparticle suspensions were prepared in $>18 \text{ M}\Omega$ resistivity ultrapure water. Citrate-capped gold nanoparticles (cit-AuNP) of 15 nm diameter were prepared using the method of Turkevich.²⁷ Bovine serum albumin-coated gold nanoparticles (BSA-cit-AuNP) were prepared by incubating cit-AuNP with $0.1 \text{ mg BSA}\cdot\text{mL}^{-1}$ using established protocols.²⁸

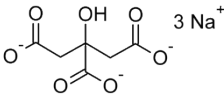
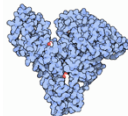
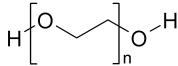
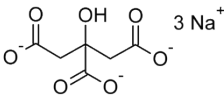
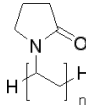
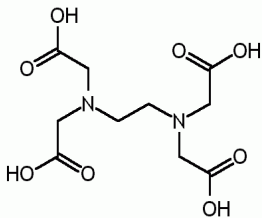
Polyethylene glycol (PEG) functionalized AuNP (PEG-AuNP) were prepared by attaching a heterofunctional thiolated/carboxylated PEG linker and thiolated PEG filler to cit-AuNP.²⁹ Briefly, heterofunctional HS-PEG-COOH at a ratio of 3,000 linker molecules per AuNP was added dropwise to a PBS (pH=7.4) buffered cit-AuNP suspension under rapid mixing. After 15 min, an excess of HS-PEG ($10 \mu\text{M}$) was added dropwise to fill the areas not covered by the linker. Assuming each thiolated-PEG molecule occupies $\approx 0.35 \text{ nm}^2$ of nanoparticle surface,³⁰ there were around 16,000 HS-PEG molecules conjugated to each AuNP. After reaction for 15 min, excess ligands were removed by five rounds of centrifugation and the final PEGylated AuNPs were resuspended in PBS.

Polyvinyl pyrrolidone (PVP) coated AgNPs (PVP-AgNP) were prepared by reduction of AgNO₃ in ethylene glycol (as solvent and reducing agent) with PVP added for stabilization. The raw reaction product was dialyzed against water to remove ethylene glycol and unbound PVP.

Ethylenediaminetetraacetic acid (EDTA) stabilized AgNPs (EDTA-AgNP) were prepared by adding 1 mL of 2.6×10^{-2} M AgNO₃ to a mixture containing 100 mL of 1.6×10^{-4} M EDTA and 4 mL of 0.1 M NaOH under vigorous stirring. Formation of EDTA-AgNP was indicated by the appearance of a faint yellow color that intensified after 2-4 minutes.

For the synthesis of cit-AgNP, 1.690 mL of 58.8 mM silver nitrate and 2.920 mL of 34 mmol·L⁻¹ tribasic sodium citrate dehydrate were added to 400 mL of boiling distilled water stirred at 600 rpm. Next, 2 mL of 100 mM sodium borohydride was added dropwise. A transition from colorless to yellow to brown was observed over the course of the sodium borohydride addition. The reaction was stirred for 30 minutes and allowed to cool to room temperature. The cit-AgNP product solutions were purified by stirred cell ultrafiltration using 10,000 MWCO regenerated cellulose filters, removing any unreacted reagents into the filtrate while the AgNPs remained in the retentate. Purified nitrogen gas provided the pressure for the stirred cell. Ultrafiltration resulted in an AgNP concentration of 1.0 mg mL⁻¹. Next, AgNP solutions were passed through a 0.2 μm PVDF syringe filter to remove dust or large aggregates. All suspensions were filtered (0.2 μm sterile vacuum filter), transferred to a glass vial, and stored in the dark at 4 °C until use.

Table 3-1. Summary of Au and AgNP suspensions prepared for the development and evaluation of a persistence metric for optically active MetNPs.

MetNP	d_{TEM} (nm)	Surface Coating
Cit-AuNP	15, 46	
BSA-cit-AuNP	46	
PEG-AuNP	46	
Cit-AgNP	20	
PVP-AgNP	20	
EDTA-AgNP	30	

Characterization. All MetNP suspensions were characterized by UV-Vis spectroscopy, transmission electron microscopy (TEM), and dynamic light scattering (DLS). Primary particle size and morphology were determined using a Zeiss 10CA Transmission Electron Microscope equipped with a high resolution (1024 × 1024 pixel format) MT Advantage GR/HR-B CCD Camera System (Advanced Microscopy Techniques Corp.). Voltage was kept at 60 kV for all samples. Samples were prepared by pipetting 10-20 μL of nanoparticle suspension onto a

carbon-coated copper TEM grid (Electron Microscopy Sciences) that was then air dried at room temperature. To assess the heterogeneity of the nanoparticle suspensions and to determine average primary particle diameters, electron micrographs were digitized and analyzed using ImagePro (MediaCybernetics, Bethesda, MD). Estimates of hydrodynamic diameter (Z-average) and electrophoretic mobility were obtained using a Malvern Zetasizer NanoZS (Malvern, UK). UV-Vis spectroscopy measurements were obtained using a Cary 5000 UV-Vis-NIR spectrophotometer (Agilent Technologies). Metal ion concentrations were measured using a Thermo Electron X-Series inductively coupled plasma-mass spectrometer (ICP-MS). Samples and calibration standards were prepared in a matrix of 2% aqua regia to minimize adsorption to sample tubing or internal instrument surfaces.

Evaluation of colloidal stability. In Chapter 2, the authors evaluated the colloidal stability of varying sizes of cit-AuNP suspensions using both time-resolved DLS (TR-DLS) and time-resolved UV-Vis spectroscopy (TR-UV-Vis). For the present work, TR-UV-Vis was used to evaluate the colloidal stability of MetNP suspensions with varying surface chemistries and in solutions of varying ionic composition. Briefly, MetNP suspensions were added to 1 cm cuvettes and then spiked with electrolyte solutions (0.15 to 30 mM) containing either sodium bicarbonate (NaHCO_3), potassium chloride (KCl), magnesium sulfate (MgSO_4), calcium sulfate (CaSO_4), or calcium chloride (CaCl_2). Following addition of electrolyte, the absorbance intensity of the localized surface plasmon resonance band (Abs_{LSPR}) of each MetNP suspension was monitored over time using either the kinetic ($\lambda = \text{LSPR}$) or kinetic scanning modes ($\lambda = 300\text{-}800$ nm) of the UV-Vis spectrophotometer. For all experiments, temperature was maintained at 25 °C by internal instrument controls. Experiments ranged in length from 10 to 60 minutes. All

experiments were performed at a mass-normalized MetNP concentration of approximately 10 mg L⁻¹ as [M⁺].

3.4 Results and Discussion

Determination of the optical absorbance persistence ratio (Abs_{LSPR1}:Abs_{LSPR2}). As defined in eq. 3-1, the optical absorbance persistence ratio represents the relationship between the absorbance intensity at the primary LSPR band (Abs_{λ=LSPR1}) and the absorbance intensity at a secondary, red-shifted LSPR band (Abs_{λ=LSPR2}) indicative of electrodynamic interactions between aggregating MetNPs and clusters. As an initial indicator of MetNP persistence as NNI-definable nanoscale materials, we can add a particular MetNP suspension to an electrolyte solution of interest (e.g., assay diluent, culture media) and measure the time required for the optical absorbance persistence ratio to decrease to one-half of its initial value. Values of Abs_{λ=LSPR1} are defined by the absorbance maximum of the LSPR band of the pristine MetNP suspension. Values for Abs_{λ=LSPR2} are defined based on observation of the bathochromic shift of the LSPR band upon electrolyte-induced aggregation of the MetNP suspension.

$$Abs_{LSPR1:LSPR2} Persistence Ratio = \frac{\left[\frac{Abs_{\lambda=LSPR1}}{Abs_{\lambda=LSPR2}} \right]_{observed}}{\left[\frac{Abs_{\lambda=LSPR1}}{Abs_{\lambda=LSPR2}} \right]_{initial}} \quad (3-1)$$

Comparing the decrease in absorbance intensity at Abs_{λ=LSPR1} to the increase in absorbance intensity at Abs_{λ=LSPR2}, makes it possible to define an Abs_{λ=LSPR1}:Abs_{λ=LSPR2} ratio that

quantitatively describes the aggregation behavior of optically active MetNPs as measured by UV-Vis spectroscopy. As noted earlier, others have previously described the aggregation behavior of cit-AuNP in aqueous systems,^{13, 14, 31} using both TR-UV-Vis and TR-DLS, but to our knowledge, the relationship between the primary and secondary LSPR bands of aggregating MetNP dispersions has not been applied as an indicator of MetNP persistence in electrolyte solutions.

Figure 3-2 illustrates the application of the $Ab_{LSPR1}:Ab_{LSPR2}$ persistence ratio for 15 nm citrate-AuNP (30 mg L^{-1} as Au). Pristine cit-AuNP of this diameter displays a characteristic primary LSPR band (LSPR1) centered at 520 nm. Upon addition of $750 \text{ }\mu\text{M}$ MgSO_4 to the cit-AuNP suspension, charge-shielding leads to the collapse of the repulsive double layer separating the cit-AuNP monomers.^{15, 16} Interparticle spacing decreases until ultimately, cit-AuNP begins to aggregate irreversibly. The decrease in interparticle spacing and eventual particle coupling results in electrodynamic interactions between the cit-AuNP monomers, which leads to the formation of a second bathochromically (“red”) shifted LSPR peak near 700 nm. To track the formation of this second LSPR peak relative to LSPR1, we define LSPR2, which occurs at a wavelength greater than LSPR1 and is determined based on the unique aggregation pattern of a particular MetNP suspension. Ideally, the increase in absorbance at LSPR2 should increase proportionally to the decrease in absorbance at LSPR1. As illustrated in Figure 3-2, we have defined LSPR2 as 600 nm, as the secondary LSPR band that occurs in this region increases proportionally to the decrease in the primary LSPR band centered at 520 nm. Over time, the cit-AuNP clusters reach diameters sufficient to induce their settling and removal from suspension, thus resulting in the irreversible loss of their unique nanoscale optical behavior.

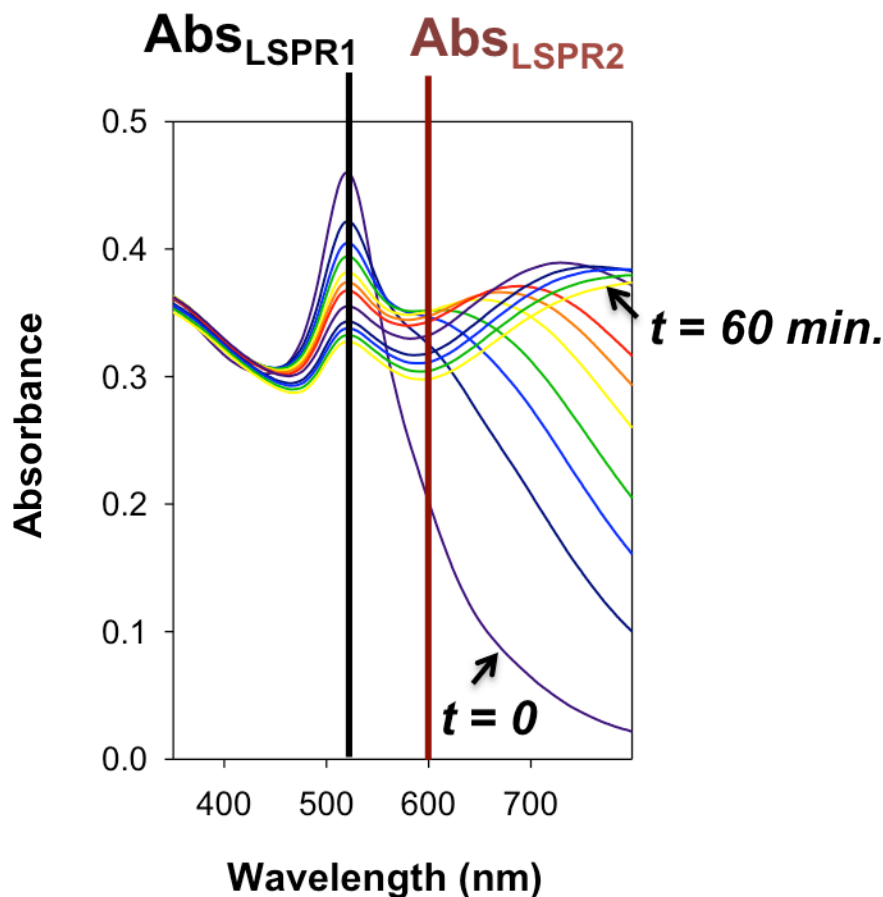


Figure 3-2. Results of TR-UV-Vis analysis of a 15 nm citrate-AuNP suspension (30 mg L^{-1} as Au) in $750 \text{ }\mu\text{M}$ MgSO_4 for 60 min. illustrating the relationship between $\text{Abs}_{\text{LSPR1}}$ and $\text{Abs}_{\text{LSPR2}}$. $\text{Abs}_{\text{LSPR1}}$ is determined based on the location of the primary LSPR band for the pristine MetNP suspension; $\text{Abs}_{\text{LSPR2}}$ is selected based on the unique plasmonic behavior (typically, a bathochromic or red-shift of the LSPR) displayed by the MetNP suspension upon aggregation in a particular medium.

Figure 3-3 plots the $\text{Abs}_{\text{LSPR1}}:\text{Abs}_{\text{LSPR2}}$ ratio for 15 nm cit-AuNP as a function of time in the presence of either MgSO_4 or CaSO_4 at $225 \text{ }\mu\text{M}$. This plot allows us to define the time required for the characteristic $\text{Abs}_{\text{LSPR1}}:\text{Abs}_{\text{LSPR2}}$ ratio for 15 nm cit-AuNP to reach 50% of its initial value after addition of MgSO_4 and CaSO_4 at $225 \text{ }\mu\text{M}$ as being ≈ 100 and 25 minutes, respectively. In other words, the optical persistence of 15 nm cit-AuNP is nearly four-fold greater in $225 \text{ }\mu\text{M}$ MgSO_4 relative to $225 \text{ }\mu\text{M}$ CaSO_4 .

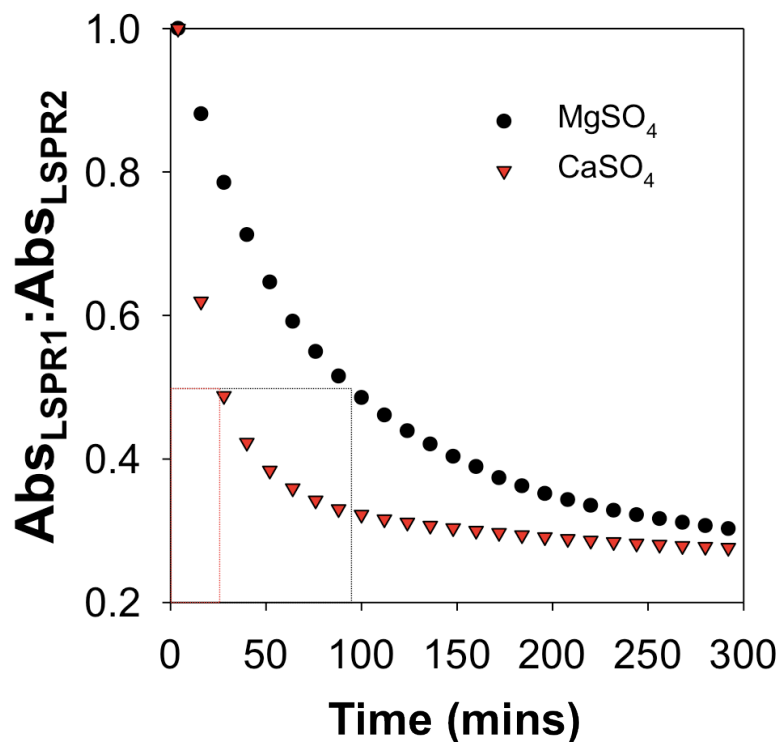


Figure 3-3. Comparison of time required for the $Abs_{LSPR1}:Abs_{LSPR2}$ ratio to decrease 50% for 15 nm cit-AuNP in 225 μM $MgSO_4$ or $CaSO_4$.

Effects of divalent electrolyte composition on Abs_{LSPR1} and Abs_{LSPR2} . As illustrated in Figure 3-3, the persistence of cit-AuNPs as optically-active nanoparticle suspensions varies between the divalent electrolytes. To investigate this phenomenon further, aggregation-induced changes in the LSPR behavior of 15 nm cit-AuNP were determined in three divalent electrolyte solutions, $MgSO_4$, $CaSO_4$, and $CaCl_2$ at ionic strengths ranging from 150 to 250 μM . Electrolyte solutions were mixed with 15 nm cit-AuNP and the absorbance between 200 and 800 nm was monitored at 25 °C for a period of 12 h. At electrolyte concentrations above 200 μM , both $MgSO_4$ and $CaSO_4$ induced measurable changes in the LSPR behavior of 15 nm cit-AuNP. These changes include a decrease in Abs_{LSPR1} ($\lambda=520$ nm) coupled with an increase in Abs_{LSPR2} ($\lambda=600$ nm).

nm) (Figure 3-4). The formation kinetics of the secondary LSPR band are dependent on both the dominant cation present (Ca^{2+} or Mg^{2+}) as well as the salt concentration (150, 200, 250 μM).

At equivalent concentrations, Ca^{2+} induces a more dramatic affect than Mg^{2+} across the time and concentration range investigated (Figure 3-4). Ca^{2+} has a slightly larger ionic radius than Mg^{2+} (100 vs. 72 pm),³² and larger counter-ions are generally thought to enhance colloidal stability by “*increasing the distance of closest approach for two colloids to twice the diameter of the counter*”,^{33,34} but this does not appear to hold for Ca^{2+} and Mg^{2+} . Laaksonen et al³⁴ report that zeta potentials become less negative with increasing counter-ion size, which they attribute to more efficient shielding of the negatively charged AuNP surfaces. In their study of gold nanoparticle interactions with natural organic matter, Stankus et al³⁵ report that Ca^{2+} is more effective than Mg^{2+} at inducing aggregation of negatively charged AuNP, and they attribute this result to the fact that Ca^{2+} (electronegativity = 1.00 Pauling units) is slightly more electropositive than Mg^{2+} (1.31 Pauling units). Based on results of our UV-Vis studies comparing divalent electrolytes, it appears that between these divalent cations, electronegativity plays an important role in modulating the aggregation behavior of negatively charged colloids.

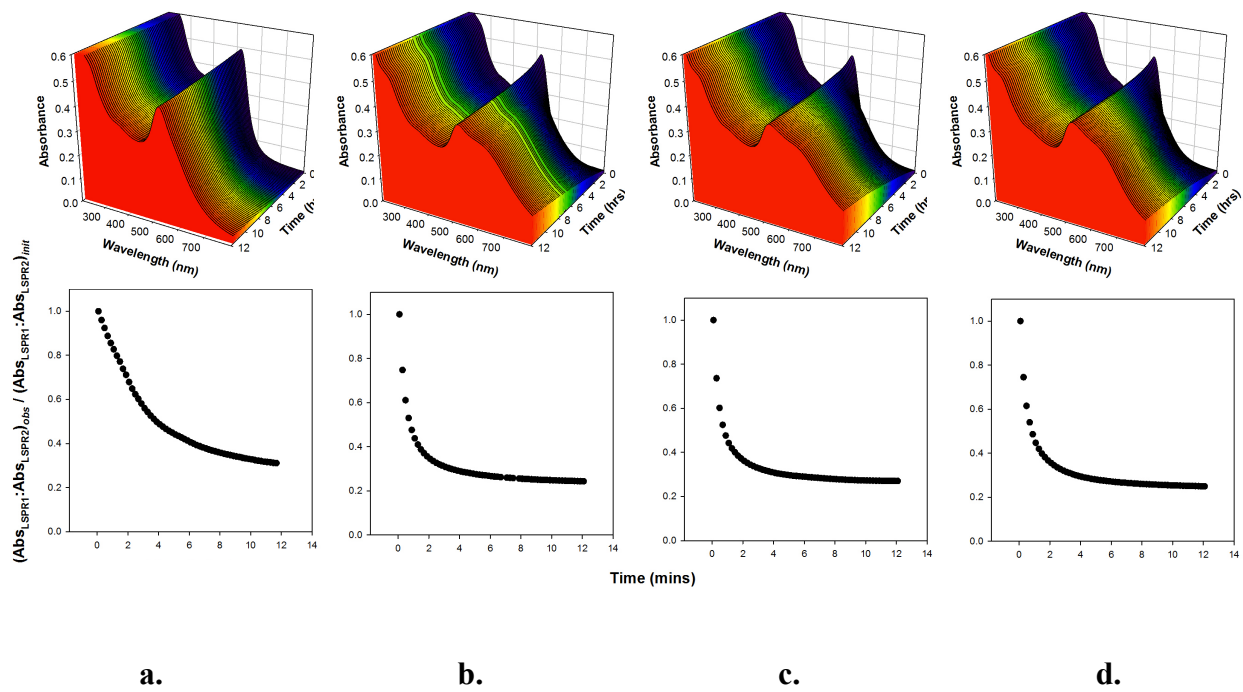


Figure 3-4. Panels a-d (top) show 3D plots summarizing the effect of varying electrolyte composition on the UV-Vis spectral properties of 15 nm cit-AuNP during 12 h incubation with 200 μM (a) MgSO_4 , (b) CaSO_4 , (c) CaCl_2 , and (d) mixed CaCl_2 and NaCl concentration. Corresponding plots showing the change in the LSPR_{1, $\lambda=520$ nm} to LSPR_{2, $\lambda=600$ nm} ratio for each electrolyte are also shown (bottom).

Comparison of $Abs_{LSPR1}:Abs_{LSPR2}$ for Au and AgNPs with variable surface coatings: The functionalization of MetNPs with materials such as proteins, polymers, and other macromolecules has been shown to enhance MetNP stability in high ionic strength media.^{36, 37} For example, the blood half-life of a nanopharmaceutical was prolonged by incorporation into a carrier molecule,³⁸ and Yang and co-workers³⁹ reported on the importance of extending the half-lives and in vivo circulation times of core-shell magnetic nanoparticles used for targeted delivery of chemotherapeutic agents to gliomas occurring in the brain and spine.

Figure 3-5 shows spectral plots obtained by TR-UV-Vis spectroscopy for six MetNP suspensions following addition of US EPA moderately hard synthetic freshwater (EPA MHS). At $t = 0$ min., the primary LSPR band of the pristine cit-AuNP suspension ($d_{TEM} = 46$ nm) was centered at 530 nm. Less than 10 min. after addition of EPA MHS, absorbance intensity at 530 nm ($Abs_{\lambda=530 \text{ nm}}$) decreased and a secondary LSPR band centered at 663 nm appeared. Absorbance intensity at this secondary band ($Abs_{\lambda=663 \text{ nm}}$) increased over the 120 min. assay period. As noted earlier, the formation of the second LSPR band is indicative of a decrease in interparticle spacing and subsequent electrodynamic interactions between particles that occur as a result of charge-shielding and subsequent collapse of the double layer separating individual-stabilized MetNPs. Addition of either a protein (BSA) or a polymer (PEG) surface coating dramatically increased the stability of AuNP over the duration of the assay. Both of these molecules are relatively bulky and are capable of providing electrostatic and/or steric (i.e., electrosteric) particle stabilization, each of which effectively prevents any decrease in interparticle spacing. The primary LSPR bands of pristine BSA- and PEG-AuNP ($d_{TEM} = 46$ nm) were centered at 535 and 532 nm, respectively, and are bathochromically shifted relative to cit-AuNP (530 nm) due to the effect of these coatings on the local refractive index in the vicinity of

the gold nanospheres.⁴⁰ Unlike cit-AuNP, however, there was no indication of an appreciable decrease in Ab_{LSPR1} , nor was there evidence of formation of a secondary bathochromically-shifted LSPR band. The primary LSPR band of the pristine cit-AgNP suspension was centered at 389 nm. Immediately following addition of EPA MHS, absorbance intensity at 389 nm decreased rapidly and a bathochromically shifted secondary LSPR band appeared near 600 nm. Addition of PVP and EDTA had a stabilizing effect on AgNP that was similar to that observed for BSA and PEG stabilization of AuNP. Primary LSPR bands for PVP- and EDTA-AgNP were centered at 405 and 427 nm, respectively, with no indication of a secondary LSPR band forming after 120 min.

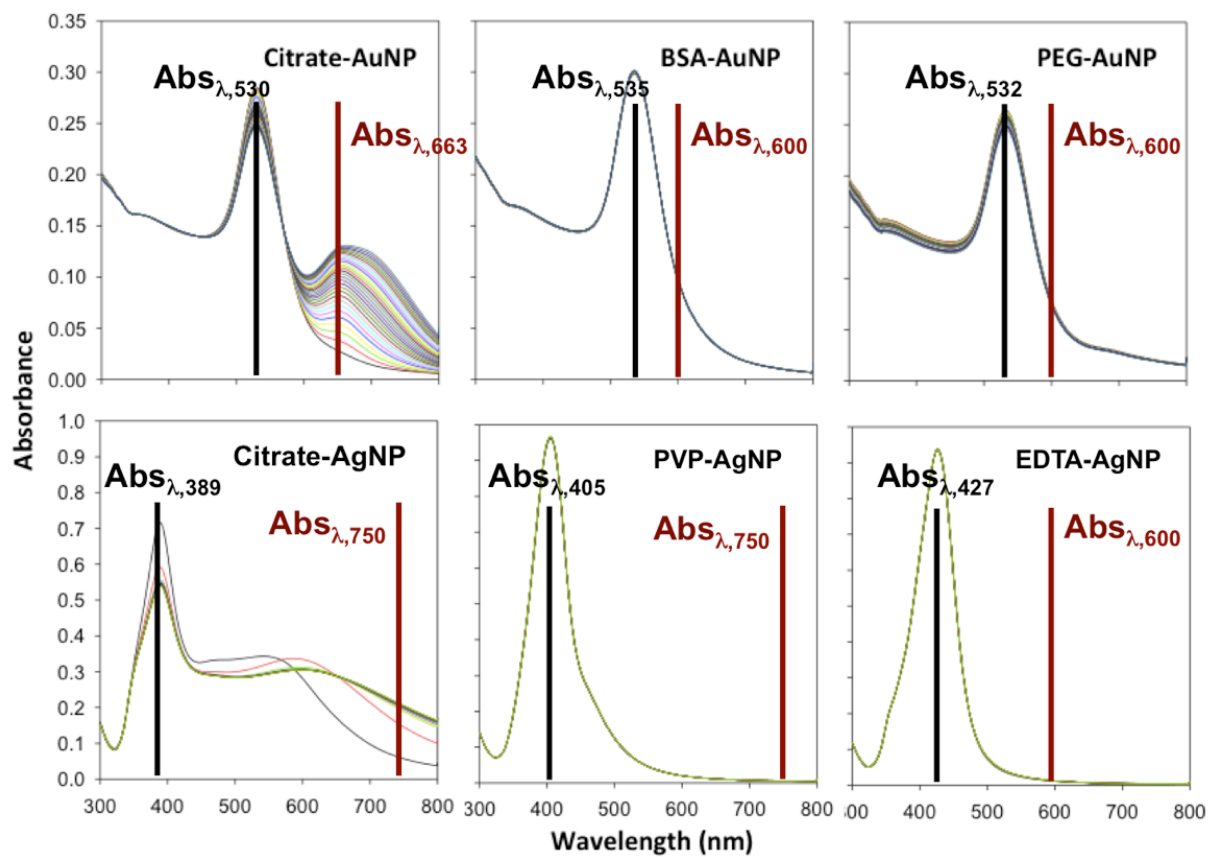


Figure 3-5. Comparison of TR-UV-Vis spectral plots for six different MetNP suspensions mixed with EPA MHS. MetNP concentrations were normalized at 10 mg L^{-1} as M^+ . $\text{Abs}_{\text{LSPR1}}$ and $\text{Abs}_{\text{LSPR2}}$ for individual MetNP suspensions are noted on the spectral plots.

Plotting the $\text{Abs}_{\text{LSPR1}}:\text{Abs}_{\text{LSPR2}}$ ratios of the six MetNPs shown in Figure 3-5 permits quantitative comparison of the persistence of the novel optical behavior of each MetNP suspension in EPA MHS freshwater (Figure 3-6). From these plots, MetNP persistence can be observed based on the loss of nanoscale optical activity. The optical behavior of citrate-capped Au and AgNP was least persistent in EPA MHS, reaching 50% of the initial $\text{Abs}_{\text{LSPR1}}:\text{Abs}_{\text{LSPR2}}$ value within ≈ 4 and 11 minutes, respectively. This suggests that upon addition to EPA MHS, the interparticle spacing between adjacent cit-AuNP and cit-AgNP monomers decreased rapidly, leading to aggregate formation and subsequent loss of LSPR activity. Optical activity of Au and AgNPs stabilized by polymer and protein coatings, however, was highly persistent in EPA MHS, as the $\text{Abs}_{\text{LSPR1}}:\text{Abs}_{\text{LSPR2}}$ ratio remained at unity throughout the duration of the assay. Optical activity of EDTA-AgNP was intermediately persistent, as evidenced by a distinct decrease in the $\text{Abs}_{\text{LSPR1}}:\text{Abs}_{\text{LSPR2}}$ ratio.

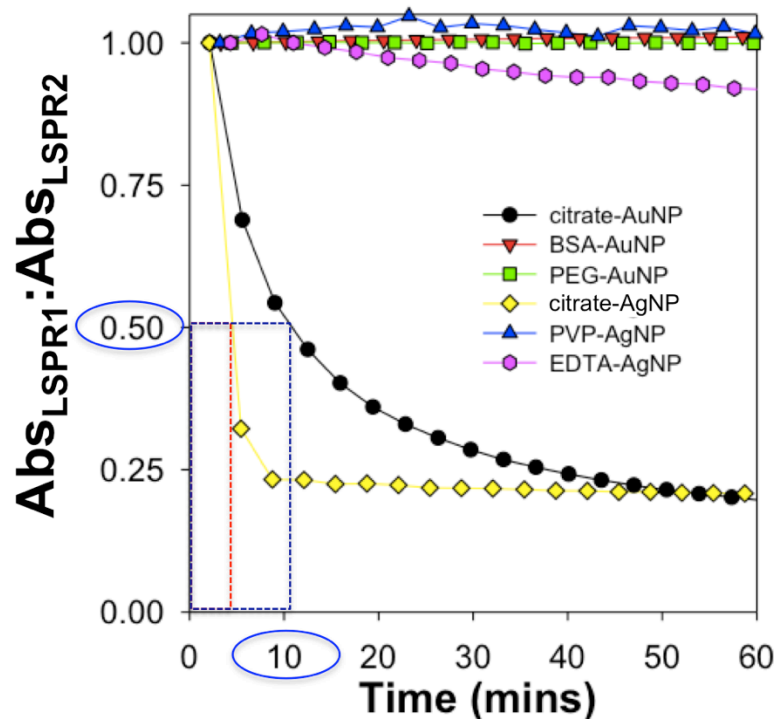


Figure 3-6. Plot showing the decline of the $Abs_{LSPR1}:Abs_{LSPR2}$ ratio for six MetNPs with differing surface coatings following addition to EPA MHS freshwater.

Although a number of approaches have been used to describe the stability of particles in biological and environmental media—including the critical coagulation concentration (CCC), the stability ratio (W), and the inverse stability ratio (α)—none of these approaches directly addresses the loss of unique nanoscale behavior, which, as defined by the NNI, represents a central criterion for defining a nanomaterial.²⁰ Unique optical behavior, particularly the presence of defined LSPR bands, is one of the characteristic nanoscale properties of MetNPs. The fact that these optical properties can be diminished upon interaction of MetNPs with electrolytes, and the subsequent formation and growth of nanoparticle clusters that accompanies such interactions, makes it be possible to develop a metric for quantifying and comparing the persistence of MetNPs in aqueous matrices. Comparing the ratio of absorbance at Abs_{LSPR1} to the growth of a second red-shifted LSPR band (Abs_{LSPR2}) may be a useful means for monitoring and comparing

the persistence of the unique nanoscale activity of MetNPs over time. As we demonstrate here, the $Ab_{\text{LS}_{\text{SPR}1}}:Ab_{\text{LS}_{\text{SPR}2}}$ ratio is likely to be a function of solution ionic composition (Figures 3-3 and 3-4), as well as a range of nanoparticle characteristics (Figures 3-5 and 3-6). Such relationships can provide utility in a number of applications ranging from the development of nano-pharmaceuticals to deriving water quality criteria for optically-active MetNPs discharged to aquatic systems.

The potentially enormous numbers of MetNP formulations possible makes full study of every material on a case-by-case basis intractable. Consequently, the determination of MetNP persistence by a rapid and accurate means may assist with streamlining environmental risk assessment efforts as well as screening of prospective MetNP-based therapeutic compounds by enabling predictions of risk and efficacy from low-cost, high-throughput UV-Vis screening techniques. This enables prioritization of the highest risk materials to send through more costly *in vitro* and *in vivo* studies early in the MetNP product discovery and development cycle.

3.5 Acknowledgments

We are grateful for funding from the US National Science Foundation (BES 0853989) and the Virginia Tech Institute for Critical Technology and Applied Science. This material is based upon work supported by the National Science Foundation (NSF) and the Environmental Protection Agency (EPA) under NSF Cooperative Agreement EF-0830093, Center for the Environmental Implications of NanoTechnology (CEINT). Any opinions, findings, conclusions or recommendations expressed in this material are those of the authors and do not necessarily

reflect the views of the NSF or the EPA. This work has not been subjected to EPA review and no official endorsement should be inferred.

3.6 References

1. Project on Emerging Nanotechnologies. Consumer products inventory of nanotechnology products. www.nanotechproject.org/inventories/consumer
2. Maynard, A. D., Nanotechnology: assessing the risks. *Nano Today* **2006**, 1 (2), 22-33.
3. Bowman, D.; Hodge, G., Nanotechnology: mapping the wild regulatory frontier. *Futures* **2006**, 38 (9), 1060-1073.
4. NNI, The National Nanotechnology Initiative-Supplement to the President's FY 2011 Budget. In National Nanotechnology Coordination Office: Washington, DC, USA, 2010.
5. DEFRA, UK Voluntary Reporting Scheme for engineered nanoscale materials. In Department of Environment Food and Rural Affairs: London, UK, 2008.
6. EPA, Notice: Nanoscale Materials Stewardship Program. In *Federal Register*, Environmental Protection Agency: Washington, DC, USA, 2008; Vol. 73, pp 4861-4866.
7. AP, Berkeley puts nanotechnology under hazardous materials law. *Los Angeles Times* 2006.
8. Paciotti, G.; Myer, L.; Weinrich, D.; Goia, D.; Pavel, N.; McLaughlin, R.; Tamarkin, L., Colloidal gold: a novel nanoparticle vector for tumor directed drug delivery. *Drug Delivery* **2004**, 11, 169-183.
9. Lee, H.; Yeo, S.; Jeong, S., Antibacterial effect of nanosized silver colloidal solution on textile fabrics. *Journal of Materials Science* **2003**, 38 (10), 2199-2204.
10. Prashant, J.; Pradeep, T., Potential of silver nanoparticle-coated polyurethane foam as an antibacterial water filter. *Biotechnology and Bioengineering* **2004**, 90 (1), 59-63.
11. Nehl, C.; Hafner, J., Shape-dependent plasmon resonance of gold nanoparticles. *Journal of Materials Chemistry* **2008**, 18, 2415-2419.
12. Mie, G., Beiträge zur optic trüber medien, speziell kolloidaler metallösungen. *Ann Phys* **1908**, 330, 377-445.
13. Diegoli, S.; Manciuola, A.; Begum, S.; Jones, I.; Lead, J.; Preece, J., Interaction between manufactured gold nanoparticles and naturally occurring organic macromolecules. *Science of the Total Environment* **2008**, 402, 51-61.

14. Kim, T.; Lee, C.-H.; Joo, S.-W.; Lee, K., Kinetics of gold nanoparticle aggregation: experiments and modeling. *Journal of Colloid and Interface Science* **2008**, 318, 238-243.
15. Derjaguin, B.; Landau, L., Theory of the stability of strongly charged lyophobic sols and of the adhesion of strongly charged particles in solutions of electrolytes. *Acta Physico Chemica URSS* **1941**, 14, 633.
16. Verwey, E.; Overbeek, J., *Theory of the stability of lyophobic colloids*. Elsevier: Amsterdam, 1948.
17. Fairbrother, A.; Wenstel, R.; Sappington, K.; Wood, W., Framework for metals risk assessment. *Ecotoxicology and Environmental Safety* **2007**, 68, 145-227.
18. Gouin, T., The precautionary principle and environmental persistence: prioritizing the decision-making process. *Environmental Science & Policy* **2010**, 13, 175-184.
19. Yamamoto, H.; Nakamura, Y.; Moriguchi, S.; Nakamura, Y.; Honda, Y.; Tamura, I.; Hirata, Y.; Hayashi, A.; Sekizawa, J., Persistence and partitioning of eight selected pharmaceuticals in the aquatic environment: laboratory photolysis, biodegradation, and sorption experiments. *Water Research* **2009**, 43, 351-362.
20. NSET, National Nanotechnology Initiative-The Initiative and its Implementation Plan. In *Nanoscale Science, E. a. T.*, Ed. National Science and Technology Council: Washington, DC, USA, 2000.
21. Kennedy, A.; Hull, M.; Bednar, A.; Goss, J.; Gunter, J.; Bouldin, J.; Vikesland, P.; Steevens, J., Fractionating nanosilver: importance for determining toxicity to aquatic test organisms. *Environmental Science & Technology* **2010**, 44 (24), 9571-9577.
22. Auffan, M.; Rose, J.; Bottero, J.; Lowry, G.; Jolivet, J.; Wiesner, M., Towards a definition of inorganic nanoparticles from an environmental health and safety perspective. *Nature Nanotechnology* **2009**, 4, 634-641.
23. Poda, A.; Bednar, A.; Kennedy, A.; Harmon, A.; Hull, M.; Mitrano, D.; Ranville, J.; Steevens, J., Characterization of silver nanoparticles using flow-field flow fractionation interfaced to inductively coupled plasma mass spectrometry. *Journal of Chromatography A* **In press**.
24. Liu, J.; Hurt, R. H., Ion release kinetics and particle persistence in aqueous nano-silver colloids. *Environmental Science & Technology* **2010**, 44, 2169-2175.
25. Alivisatos, P., The use of nanocrystals in biological detection. *Nature Biotechnology* **2004**, 22 (1), 47-52.
26. Pissuwan, D.; Valenzuela, S.; Cortie, M., Therapeutic possibilities of plasmonically heated gold nanoparticles. *Trends in Biotechnology* **2006**, 24 (2), 62-67.

27. Turkevich, J.; Stevenson, P. C.; Hillier, J. A., Study of the nucleation and growth processes in the synthesis of colloidal gold. *Discuss. Faraday Soc.* **1951**, 11, 55-59.
28. Li-Mei, A.; Feng, G.; Bi-Feng, P.; Da-Xiang, C.; Hong-Chen, G., Interaction between gold nanoparticles and bovine serum albumin or sheep antirabbit immunoglobulin G,. *Chinese Journal of Chemistry* **2006**, 24, 253-256.
29. Qian, X. M.; Peng, X. H.; Ansari, D. O.; Yin-Goen, Q.; Chen, G. Z.; Shin, D. M.; Yang, L.; Young, A. N.; Wang, M. D.; Nie, S. M., In vivo tumor targeting and spectroscopic detection with surface-enhanced Raman nanoparticle tags. *Nature Biotechnology* **2008**, 26 (1), 83-90.
30. Wuelfing, W. P.; Gross, S. M.; Miles, D. T.; Murray, R. W., Nanometer Gold Clusters Protected by Surface-Bound Monolayers of Thiolated Poly(ethylene glycol) Polymer Electrolyte. *Journal of the American Chemical Society* **1998**, 120 (48), 12696-12697.
31. He, T.; Wan, J.; Tokunaga, T., Kinetic stability of hematite nanoparticles: the effect of particle sizes. *Journal of Nanoparticle Research* **2008**, 10, 321-332.
32. Shannon, R., Revised effective ionic radii and systematic studies of interatomic distances in halides and chalcogenides. *Acta Cryst* **1976**, A32, 751-767.
33. Frens, G.; Overbeek, J., Repeptization and the theory of electrostatic colloids. *Colloid and Interface Science* **1972**, 38 (2), 376-387.
34. Laaksonen, T.; Ahonen, P.; Johans, C.; Kontturi, K., Stability and electrostatics of mercaptoundecanoic acid capped gold nanoparticles with varying counter-ion sizes. *ChemPhysChem* **2006**, 7 (10), 2143-2149.
35. Stankus, D.; Lohse, S.; Hutchison, J.; Nason, J., Interactions between natural organic matter and gold nanoparticles stabilized with different organic capping agents. *Environmental Science & Technology* **2010**, 45, 3238-3244.
36. MacCuspie, R., Colloidal stability of silver nanoparticles in biologically relevant conditions. *Journal of Nanoparticle Research* **2010**, 13 (7), 2893-2908.
37. MacCuspie, R.; Allen, A.; Hackley, V., Dispersion stabilization of silver nanoparticles in synthetic lung fluid studied under in situ conditions. *Nanotoxicology* **2010**, 5 (2), 140-156.
38. Williams, J.; Lansdown, R.; Sweitzer, R.; Romanowski, M.; LaBell, R.; Ramaswami, R.; Unger, E., Nanoparticle drug delivery system for intravenous delivery of topoisomerase inhibitors. *Journal of Controlled Release* **2003**, 91 (1-2), 167-172.

39. Yang, H.-W.; Hua, M.-Y.; Liu, H.-L.; Huang, C.-Y.; Tsai, R.-Y.; Lu, Y.-J.; Chen, J.-Y.; Tang, H.-J.; Hsien, H.-Y.; Chang, Y.-S.; Yen, T.-C.; Chen, P.-Y.; Wei, K.-C., Self-protecting core-shell magnetic nanoparticles for targeted, traceable, long half-life delivery of BCNU to gliomas. *Biomaterials* **2011**, In press.
40. Krasovskii, V.; Nagovitsyn, I.; Chudinova, G.; Savranskii, V.; Karavanskii, V., Interaction of gold nanoparticles with bovine serum albumin. *Bulletin of the Lebedev Physics Institute* **2007**, 34 (11), 321-324.

Chapter 4. Filter-feeding bivalves store and biodeposit colloiddally stable gold nanoparticles

Matthew S. Hull^{1,2,3}, Perrine Chaurand^{3,4}, Jerome Rose^{3,4}, Melanie Auffan^{3,4}, Jean-Yves Bottero^{3,4},
Jason C. Jones^{1,2}, Irvin R. Schultz⁵, and Peter J. Vikesland^{1,2,3*}

¹Virginia Tech Department of Civil and Environmental Engineering, Blacksburg, Virginia, USA

²Virginia Tech Institute for Critical Technology and Applied Science (ICTAS)

³Center for the Environmental Implications of Nanotechnology (CEINT)

⁴CEREGE, UMR 6635 CNRS/Aix-Marseille University, International Consortium for the Environmental Implications of Nanotechnology (iCEINT), Aix-en-Provence, France

⁵Pacific Northwest National Laboratory, Marine Sciences Laboratory, Sequim, Washington,
USA

4.1 Abstract

Nanoparticles resistant to salt-induced aggregation are continually being developed for biomedical and industrial applications. Because of their colloidal stability these functionalized nanoparticles are anticipated to be persistent aquatic contaminants. Here, we show that *Corbicula fluminea*, a globally distributed clam that is a known sentinel of aquatic ecosystem contamination, can uptake and biodeposit bovine serum albumin (BSA) stabilized gold nanoparticles. Nanoparticle clearance rates from suspension were dictated by diameter and concentration, with the largest particles cleared most quickly on a mass basis. Particle capture facilitates size-selective ‘biopurification’ of particle suspensions with nanoscale resolution.

Nanoparticles were retained either within the clam digestive tract or excreted in feces. Our results suggest that biotransformation and biodeposition will play a significant role in the fate and transport of persistent nanoparticles in aquatic systems.

4.2 Introduction

Gold nanoparticles (AuNP) are expected to be key nanoscale components in twenty-first century applications ranging from biosensors to catalysis due to their unique optical properties, chemical stability, and their capacity to exhibit a multiplicity of shapes, particle sizes, and surface chemistries.¹ Because of their increased use and chemical inertness, gold nanoparticles have potential to become a significant persistent nanomaterial input to environmental systems. To facilitate gold nanoparticle incorporation into devices and applications it is generally necessary to functionalize the nanoparticle surface with DNA, peptides, proteins, or polymers.²⁻⁴ Serum albumin proteins such as bovine serum albumin (BSA), which are abundant in mammalian plasma, have attracted particular interest as stabilizers given their frequent use in the development and study of emerging bionanomaterials,⁵ their ability to stabilize nanoparticles for cellular targeting,⁶ and the propensity for nanoparticles to associate with proteins both within cells⁷ and in environmental media.⁸ Although the extent to which the use of BSA, specifically, will be adopted by industry remains unknown, the use of BSA as a surrogate protein for the preparation of biological macromolecule-nanoparticle conjugates is well established.

Given what we currently know about the persistence and toxicity of pharmaceutical compounds in the environment, the safe use and disposal of nanoscale particles, particularly certain types of nanomedicines functionalized for stability in highly saline media such as blood,⁹
¹⁰ inherently requires efforts to understand how primary particle size and surface

functionalization alter nanoparticle uptake and fate in biological and environmental systems. The objective of the present work was to investigate the size-dependent uptake, fate, and biotransformation of BSA-coated gold nanoparticles by the filter-feeding bivalve *Corbicula fluminea*. Freshwater and marine bivalves are commonly employed as biological sentinels¹¹ for the detection and monitoring of a broad spectrum of environmental contaminants such as metals,¹² biocides,¹³ asbestos fibers,¹⁴ bacteria,¹⁵ and protozoan parasites.^{16, 17} Recently, researchers have demonstrated that biofilms and clams were the primary biological compartment for surfactant-stabilized gold nanorods added to estuarine mesocosms,¹⁸ and that 10 nm amine-functionalized gold nanoparticles penetrated the gills and digestive epithelia of *C. fluminea*.¹⁹ The present work goes further in demonstrating the role of particle size on the rate of particle clearance from suspension and the importance of biodeposition to cross-media transference of colloidal particles.

4.3 Experimental

Preparation of gold nanoparticle suspensions. Bovine serum albumin-coated gold nanoparticles (BSA-AuNP) were prepared by incubating citrate-stabilized gold nanoparticles (citrate-AuNP) with 0.1 mg BSA·mL⁻¹ using established protocols.²⁰ Citrate-AuNP of 7.8 and 15 nm diameter were prepared as described by Jana et al²¹ and by Turkevich, respectively.²² The seed-mediated process of Frens²³ was used to prepare 46 nm citrate-AuNP. Each suspension incorporated citrate as a reducing agent (or co-reducing agent) and surface stabilizer, as citrate is known to play an important role in determining the size and monodispersivity of gold nanoparticles by regulating the pH of the reaction.²⁴ All suspensions were sterile-filtered (0.2 μm), and stored in an amber glass vial at 4 °C until use.

Characterization. Gold nanoparticle suspensions were characterized by UV-Vis spectroscopy, transmission electron microscopy (TEM), and dynamic light scattering (DLS). Primary particle size and morphology were characterized using a Zeiss 10CA Transmission Electron Microscope (60 kV) equipped with a high resolution (1024 × 1024 pixel format) MT Advantage GR/HR-B CCD Camera System (Advanced Microscopy Techniques Corporation). For sample preparation, 10-20 µL of citrate- or BSA-AuNP suspension were pipetted onto a carbon-coated copper TEM grid (Electron Microscopy Sciences) and dried at room temperature. Electron micrographs were digitized and analyzed using ImagePro (MediaCybernetics, Bethesda, MD) to assess the heterogeneity of the nanoparticle suspensions and to calculate average primary particle diameters. An FEI Titan 300 operating at 200 kV was used to acquire high-resolution TEM, as well as scanning tunneling electron microscopy (STEM) images. Characterization results for gold nanoparticle suspensions are provided in the Supporting Information (Table S1).

Nanoparticle clearance assays with *C. fluminea*. Adult Asian clams (*Corbicula fluminea* [Müller]) were collected from the New River near Radford, VA, and acclimated to laboratory conditions for 14 d prior to testing. *C. fluminea* nanoparticle clearance assays were performed in moderately hard, synthetic (MHS) freshwater. For studies investigating the size-dependent clearance of BSA-AuNP by *C. fluminea*, as well as the localization of BSA-AuNP within *C. fluminea* organ systems, exposures were performed in 10 L polypropylene aquariums filled with 2 L of BSA-stabilized gold nanoparticle suspension prepared in EPA MHS at a concentration of 2 mg L⁻¹ as Au (BSA-AuNP were stable in EPA MHS throughout the exposure period as determined by UV-Vis measurements of control samples). At 2 mg L⁻¹, the concentrations of BSA-AuNP investigated in the current study exceed nanoparticle concentrations likely to occur in real-world environmental systems. The elevated concentration, however, was necessary to

monitor colloidal stability of the BSA-AuNP suspension by UV-Vis spectroscopy analysis of the surface Plasmon resonance band (SPR) throughout the duration of the assay. The authors considered the ability to monitor long-term colloidal stability to be of key importance during the current study, and thus exposures at concentrations in excess of environmentally relevant concentrations were used. To each aquarium, 75 *C. fluminea* of 1-2 years of age, 15 ± 0.6 mm in length (umbo to ventral margin), and 2.0 ± 0.3 g whole body wet weight were added at t_0 hours. Aquariums were continuously aerated using a borosilicate pipette. To investigate the effects of initial (t_0) Au concentration (2, 4, or 8 mg L⁻¹ as Au) on BSA-AuNP clearance, additional assays were performed in replicate 50 mL glass beakers ($n = 5$), each of which contained 40 mL of test suspension. Individual *C. fluminea* test organisms were added to each beaker. All exposures were performed at 20 ± 1 °C. To reduce system complexity, feeding was withheld during all particle clearance assays.

Optical absorbance and water column gold concentration were monitored by UV-Vis and ICP-MS, respectively. At each of the following time-points, a 1 mL water column sample was taken: 0 (control, prior to addition of organisms to test suspension), 12, 36, 60, 84, 108, and 180 h. After 180 h, *C. fluminea* were removed from the BSA-AuNP exposure, rinsed with ultrapure water and transferred to 10 L polyethylene aquariums containing 2 L of EPA MHS diluent only (i.e., no BSA-AuNP were present in the depuration tanks). After the transfer to fresh diluent, sampling resumed and one mL water samples were removed at each of the following time points: 204, 228, 252, and 348 hours after the experiment began. For each one mL sample removed from the aquarium, absorbance from 300-800 nm was measured. The same sample was then transferred to a sterile polystyrene tube, acidified with 200 μ L aqua regia (1:3, Trace metal grade HNO₃:HCl) and brought to a final volume of 10 mL with ultrapure water. Samples then were

analyzed for gold content by ICP-MS per Standard Method 3125-B.²⁵ Samples and calibration standards were prepared in a matrix of 2% aqua regia, which was more effective at dissolving the AuNP than either HNO₃ or HCl alone.

Micro X-ray Fluorescence Spectroscopy (μ -XRF). At each sampling point described previously for the water column samples, three *C. fluminea* were removed from each aquarium, euthanized, and prepared for μ -XRF measurements. To facilitate shell opening, interior and posterior ligaments of *C. fluminea* were severed using a surgical scalpel. Next, the interior soft tissue was dissected intact from each half-shell and rinsed three times with deionized water. The soft tissue was then placed whole into a labeled plastic tissue cassette with foam absorbent pad. The tissue samples were prepared for μ -XRF analysis using a procedure described by Laforsch and Tolldrian²⁶ for μ -XRF analysis of *Daphnia magna*. Briefly, the samples were dried in a graded series of acetone solutions (70 to 100%) before being transferred to a solution of 1,1,1,3,3,3 hexamethyldisilazane (HMDS). After 30 minutes in HMDS, tissue samples were transferred to a vacuum desiccator and dried overnight.

All μ -XRF measurements were carried out at the lab-scale on a microscope (XGT⁷⁰⁰⁰, Horiba Jobin Yvon) equipped with an X-ray guide tube producing a finely focused and high-intensity beam with a 100 μ m spot size (Rh X-ray tube, accelerating voltage of 50 kV, current of 1 mA). X-ray emission from the irradiated sample is detected via an energy-dispersive X-ray (EDX) spectrometer equipped with a liquid-nitrogen-cooled high purity Si detector. Elemental maps and microanalyses were performed on HMDS-prepared whole-animal samples at atmospheric pressure. Images were obtained from the intensity of the Au L α 1 emission line. The selected region of interest (ROI) of this line was reduced in energy because of the partial overlap of the Zn K β line with the Au L α 1 line. Moreover the background contribution was removed.

The average XRF spectrum for each whole organism was generated from hyperspectral mapping (i.e. a full XRF spectrum recorded at each and every pixel of the element image) and converted to semi-quantitative results (relative mass percent) using the fundamental parameters approach (FPA).

For enhanced sensitivity and spatial resolution ($3\ \mu\text{m} \times 3\ \mu\text{m}$), μ -XRF measurements were also performed on LUCIA beamline at the SOLEIL synchrotron (Paris, France) under vacuum, with a Si(111) monochromator and a silicon drift detector.²⁷ Due to the high intensity of the P (K) phosphorus signal compared to the Au M₃-edge (2 743 eV), the Au map is presented as the ratio of the normalized Au map over the normalized P map.

Following μ -XRF measurements, Au body burdens were determined by ICP-MS of digestates prepared by nitric acid microwave digestion of the tissue amalgamated from 3 clams removed at each exposure time-point (CEM MARS method #375). To ensure the complete solubilization of AuNP, 200 μL aqua regia was mixed with tissue digestates prior to analysis by ICP-MS as described previously for water column samples. Body burdens for Au were expressed as the mass of Au (mg) per mass of wet tissue (kg).

Characterization of clam feces. Upon termination of the exposures, visible feces were harvested from each aquarium by pipette and transferred to glass scintillation vials. Up to 5 mg of each fecal sample then was transferred to an ultrathin carbon film/holey carbon 400 mesh copper TEM grid and dried overnight at room temperature. Samples were imaged by TEM, HRTEM, and STEM.

4.4 Results and Discussion

Suspensions of three different sizes of BSA-stabilized gold nanoparticles (BSA-AuNP; Figure 4-1a-c) were added at a mass-normalized concentration of 2 mg L^{-1} (as Au) to aquariums containing seventy-five *C. fluminea* test organisms. After 180 h, *C. fluminea* filtered and removed from suspension BSA-AuNP of 7.8, 15, and 46 nm diameter (Figure 4-1d-e). Clearance of BSA-AuNP from the water column was quantified by daily monitoring of the total gold concentration by ICP-MS and the optical absorbance at the surface plasmon resonance band (Abs_{SPR}) by UV-Vis spectroscopy. Over the 180-h exposure period, both [Au] and the SPR band (Supporting Information Figure 4-S1) steadily decrease for samples from aquariums containing *C. fluminea*, but remain stable in the absence of test organisms (Figure 4-1d). Integrating these two measurement techniques provides a means to precisely determine concentration (in terms of total gold as measured by ICP-MS), while simultaneously providing evidence that the gold is present in nanoparticulate form (as indicated by a distinct SPR band between 500-550 nm that is absent for ionic gold; Supporting Information Figure 4-S2). The location, intensity, and width of the SPR band are indicative of particle size, shape, concentration, and sample heterogeneity.²⁸ The initial SPR band location is a function of particle size, with the smallest particles exhibiting a hypsochromic (blue) shift of the SPR band relative to larger particles. For each particle suspension, the change in Abs_{SPR} correlates with ICP-MS measurements of the total gold concentration indicating that the gold exists primarily as discrete nanoscale particles. This result is consistent with the findings of others who have reported that Abs_{SPR} can be used to quantify the concentration as well as the size of metallic nanoparticles in suspension.²⁸

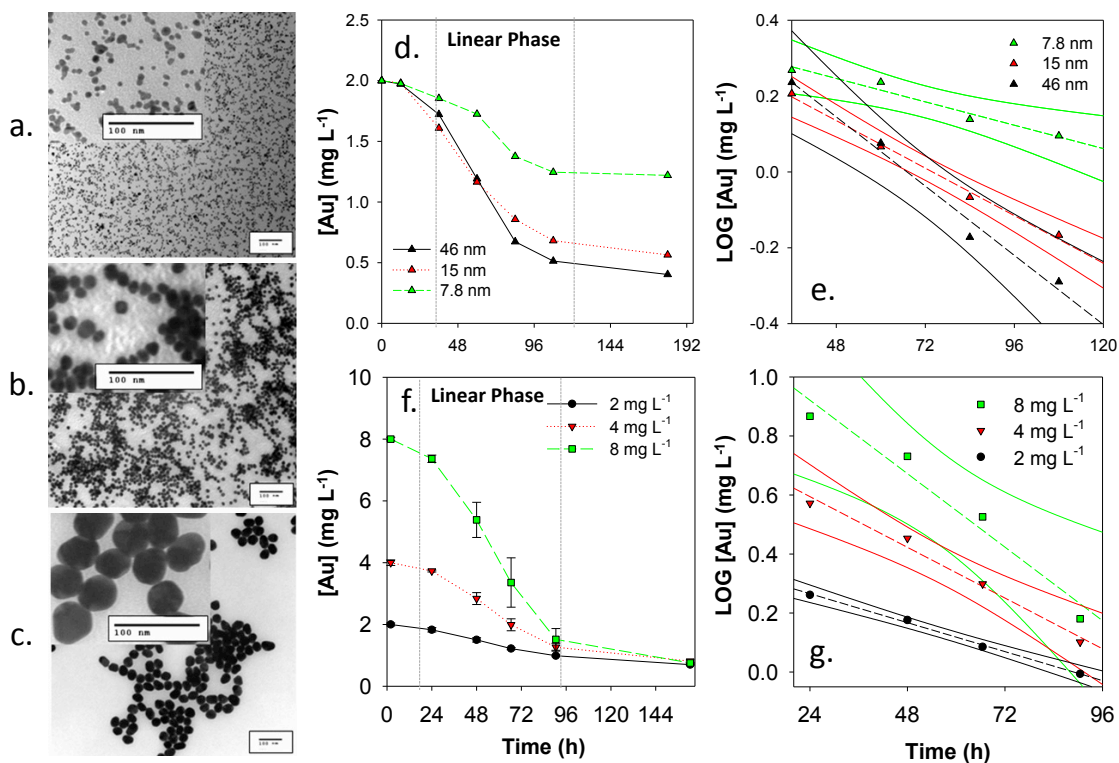


Figure 4-1. (a-c) TEM images of 7.8, 15, and 46 nm AuNP—in each panel, scale bars denote 100 nm; insets show particles at increased magnification. (d) Plot showing the average water column concentration of 7.8, 15, and 46 nm BSA-AuNP expressed in terms of Au mass concentration (mg L^{-1}) from 0 to 180 h (solid lines denote the average water column [Au] in negative controls—no clams present—as determined from Abs_{SPR}), and (e) corresponding plot of the log-transformed data (and 95% confidence intervals) for the linear clearance phase (from 48 to 120 h). (f) Plot of the average water column concentration of 46 nm BSA-AuNP as a function of [Au] at t_0 and time exposed to *C. fluminea*; and (g) plot of the linear phase of BSA-AuNP clearance (and 95% confidence intervals). Fitting of these data was used to determine first-order rate constants for clearance of BSA-AuNP as a function of primary particle size and [Au] concentration at t_0 .

The absence of a measurable red-shift or significant broadening of the SPR peak between 600-800 nm during the exposure indicates that particle removal from suspension was not the result of particle aggregation and settling (Supporting Information Figure 4-S3).^{29, 30} This absence provides clear evidence that *C. fluminea* removes discrete, BSA-stabilized nanoparticles from suspension through filtration. It is important to differentiate between these processes since, as noted by others,³¹ many studies of nanoparticle uptake and toxicity fail to account for

aggregation processes that result in the removal of particles from suspension due to settling and not organismal uptake.

Clearance of each size particle follows a logarithmic pattern: a lag-phase during the first 12 h of exposure, a linear clearance phase between 12 and 108 h, and a leveling off between 108 and 180 h (Figure 4-1d). Other researchers have shown that the filtration rates of disturbed bivalves are reduced more than four-fold relative to undisturbed animals,³² thus suggesting that the initial lag-phase is attributable to the acclimation period required for the clams to begin filtering following transfer to the assay chamber. The linear clearance phase is representative of a period during which the clams have acclimated to the assay environment and begun actively filtering. The leveling off observed may be the result of a combination of factors including decreasing particle concentration, gill clogging,³² compaction of the digestive tract,³³ or physiological adjustment of filtering³⁴ and ingestion rates.³⁵ We cannot presently exclude the possibility that *C. fluminea* is initially stimulated by free or surface adhered BSA protein or that the clams preferentially deplete the BSA protein fraction and then decrease filtration activity once the ratio of BSA to AuNP is reduced below some threshold. A similar phenomenon has been reported by researchers who observed stimulated feeding behavior for *Sphaerium* and *Dreissena* bivalves exposed to high concentrations of inorganic graphite particles of 0.5 to 1.5 μm diameter;³⁶ in these experiments, measured filtration rates were initially very low, but increased upon addition of the algal cells on which these bivalve genera commonly feed. The increase in feeding rates could be attributable to either a) facilitated uptake of graphite particles sorbed to algal cells or b) the availability of a preferred food source—in this case, algal cells. Additional studies to test the hypothesis that the presence of proteins and other biological macromolecules may stimulate

uptake of BSA-AuNP are required to truly address this question. Such studies were outside the scope of the present investigation.

Clearance of BSA-AuNP during the linear-uptake phase ($12 \leq t \leq 180$ h) followed first-order kinetics and rate constants determined for the 7.8, 15, and 46 nm nanoparticles were 0.0026, 0.0052, and 0.0076 h^{-1} , respectively (Figure 4-1e). Plotting the particle clearance rate constant versus the primary particle diameter shows that the rate increases logarithmically with particle diameter (Supporting Information Figure 4-S4). Although descriptive across the range of particle sizes studied here, this general pattern of clearance as a function of particle size does not extend to larger micron-sized particles, which can be cleared from suspension with 100% efficiency in less than one hour.³⁷ This result is not surprising, since the mechanisms used to capture particles varying so greatly in size differ due to particle fluid dynamics, composition, density, and geometry.³⁸

Particle removal efficiencies,³⁷ calculated based on the change in the Au mass concentration between t_0 and t_{180} indicate that 7.8, 15, and 46 nm BSA-AuNP were removed from suspension with 39, 72, and 80% efficiency, respectively. Others have demonstrated this positive correlation between the retention efficiency and the particle size with diameters as low as 2 μm .³⁷ Our results show that this correlation remains even at the sub-micron scale with particles differing in diameter by less than 30 nm. However, our assays with nanoscale particles require clearance periods of up to 180 h, whereas the retention efficiencies of larger micron-sized particles are typically determined in assays of less than an hour duration to minimize the confounding effects of gravitational settling.³⁷ Given the colloidal stability of BSA-AuNP in the absence of the clams (Figure 4-1d), gravitational settling was not a concern here.

Uptake experiments performed with 46 nm BSA-AuNP at differing initial (t_0) concentrations of 2, 4, and 8 mg L⁻¹ indicate that particle concentration also influences the rate of nanoparticle clearance from suspension (Figure 4-1f-g). A logarithmic clearance pattern was again evident for each initial concentration, with a lag-phase of 24 h preceding a linear decrease in the water column concentration for the next 65-70 h, and then a leveling off over the final 70 h of the assay. Nanoparticle clearance during the linear-phase followed first-order kinetics and as expected for a first-order process there is a positive relationship between the initial concentration of BSA-AuNP and the clearance rate (Figure 4-1g). Previous research using micron-sized particles has shown a similar positive relationship between particle concentration and filtration rate as *Corbicula* are thought to physiologically adjust filtration rates to achieve an optimal rate of particle clearance.³⁴ Our data suggest that this relationship extends to particles well into the nano-domain.

Size-selective sorting of nanoscale particles by clams. The size-selective clearance of BSA-AuNP observed for *C. fluminea* introduces the possibility of using bivalves or other suspension feeders to sort nanoscale particles by size with nanometer resolution. To test this hypothesis, a size-selective uptake experiment was performed using three sizes of BSA-AuNP added to 50 mL assay chambers both separately and in a combined ‘cocktail’. All particle concentrations were mass normalized to give a final in-chamber gold concentration of 15 mg L⁻¹; for the cocktail this required adding each of the three suspensions at concentrations of 5 mg L⁻¹. A relatively high concentration was necessary to facilitate monitoring of the location and height of the SPR band by UV-Vis spectroscopy. Suspensions could not be normalized by particle number or surface area since the mass concentrations required to achieve this for the smallest particle suspensions were below instrument detection limits.

Despite the increased t_0 concentration, BSA-AuNP of all three sizes were readily cleared from suspension by *C. fluminea* (Supporting Information Figure 4-S5). Although the same positive relationship between clearance rate and particle diameter that was observed in the large-scale aquarium exposures was evident once again, quantitative comparisons among the rate constants obtained from these two experiments are not possible due to differences in Au concentration, water volume, and number of test organisms. After 120 h the mean SPR band for the cocktail to which clams were added blue-shifted ≈ 4 nm, suggesting a decrease in the average particle diameter (Supporting Information Figure 4-S6a). The difference between the location of the SPR band of the cocktail in the presence and absence of the clams was greatest after 72 h (Supporting Information Figure 4-S6a), suggesting that a practical application of filter-feeding organisms to size-purify nanoparticles would require an exposure duration that achieves maximum size-reduction without allowing excreted metabolites to reach levels that might induce particle aggregation through alteration of solution ionic strength or pH.

Based on the clearance rates of the individual particle suspensions, after 120 h filtering by *C. fluminea*, the relative percent composition (by mass) of the cocktail changed from being divided evenly at one-third for each particle size to being more than one-half 7.8 nm particles (Supporting Information Figure 4-S6b). The optical absorbance of the largest particles, 46 nm, was reduced to below the detection limits of the UV-Vis after 96 h, suggesting that these particles likely comprised less than 10% of the cocktail upon termination of the experiment. It is worth noting that the SPR shift of ~ 4 nm could be replicated experimentally by preparing cocktails corresponding to the measured gold concentrations and predicted particle size distributions at t_0 and t_{120} during the size-selective uptake assay (Supporting Information Figure 4-S7).

Although not previously reported for nanoscale particles, investigators have noted that bivalves filter or retain small particles less efficiently than larger particles, and thus the fraction of these “inefficiently retained” particles can increase over time.³² Other researchers have suggested that small particles, typically < 3 μm in diameter, exhibit ‘negative retention’ in studies of particle retention by bivalves.^{37,39,40} A conspicuous lack of particle characterization in conjunction with these uptake studies, however, has limited the ability of investigators to draw definitive conclusions as to the source and composition of these particles. At least one researcher concluded that small particles were produced by bivalve test organisms,³⁷ whereas more recently, others have concluded that such particles do not necessarily originate from the study organisms.⁴¹ Our results suggest that on a mass basis, the efficiency with which filter-feeding bivalves clear particles from the water column decreases with a decrease in particle diameter, even in the nanometer domain, and this may facilitate the biologically-mediated separation of particles differing in size by only tens of nanometers. Clearance rates for particles of 7.8 and 15 nm diameter, while generally indistinguishable from one another, could be differentiated from the largest diameter particles (46 nm). In theory, such biologically-mediated size-selection of colloidal particles could be applied as a potentially low-cost, passive, and continuous alternative to conventional size purification techniques such as differential centrifugation or tangential flow filtration. Additional studies are required, however, to realize any practical application of this concept, as a number of factors ranging from the condition of the filtering organisms to the presence of stabilizers or preservatives that may co-occur with commercial nanomaterials will likely influence actual filtration rates.

Fate and biotransformation of nanoparticles in bivalves. Analysis of whole-organism, soft-tissue preparations (shells removed) by X-ray fluorescence microscopy ($\mu\text{-XRF}$) indicated that

gold was confined to the digestive gland and regions of the digestive tract of BSA-AuNP-exposed *C. fluminea* with little indication of migration to other organ systems (Figure 4-2a,b). Because μ -XRF does not discriminate between surface-associated versus internalized analytes, analyses of organism cross sections were performed, and verified that gold was internalized and not simply sorbed to the external surfaces of the organisms (Supporting Information Figure 4-S8a). These cross-sections were also analyzed using the synchrotron-based XRF microscope LUCIA with a beam size of $3\ \mu\text{m} \times 3\ \mu\text{m}$. With this improved sensitivity and spatial resolution, we observed spots of gold that are diffusely distributed throughout the digestive gland. The larger clusters are about $15 \times 30\ \mu\text{m}$, and most of them are below 3 to 6 μm (Supporting Information Figure 4-S8b). We note that μ -XRF cannot differentiate between nanoparticulate gold or soluble gold; however, because nanoparticulate gold was observed in collected feces (*vide infra*) we expect that the gold signal from the digestive system is primarily due to nanoparticulate gold.

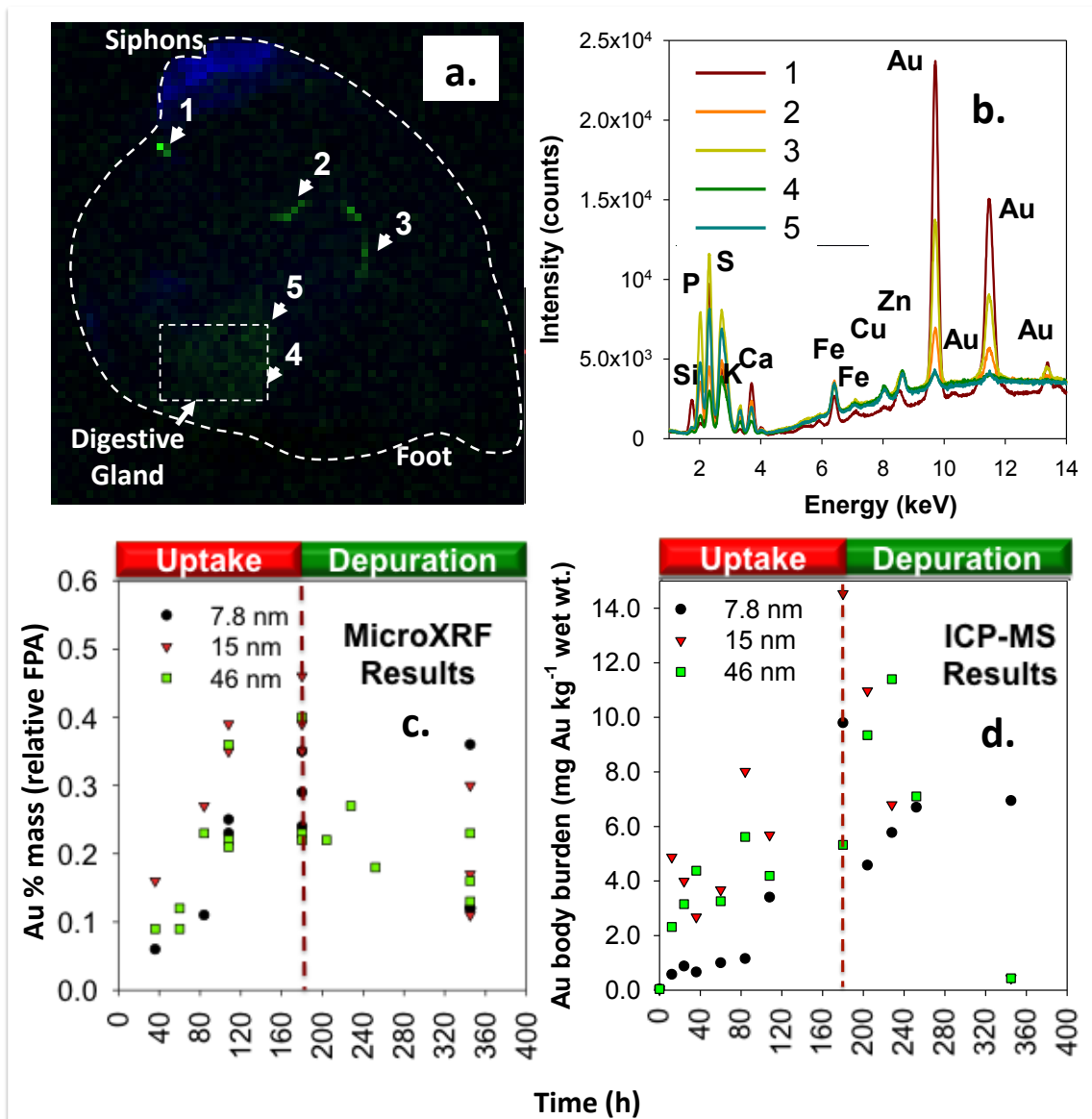


Figure 4-2. (a) A μ -XRF image of an HMDS-fixed *C. fluminea* specimen exposed to 46 nm BSA-AuNP for 180 h. Siphons, which were rich with Fe, are colored blue; Au-rich regions in the intestine and at the anus are colored green. The body of the organism is encircled by a dashed line and the locations of the siphons and foot are noted; a dashed rectangle surrounds the digestive gland—additional analysis of the digestive gland and organism cross-sections are provided in the Supporting Information (Figure 4-S8). (b) Semi-quantitative data of the elemental composition of samples were collected by μ -XRF spot-analysis of the *C. fluminea* specimen shown in panel (a), with numbers 1-5 corresponding to the Au-rich locations noted on the μ -XRF image. Plots showing (c) the relative Au composition (%) of HMDS-fixed *C. fluminea* as determined by μ -XRF and (d) Au body burden (mg Au kg⁻¹ wet tissue weight) as determined by ICP-MS of acid-digested tissue as a function of time (0 to 345 h) and primary particle size of BSA-AuNP—7.8, 15, and 46 nm. The vertical dashed lines at 180 h (panels c and d) indicate the point at which *C. fluminea* were rinsed and transferred from the BSA-AuNP test suspensions to fresh EPA MHS water and allowed to depurate their gut contents.

The gold content of whole *C. fluminea* was evaluated using a combination of μ -XRF and the fundamental parameters approach (FPA).⁴² The obtained percent mass as Au correspond to semi-quantitative and relative values, and are plotted as a function of time (Figure 4-2c). These results show that exposed clams contained gold, particularly in the digestive gland and at regions along the digestive tract (Figure 4-2a,b), and that the relative mass concentration of gold increased as a function of time for each particle size until the clams were removed from the BSA-AuNP exposure after 180 h and transferred to clean water (Figure 4-2c). For each particle size, the rate of increase in the relative mass concentration of gold measured in *C. fluminea* tissue was most rapid over the first 108 h of the exposure, which corresponds with the period of most rapid particle clearance from suspension. At each measured time-point during the accumulation phase, the relative mass concentration of gold present in the clams exposed to 15 nm BSA-AuNP was consistently greater than for the other two particle sizes, but this relationship was not statistically significant. In contrast to the μ -XRF results, but in strong support of the suspension chemistry results showing reduced clearance rates for the smallest particles (Figure 4-1d,e), ICP-MS analysis of tissue digestates show that the mass of Au internalized by *C. fluminea* via filtering of 7.8 nm BSA-AuNP was dramatically reduced relative to that of the 15 and 46 nm particles (Figure 4-2d). Discrepancies in μ -XRF and ICP-MS measures of Au were expected, however, since μ -XRF of whole-organism samples is sensitive to variations in three-dimensional sample geometry and subsequent fluctuations in X-ray penetration and fluorescence, whereas ICP-MS is not subjected to these same influences.

Following the transfer of clams to clean water, tissue gold concentrations determined by μ -XRF decreased, but even after 165 h, did not return to pre-exposure levels (Figure 4-2c). Tissue Au concentrations measured by ICP-MS, however, indicated a return to near-background levels

for 15 and 46 nm BSA-AuNP, whereas Au levels remained elevated for clams exposed to the 7.8 nm particles (Figure 4-2d). As suggested by others who recently compared the uptake of aggregated versus disaggregated nanoparticles by *Mytilus edulis* and *Crassostrea virginica*,⁴³ extended retention times in the gut (e.g., >72 h) may be indicative of particles undergoing extracellular digestion processes, and our results support this contention.

Semi-quantitative μ -XRF data suggest that clams partially accumulate and retain gold in the digestive tract and gland, but provide only limited information about the form that gold nanoparticles take during digestion. If *C. fluminea* are capable of digesting gold nanoparticles, then changes in particle size, shape, or aggregation state should be expected. Examination of fecal material by Scanning Tunneling Electron Microscopy (STEM) and High-Resolution Transmission Electron Microscopy (HRTEM) coupled with Energy Dispersive X-Ray Spectroscopy (EDX) indicate that particles can be recovered from *C. fluminea* feces in a variety of forms, including nanoscale aggregates and individual particles (Figure 3a-e), and that feces are comprised of a mixture of electron-dense metals including Au (Figure 4-3f). For the 46 nm BSA-AuNP, nanoparticles recovered in feces appeared much less spherical and uniform in size than prior to the exposure (Figure 4-3a), suggesting that some dissolution or mechanical alteration of the particles had occurred as a result of digestion and excretion. Conversely, 15 nm BSA-AuNP were recovered in fecal materials in dense clusters of particles (Figure 4-3d), but retained their spherical shape and uniform size (Figure 4-3e). These results confirm that filter-feeding bivalves likely will play an important role in transforming and transferring nanoscale particles suspended in the water column to the subsurface via biodeposition. Biodeposition, or the process of filtering, compacting, and depositing suspended particulate matter at the sediment-water interface, is an important ecological function performed by both freshwater and marine

bivalves as well as many other suspension feeders, and in some aquatic systems, the magnitude of this process can exceed tens of thousands of metric tons of biodeposited material annually.⁴⁴

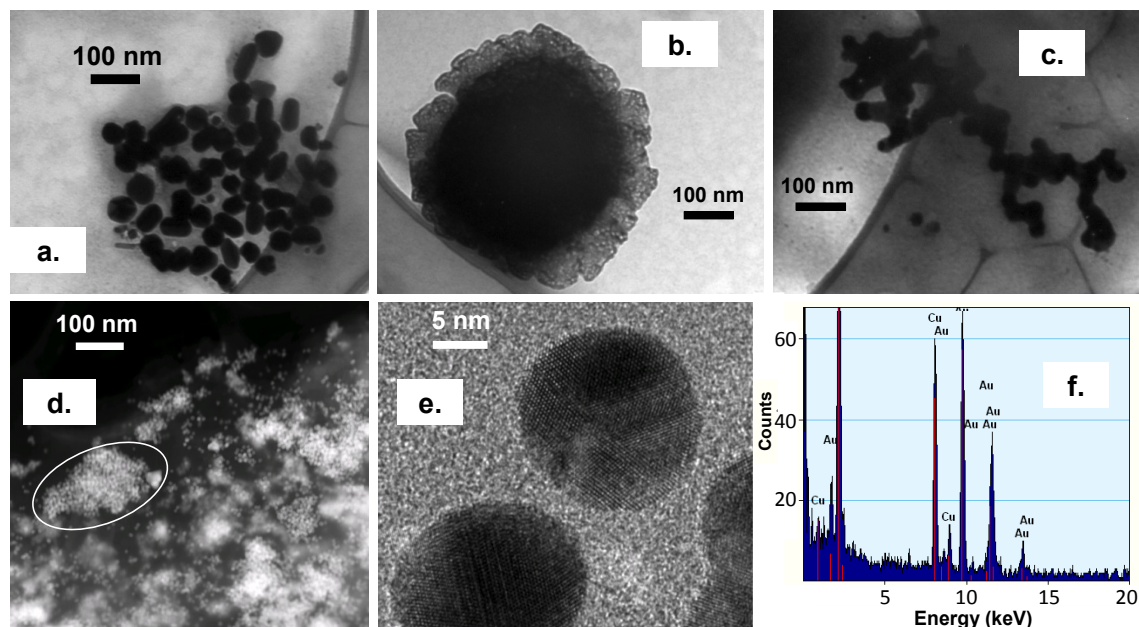


Figure 4-3. TEM images showing structures recovered from feces egested by *C. fluminea* following exposure to BSA-AuNP at 2 mg L⁻¹ as [Au]: (a) cluster of AuNP that are less spherical and less uniform in size than the 46 nm BSA-AuNP that were originally dosed to clams; (b, c) two different types of aggregate structures recovered from the same fecal sample; (d) STEM image of low electron-density fecal material containing clusters of 15 nm AuNP (white circle added to indicate one cluster); (e) Hi-Res TEM and (f) EDX indicating that particles recovered from feces of clams exposed to 15 nm BSA-AuNP at 2 mg L⁻¹ are spherical, crystalline, uniform in size, and comprised primarily of Au.

4.5 Acknowledgments

We are grateful for funding from the US National Science Foundation (BES 0853989) and the Virginia Tech Institute for Critical Technology and Applied Science. This material is based upon work supported by the National Science Foundation (NSF) and the Environmental Protection Agency (EPA) under NSF Cooperative Agreement EF-0830093, Center for the Environmental Implications of NanoTechnology (CEINT). Any opinions, findings, conclusions or recommendations expressed in this material are those of the authors and do not necessarily reflect the views of the NSF or the EPA. This work has not been subjected to EPA review and no

official endorsement should be inferred. W. Miles, R. Davis, R. Elston, M. Muryama, and K. Lowe provided invaluable assistance with sample characterization. We are grateful to the SOLEIL synchrotron (Paris, France) for the provision of beam time and acknowledge LUCIA staff (Nicolas Trcera, Anne-Marie Flank) for their technical support during data collection.

4.6 Supporting Information

Characterization

Analysis of TEM images indicated that mean primary particle diameters were 7.8 ± 3.3 , 15 ± 6.8 , and 46 ± 5.3 nm (Table 4-S1). Corresponding hydrodynamic diameters (Z_{ave} , nm) measured by dynamic light scattering (DLS) were 12.9 ± 0.4 , 31.9 ± 0.3 , and 44.1 ± 0.1 nm, respectively. Polydispersity indices ranged from 0.230 to 0.289, suggesting that suspensions were similarly monodisperse. Particle diameters predicted from the position of the surface plasmon resonance (SPR) band¹ were 4.2, 11.4, and 38.4 nm, which is in general agreement with the diameters measured by TEM and DLS. All particles were negatively charged at the pH of the assay (pH = 7.8) with electrophoretic mobilities of -1.47 ± 0.25 , -2.05 ± 0.13 , and -1.71 ± 0.01 $\mu\text{m}\cdot\text{cm}(\text{V}\cdot\text{s})^{-1}$ for the 7.8, 15, and 46 nm BSA-AuNP, respectively. Accurate zeta potential values could not be calculated for these particles due to the soft BSA coating,^{2,3} nonetheless, these electrophoretic mobilities support the contention that the particles were negatively charged under the assay conditions.

Consideration of Dosimetry: Mass, Particle Number, and Surface Area

On a mass basis, approximately 70-80% of the 15 and 46 nm BSA-AuNP were removed from suspension after 180 h, compared to less than 40% of the 7.8 nm BSA-AuNP. In terms of

particle number concentration, however, the number of 7.8 nm BSA-AuNP removed from suspension exceeded the number of 15 and 46 nm particles by 1.0×10^{14} and 1.5×10^{14} particles- mL^{-1} , respectively. When the concentrations are expressed in terms of the total surface area of particles removed, cumulative clearance of 7.8 and 15 nm BSA-AuNP were similar at approximately $3.0 \times 10^7 \text{ m}^2\text{-mL}^{-1}$, which was nearly three-fold greater than the total surface area concentration of the 46 nm BSA-AuNP removed.

Experimental Replication of Size-selective Biopurification of BSA-AuNP

It is worth noting that the SPR shift of ~ 4 nm could be replicated experimentally by preparing cocktails corresponding to the measured gold concentrations and predicted particle size distributions at t_0 and t_{120} during the size-selective uptake assay (Supporting Information Figure 4-S7).

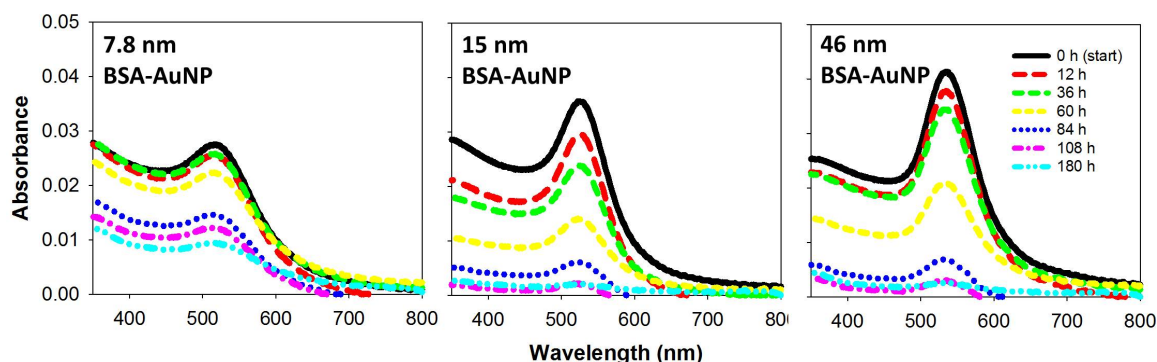


Figure 4-S1. Plots of UV-Vis spectra showing the time-dependent (0 to 180 h) decrease in absorbance intensity at Abs_{SPR} for 7.8 nm, 15 nm, and 46 nm BSA-AuNP suspensions in the presence of *C. fluminea*. Initial concentrations of BSA-AuNP were mass normalized to 2 mg L^{-1} as [Au].

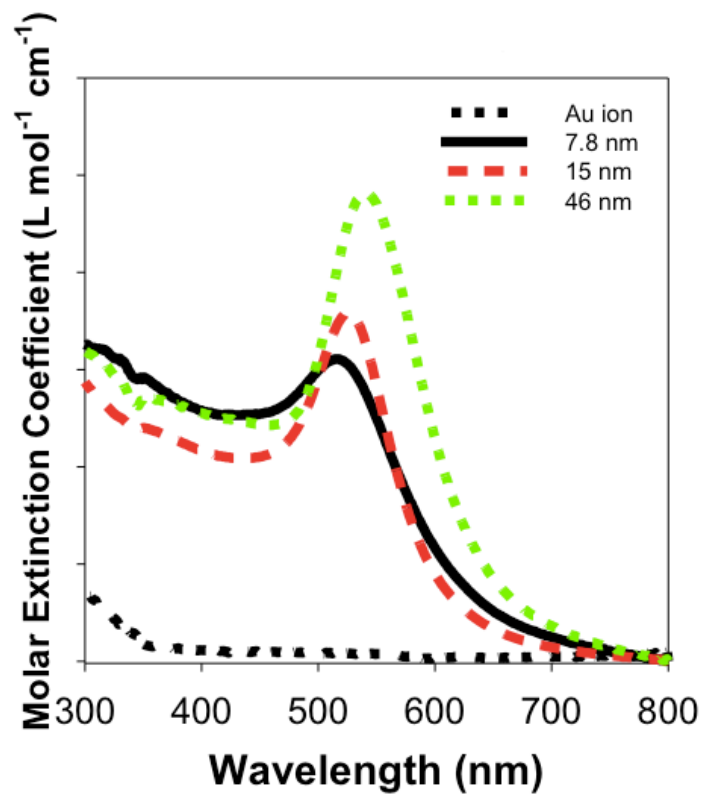


Figure 4-S2. Extinction spectra for the Au ion and 7.8, 15, and 46 nm gold nanoparticles.

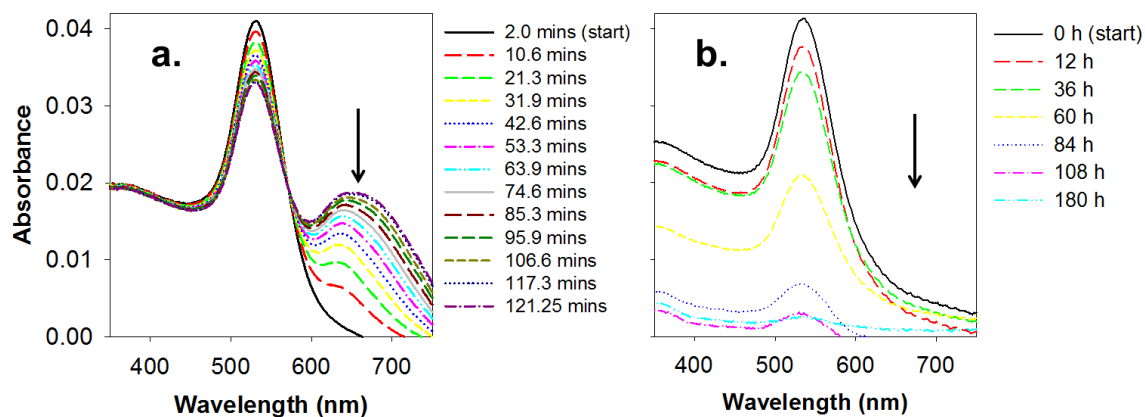


Figure 4-S3. Characteristic changes in absorbance spectra and the location or height of Abs_{SPR} over time due to (a) aggregation in EPA MHS after 120 min versus (b) particle clearance by a filter-feeding bivalve. The arrow denotes the location of a new absorption band that forms upon aggregation of AuNP, but is not evident when AuNP are cleared from suspensions via biological filtration.

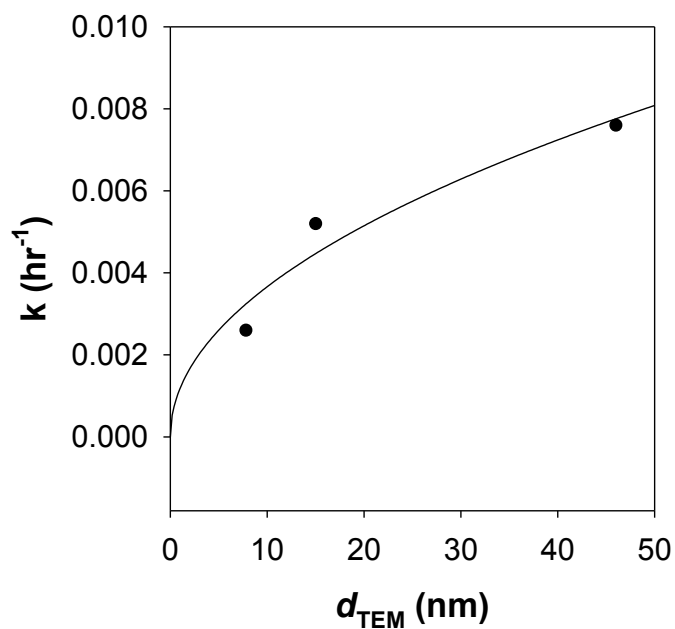


Figure 4-S4. Plot showing first-order rate constants for clearance of BSA-AuNP as a function of primary particle diameter.

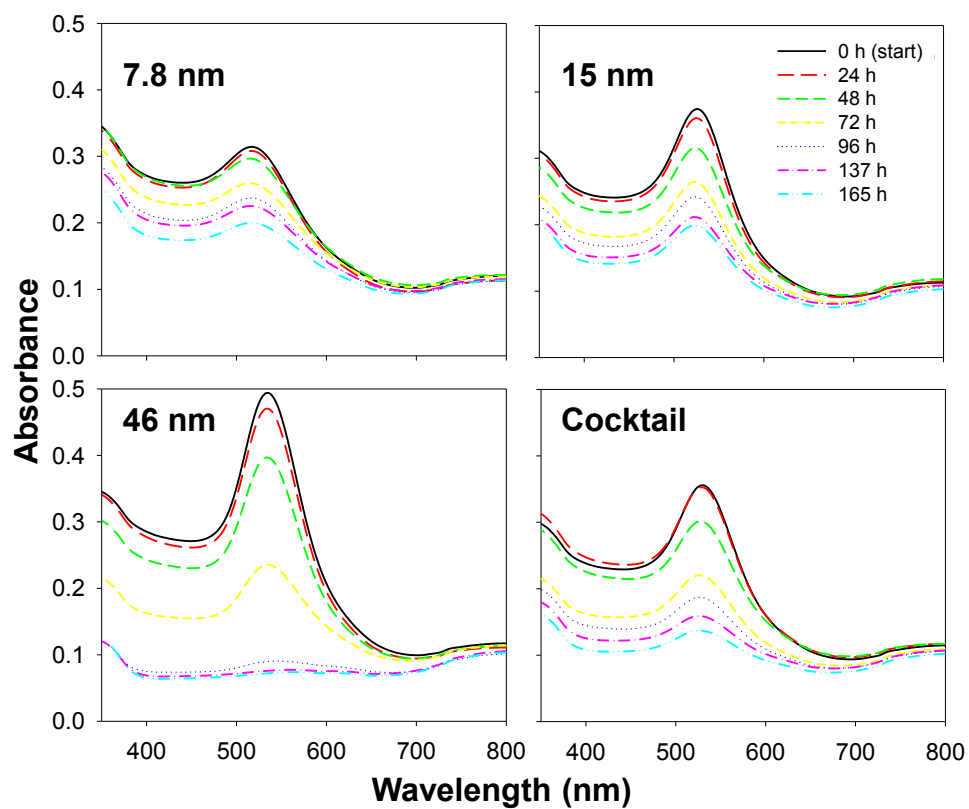


Figure 4-S5. UV-Vis spectra showing the time-dependent decrease in absorbance intensity of the SPR band of three sizes of BSA-AuNP—prepared individually and in combination as a ‘cocktail’ at a concentration of 15 mg L⁻¹ as [Au]—in the presence of *C. fluminea*.

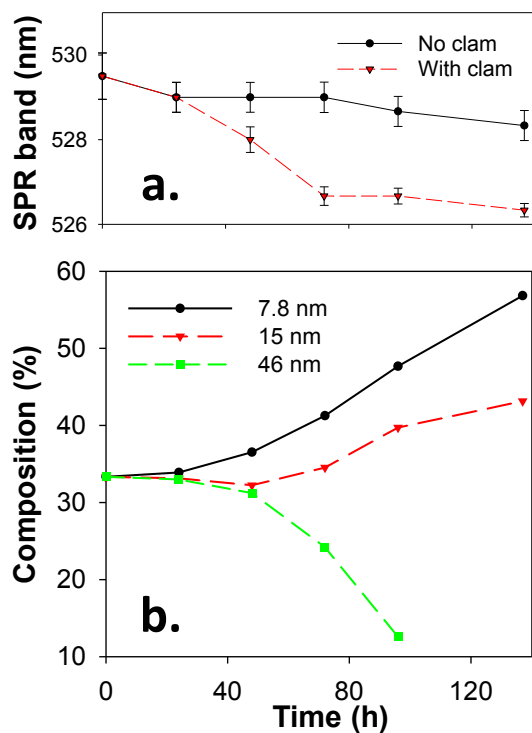


Figure 4-S6. (a) Plot of the mean blue shift \pm SD ($n = 3$) observed for the SPR band of the cocktail in the presence and absence of clams and **(b)** the predicted change in the respective contributions of each size of particle to the overall composition of the cocktail based on the size-dependent clearance rates. Beyond 96 h, the composition of 46 nm BSA-AuNP was below detection limits.

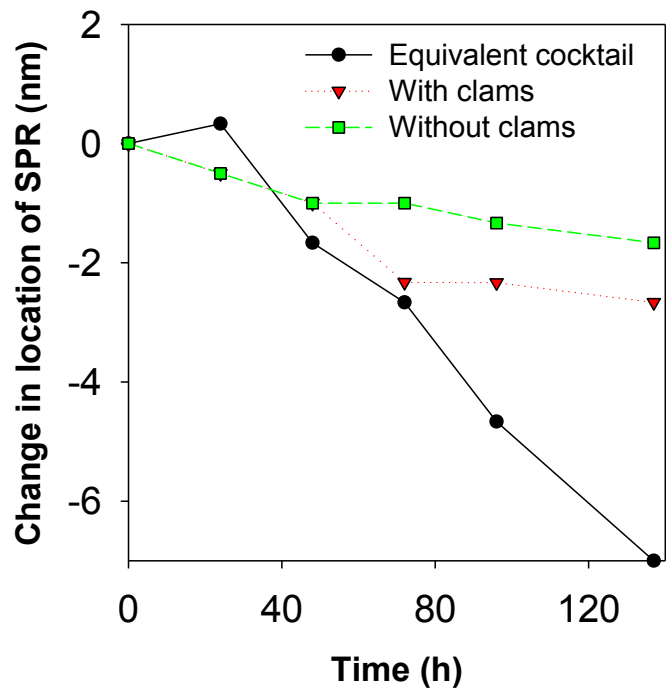


Figure 4-S7. Comparison of average SPR band shift for BSA-AuNP cocktails from the size-selective uptake experiment (with and without clams) and the experiment with cocktails prepared at the particle size composition and total [Au] predicted from the size-selective uptake experiment.

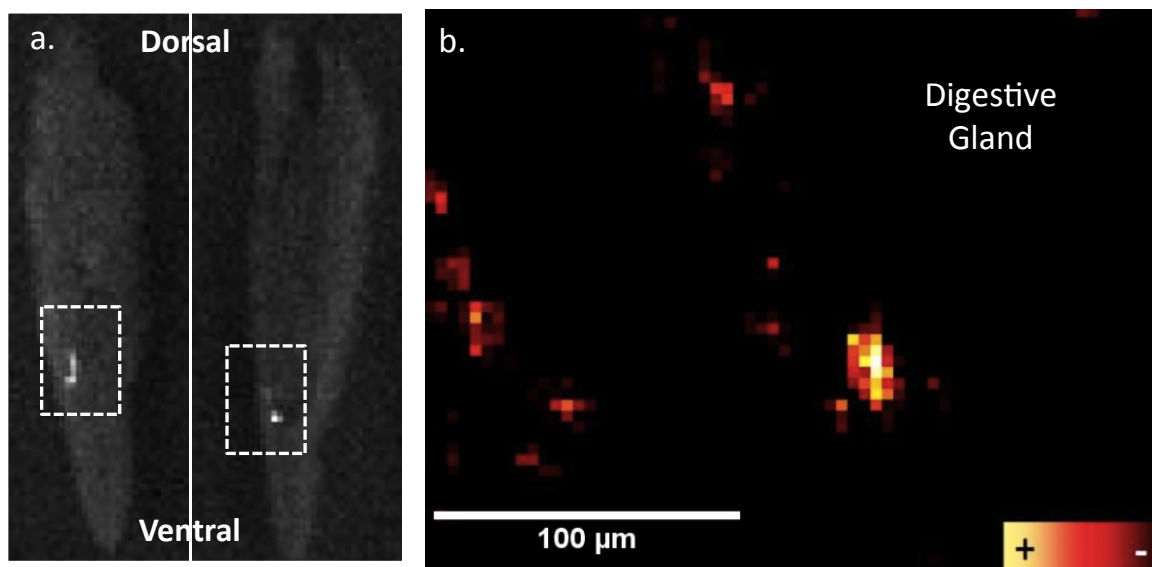


Figure 4-S8. (a) μ -XRF image of *C. fluminea* tissue cross-sections showing the internalization of Au (light areas surrounded by dashed boxes) within the digestive tract; (b) synchrotron-based μ -XRF (LUCIA beamline) Au map of a cross-section of the *C. fluminea* digestive gland.

Table 4-S1. Characteristics of BSA-AuNP. Size of primary particles on a TEM grid ($n \geq 100$) is expressed as the median value of the size determined using ImagePro and as the diameter predicted by Haiss et al. using the location and height of the surface Plasmon resonance (SPR) band.¹ Mean effective hydrodynamic diameter (Z_{ave} , nm), polydispersity index (PDI), electrophoretic mobility ($\mu\text{m cm (Vs)}^{-1}$), and location of the SPR band as measured in EPA moderately hard reconstituted water (EPA MHS).

BSA-AuNP Suspension	TEM (nm)	Predicted by			Electrophoretic mobility ($\mu\text{m cm (Vs)}^{-1}$)	SPR band (nm)
		Haiss et al. (nm)	Z_{ave} (nm)	PDI		
8 nm	7.8 ± 3.3	4.2	12.9 ± 0.4	0.23 ± 0.03	-1.06 ± 0.45	518
15 nm	15 ± 6.8	11	31.9 ± 0.3	0.24 ± 0.00	-1.96 ± 0.19	523
46 nm	46 ± 5.3	38	44.1 ± 0.1	0.29 ± 0.00	-1.80 ± 0.07	536

4.7 References

1. Daniel, M.; Astruc, D., Gold nanoparticles: assembly, supramolecular chemistry, quantum-size-related properties, and applications toward biology, catalysis, and nanotechnology. *Chem Rev* **2004**, 104 (1), 293-346.
2. Giersig, M.; Mulvaney, P., Preparation of ordered colloid monolayers by electrophoretic deposition. *Langmuir* **1993**, 9, 3408-3413.
3. Park, S.Y.; Lytton-Jean, A.K.R.; Lee, B.; Weigand, S.; Schatz, G.C.; Mirkin, C.A., DNA-programmable nanoparticle crystallization. *Nature* **2008**, 451 (7178), 553-556.
4. Murphy, C.J.; Gole, A.M.; Stone, J.W.; Sisco, P.N.; Alkilany, A.M.; Goldsmith, E.C.; Baxter, S.C., Gold Nanoparticles in Biology: Beyond Toxicity to Cellular Imaging. *Accounts Chem Res* **2008**, 41 (12), 1721-1730.
5. Röcker, C.; Pötzl, M.; Zhang, F.; Parak, W.J.; Nienhaus, G.U., A quantitative fluorescence study of protein monolayer formation on colloidal nanoparticles. *Nat Nanotechnol* **2009**, 4, 577-580.
6. Tkachenko, A.; Xie, H.; Liu, Y.; Coleman, D.; Ryan, J.; Glomm, W.; Shipton, M.; Franzen, S.; Feldheim, D., Cellular trajectories of peptide-modified gold particle

- complexes: comparison of nuclear localization signals and peptide transduction domains. *Bioconjugate Chem* **2004**, 15 (3), 482-490.
7. Cedervall, T.; Lynch, I.; Lindman, S.; Berggard, T.; Thulin, E.; Nilsson, H.; Dawson, K.; Linse, S., Understanding the nanoparticle-protein corona using methods to quantify exchange rates and affinities of proteins for nanoparticles. *P Natl Acad Sci USA* **2007**, 104 (7), 2050-2055.
 8. Moreau, J.; Weber, P.; Martin, M.; Gilbert, B.; Hutcheon, I.; Banfield, J., Extracellular proteins limit the dispersal of biogenic nanoparticles. *Science* **2007**, 316, 1600-1603.
 9. Kratz, F., Albumin as a drug carrier: design of prodrugs, drug conjugates and nanoparticles. *J Control Release* **2008**, 132 (3), 171-183.
 10. Leo, E.; Contado, C.; Bortolotti, F.; Pavan, B.; Scatturin, A.; Tosi, G.; Manfredini, S.; Angusti, A.; Dalpiaz, A., Nanoparticle formulation may affect the stabilization of an antiischemic prodrug. *Int J Pharm* **2006**, 307 (1), 103-113.
 11. Doherty, F.G., The Asiatic Clam, *Corbicula* Spp, as a Biological Monitor in Fresh-Water Environments. *Environ Monit Assess* **1990**, 15 (2), 143-181.
 12. Croteau, M.N.; Luoma, S.N., Delineating copper accumulation pathways for the freshwater bivalve *Corbicula* using stable copper isotopes. *Environ Toxicol Chem* **2005**, 24 (11), 2871-2878.
 13. Champeau, O.; Narbonne, J.F.S., Effects of tributyltin and 17 beta-estradiol on immune and lysosomal systems of the Asian clam *Corbicula fluminea* (M.). *Environ Toxicol Phar* **2006**, 21 (3), 323-330.
 14. Belanger, S.E.; Cherry, D.S.; Cairns, J.; McGuire, M.J., Using Asiatic Clams as a Biomonitor for Chrysotile Asbestos in Public Water-Supplies. *J Am Water Works Ass* **1987**, 79 (3), 69-74.
 15. Blaise, C.; Trottier, S.; Gagne, F.; Lallement, C.; Hansen, P.D., Immunocompetence of bivalve hemocytes as evaluated by a miniaturized phagocytosis assay. *Environ Toxicol* **2002**, 17 (3), 160-169.
 16. Graczyk, T.K.; Fayer, R.; Cranfield, M.R.; Conn, D.B., Recovery of waterborne *Cryptosporidium parvum* oocysts by freshwater benthic clams (*Corbicula fluminea*). *Appl Environ Microb* **1998**, 64 (2), 427-430.
 17. Miller, W.A.; Gardner, I.A.; Atwill, E.R.; Leutenegger, C.M.; Miller, M.A.; Hedrick, R.P.; Melli, A.C.; Barnes, N.M.; Conrad, P.A., Evaluation of methods for improved detection of *Cryptosporidium* spp. in mussels (*Mytilus californianus*). *J Microbiol Meth* **2006**, 65 (3), 367-379.

18. Ferry, J.; Craig, P.; Hexell, C.; Sisco, P.; Frey, R.; Pennington, P.; Fulton, M.; Scott, I.; Decho, A.; Kashiwada, S.; Murphy, C.; Shaw, T., Transfer of gold nanoparticles from the water column to the estuarine food web. *Nat Nanotechnol* **2009**, 4, 441-444.
19. Renault, S.; Baudrimont, M.; Mesmer-Dudons, N.; Gonzalez, P.; Mornet, S.; Brisson, A., Impacts of gold nanoparticle exposure on two freshwater species: a phytoplanktonic alga (*Scenedesmus subspicatus*) and a benthic bivalve (*Corbicula fluminea*). *Gold Bull* **2008**, 41 (2), 116-126.
20. Li-Mei, A.; Feng, G.; Bi-Feng, P.; Da-Xiang, C.; Hong-Chen, G., Interaction between gold nanoparticles and bovine serum albumin or sheep antirabbit immunoglobulin G. *Chinese J Chem* **2006**, 24, 253-256.
21. Jana, N.; Gearheart, L.; Murphy, C., Wet chemical synthesis of high aspect ratio cylindrical gold nanorods. *J. Phys. Chem. B* **2001**, 105, 4065-4067.
22. Turkevich, J.; Stevenson, P.C.; Hillier, J.A., Study of the nucleation and growth processes in the synthesis of colloidal gold. *Discuss. Faraday Soc.* **1951**, 11, 55-59.
23. Frens, G., Controlled nucleation for the regulation of the particle size in monodisperse gold suspensions. *NPHS* **1973**, 241, 20-22.
24. Ji, X.; Song, X.; Li, J.; Bai, Y.; Yang, W.; Peng, X., Size control of gold nanocrystals in citrate reduction: the third role of citrate. *J. Am. Chem. Soc.* **2007**, 129 (45), 13939-13948.
25. APHA; AWWA; WEF, Standard Methods for Examination of Water and Wastewater. **1998**.
26. Laforsch, C.; Tolldrian, R., A new preparation technique for daphnids for scanning electron microscopy by using hexamethyldisilazane. *Arch. Hydrobiol.* **2000**, 149, 587-596.
27. Flank, A.M.; Cauchon, G.; Lagarde, P.; Bac, S.; Janousch, M.; Wetter, R.; Dubuisson, J.M.; Idir, M.; Langlois, F.; Moreno, T.; Vantelon, D., LUCIA, a microfocus soft XAS beamline. *Nuclear Instruments and Methods in Physics Research B* **2006**, 246, 269-274.
28. Haiss, W.; Thanh, N.; Aveyard, J.; Fernig, D., Determination of size and concentration of gold nanoparticles from UV-Vis spectra. *Anal Chem* **2007**, 79, 4215-4221.
29. Diegoli, S.; Manciulea, A.; Begum, S.; Jones, I.; Lead, J.; Preece, J., Interaction between manufactured gold nanoparticles and naturally occurring organic macromolecules. *Sci Total Environ* **2008**, 402, 51-61.

30. Khlebtsov, N.; Dykman, L.; Krasnov, Y.; Mel'nikov, A., Light absorption by the clusters of colloidal gold and silver particles formed during slow and fast aggregation. *Colloid J* **2000**, 62 (6), 765-779.
31. Wiesner, M.R.; Lowry, G.V.; Alvarez, P.; Dionysiou, D.; Biswas, P., Assessing the risks of manufactured nanomaterials. *Environ Sci Technol* **2006**, 40 (14), 4336-4345.
32. Kryger, J.; Riisgard, H., Filtration rate capacities in 6 species of European freshwater bivalves. *Oecologia* **1988**, 77, 34-38.
33. Kennedy, A.J.; Hull, M.S.; Steevens, J.A.; Dontsova, K.M.; Chappell, M.A.; Gunter, J.C.; Weiss, C.A., Factors influencing the partitioning and toxicity of nanotubes in the aquatic environment. *Environ Toxicol Chem* **2008**, 27 (9), 1932-1941.
34. Way, C.A.; Hornbach, D.J.; Miller-Way, C.A.; Payne, B.S.; Miller, A.C., Dynamics of filter feeding in *Corbicula fluminea* (Bivalvia: Corbiculidae). *Can. J. Zool.* **1990**, 68, 115-120.
35. Hornbach, D.J.; Way, C.M.; Wissing, T.E.; Burky, A.J., Effects of particle concentration and season on the filtration rates of the freshwater clam, *Sphaerium striatinum* Lamarck (Bivalvia: Pisidiidae). *Hydrobiologia* **1984**, 108, 83-96.
36. Morton, B., Studies on the biology of *Dreissena polymorpha* Pall. v. Some aspects of filter-feeding and the effect of microorganisms upon the rate of filtration. *Proc Malacological Soc London* **1971**, 39, 289-301.
37. Riisgard, H., Efficiency of particle retention and filtration rate in 6 species of Northeast American bivalves. *Marine Ecology Progress Series* **1988**, 45, 217-223.
38. Silverman, H.; Lynn, J.W.; Beninger, P.G.; Dietz, T.H., The role of the latero-frontal cirri in particle capture by the gills of *Mytilus edulis*. *Biol Bull* **1999**, 197, 368-376.
39. Mohlenberg, F.; Riisgard, H.U., Efficiency of particle retention in 13 species of suspension feeding bivalves. *Ophelia* **1978**, 17, 239-246.
40. Vahl, O., Efficiency of particle retention in *Mytilus edulis* L. *Ophelia* **1972**, 10, 17-25.
41. Ropert, M.; Gouletquer, P., Comparative physiological energetics of two suspension feeders: polychaete annelid *Lanice conchilega* (Pallas 1766) and Pacific cupped oyster *Crassostrea gigas* (Thunber 1795). *Aquaculture* **2000**, 181, 171-189.
42. van Sprang, H., Fundamental parameter methods in XRF spectroscopy. *Advances in X-ray Analysis* **2000**, 42, 1-10.
43. Ward, J.E.; Kach, D.J., Marine aggregates facilitate ingestion of nanoparticles by suspension-feeding bivalves. *Mar Environ Res* **2009**, 68, 137-142.

44. Haven, D.S.; Alamo, R.M., Aspects of biodeposition by oysters and other invertebrate filter feeders. *Limnol Oceanogr* **1966**, 11 (4), 487-498.

Chapter 5. Uptake and retention of metallic nanoparticles in the Mediterranean mussel (*Mytilus galloprovincialis*)

Matthew S. Hull^{1,2,3}, Marvin G. Warner⁴, Peter J. Vikesland^{1,2,3}, and Irvin R. Schultz^{5*}

¹Virginia Tech Department of Civil and Environmental Engineering, Blacksburg, VA, USA

²Virginia Tech Institute for Critical Technology and Applied Science (ICTAS) Center for Sustainable Nanomaterials (VT SuN), Blacksburg, VA, USA

³Center for the Environmental Implications of Nanotechnology (CEINT), Duke University, Durham, NC, USA

⁴Pacific Northwest National Laboratory, Chemical Sciences Division, Richland, WA, USA

⁵Pacific Northwest National Laboratory, Marine Sciences Laboratory, Sequim, WA, USA

5.1 Abstract

In controlled laboratory exposures we measured the uptake, distribution and elimination of two types of metallic nanoparticles (MetNPs): polyethylene glycol functionalized paramagnetic 50 nm Fe₃O₄ nanoparticles (PEG-FeOxNP) and 8 × 3 nm (length × diameter) quantum dots (Invitrogen Qdot® 655 ITK, PEG-coated Cd-Se core (PEG-Qdot)) by the aquatic mussel *Mytilus galloprovincialis*. All MetNPs were dosed using static water exposures. Our focus was on collecting a dataset to estimate a mass-balance determination of MetNP fate within test organisms. Water-column exposures used individual mussels placed in Pyrex® aquariums

containing known volumes of water maintained under natural photoperiod and constant temperature. Stability of the MetNP suspensions in seawater test media was monitored prior to the addition of test organisms. Water samples were removed prior to and during filtering activity to assess the uptake of MetNP from the water. At selected time points, groups of mussels were serially euthanized and various tissues (hemolymph, digestive gland, remaining carcass) dissected and analyzed for the presence of MetNP ions by ICP-OES (Fe in FeOxNPs) or ICP-MS (Cd in Cd-Se Qdots). Results indicated that all MetNPs were rapidly accumulated by the mussels with >90% of the MetNPs accumulated within 8 h of initial exposure. Metal analysis of tissues indicated that nearly the entire retained dose of FeOxNPs was deposited in the digestive gland whereas PEG-Qdots appear to have been rapidly eliminated from mussels as feces. These results provide important insights on the uptake and elimination kinetics of MetNPs in filter-feeding marine bivalves, and may be useful for subsequent development of toxicokinetic models to predict the kinetics of these processes.

5.2 Introduction

The paucity of data on the biological fate of nanoparticles in aquatic organisms has hindered development of explanatory frameworks and predictive models to estimate bioavailability, retention, and potential for trophic transfer within food webs. To better comprehend the consequences of environmental nanoparticle release, it is important to understand how variations in the physical and chemical properties of nanoparticles impact toxicokinetic processes that ultimately determine bioavailability. Aquatic environments are the ultimate sink for most persistent contaminants and this may also be the case for nanoparticles resistant to environmental degradation. There is a need to better understand how the physicochemical properties of

nanoparticles affect their absorption by, tissue distribution within, and excretion by aquatic animals. Understanding how these properties influence MetNP uptake and retention in filter-feeding invertebrates such as bivalves that actively ingest particulate matter is especially critical as these invertebrates are common prey items and serve as a food source for man, thus raising concerns about potential biomagnification of MetNPs at higher trophic levels.

The current work investigated the biological fate of two metallic nanoparticles (MetNPs)—iron oxide nanoparticles (FeOxNP) with and without a polyethylene glycol (PEG) coating and PEG-coated quantum dots (PEG-Qdot)—in a marine mussel. Nanoparticle disposition and bioavailability were assessed using water column exposures. A preliminary mass balance model was developed to determine particle bioavailability and clearance within test organisms. These results provide fundamental information on both the environmental and biological fate of MetNPs in estuarine environments.

Environmental significance of metallic nanoparticles. The production and search for commercial applications of nanoscale structures has been acclaimed as the next great general purpose technology that will impact society in a manner similar to the electronic technologies of the 20th century.¹ A subset of nanoscale structures are nanoparticles, which have been defined by many authors as single particles with a diameter less than 100 nm and novel properties stemming from their small size.² Nanoparticles can be synthesized from almost any material, but can be broadly separated into carbon based, such as C₆₀ fullerenes and metal or metal oxides (collectively termed “metallic” nanoparticles or MetNPs henceforth). MetNPs can be divided into many sub categories including quantum dots, which are semiconducting nanocrystals varying in size from ~2 to 100 nm.³ MetNPs are finding a growing number of applications in the medical, industrial, military and environmental sectors.

The potential for widespread environmental release is a recognized concern as a result of manufacturing processes, accidental spillage and through commercial uses such as personal-care products (e.g. sunscreens⁴). Other proposed applications of metal oxide nanoparticles, such as iron oxides, are in environmental remediation.⁵ Still other types of MetNPs including those made from silver, gold, manganese, and molybdenum have a variety of military or biomedical uses.^{6,7} It is well known that aquatic sediments tend to be the ultimate repository for particulate bound contaminants.⁸ Thus, it is reasonable to assume a similar fate for MetNPs. This potential fate raises particular concerns for near-shore marine environments, which are expected to experience increased pollution from the growth of coastal urban centers.

Marine invertebrates as test organisms. It is well established that all aquatic invertebrates accumulate trace metals due to environmental exposures.⁹ The ability of sessile marine invertebrates to accumulate and tolerate high levels of contaminants such as trace metals has spurred the international development of “mussel watch” programs, which use mussels and other bivalves as environmental sentinels of pollution.¹⁰ Associated with these activities has been substantial research activity in the past few decades to better understand the bioavailability of metals to marine invertebrates and physiological processes that appear to regulate tissue and cellular distribution and excretion of metals.¹¹ The physicochemical form of absorbed metal in marine invertebrates is generally considered to exist in three different pools: small quantities freely soluble or in metabolically available forms (as for essential metals), bound with high affinity to specific proteins such as metallothioneins, and as insoluble nano- and micron sized granules.⁹ The formation of large metal granules in various tissues is a particularly interesting phenomenon well documented to occur in marine bivalves and decapod crustaceans (among other invertebrate groups) after laboratory and environmental exposures to a wide variety of

metals including Cu, Cd, Zn, Ti, Cr, Fe, Mo and Ag.¹²⁻¹⁷ The formation of metal granules particularly within digestive tissues is generally considered to be a detoxification process, with the granules eventually being excreted as a result of discharge of senescent cells into the feces.¹⁷ With regard to trophic transfer of trace metals among invertebrates, recent evidence suggests metal granules can be bioavailable to predators feeding on bivalves and other invertebrates, although the extent appears to vary depending in part on the metal composition of the granules.¹⁸⁻

20

The ability of marine invertebrates to form and store metallic nano-sized granules combined with the filter feeding behavior of bivalves such as mussels raises several important questions associated with exposure to synthetic MetNPs: can bivalves such as mussels accumulate and retain metallic nanoparticles; are all metallic nanoparticles accumulated alike or can mussels discriminate between particles; will metallic nanoparticles be stored and eliminated in a similar manner to naturally formed metal granules; and what is the potential for trophic transfer of MetNPs to predators?

Overview of nanoparticle kinetics in animals. Results from mammalian studies using iron oxide or biodegradable nanoparticles of various sizes suggest that after intravascular injection, nanoparticles can be rapidly cleared from the bloodstream within minutes by a process known as opsonization, which involves the binding of opsonin proteins to the surface of the particle and subsequent removal by the reticulo-endothelial system (RES).^{21, 22} The RES removal process tends to cause non-biodegradable particles (such as iron oxide) to accumulate in the liver and spleen, which are the major tissues comprising the RES.²³ However, this process can be disrupted by surface modifications to the nanoparticles that disrupt attachment of opsonin proteins thus prolonging by hours to days nanoparticle clearance from the bloodstream.²⁴ In

addition to surface characteristics, another factor influencing blood clearance is size, with nanoparticles below 200 nm in diameter generally cleared more slowly than larger particles.^{23,25} Perhaps because most pharmaco-/toxicokinetic studies of nanoparticles are motivated by therapeutic implications, there has been a notable lack of studies on nanoparticles comprised of metallic cores other than iron oxide, preventing generalization about how the chemical properties of the nanoparticle core impact particle clearance rates and tissue distribution.

There has been very little research effort to understand the biological fate of nanoparticles in aquatic organisms. Although invertebrates have a simplified version of the complement system,²⁶ it is unclear whether nanoparticles can be efficiently removed as compared to higher vertebrates. Of greatest relevance to this work, is the recent study by Haye et al.²⁷ characterizing the uptake of spherical, latex nanoparticles varying in size from 40–1000 nm in the American oyster (*Crassostrea virginica*). This study reported that oysters were able to completely remove by filtering activity, 90-99% of the 40 nm latex particles from a 0.4 L solution (initial concentration 2 mg L⁻¹) within 4-10 hrs. This result provides an indication of the potential for nanoparticle accumulation to occur in marine bivalves. Other studies, however, have shown that particle clearance rates vary considerably based on bivalve species and composition. For example, Hull et al.²⁵ reported that >180 h were required for *Corbicula fluminea*, to effectively clear 2 mg L⁻¹ (as Au) suspensions of protein-stabilized gold nanoparticles. In this same study, particle clearance rates were related positively to primary particle diameter in the size range of 7 to 46 nm.

Need for explanatory frameworks and use of QSAR models for nanoparticles. The expanding diversity of nanoparticles underscores the need for basic studies relating nanoparticle physical and chemical properties with biological fate and toxicity. Development of structure

activity relationships for nanoparticles is a recognized priority worldwide to both focus experimental studies towards critical data gaps and provide risk assessors with a rational approach for estimating environmental impacts.²⁸ With respect to MetNPs, important unresolved questions are related to whether any aspects of conceptual models for metal bioaccumulation in aquatic animals are relevant to nanoparticles. In the worst-case scenario, all that has been learned previously for metal bioaccumulation is useless towards understanding nanoparticle kinetic behavior. Alternatively, there may be certain fundamental aspects of metal ion characteristics that can be used to allow prediction of nanoparticle bioavailability and disposition once confounding variables associated with nanoparticle physicochemical properties are better understood. Therefore, an important aspect of the present work was the collection of a detailed toxicokinetic dataset on two different MetNPs that when integrated with findings from other MetNPs studies will permit statistical analysis using various predictive models of metal bioaccumulation, including metal ionic characteristics. The latter has been successfully used to relate overall bioaccumulation or assimilation^{29, 30} and also specific aspects of metal toxicokinetics such as blood clearance after environmental exposures or intravascular injection in aquatic animals.³¹ These examples are in addition to many studies of metal toxicity and structure activity in diverse organisms from bacteria to rodents.³²⁻³⁵

5.3 Experimental Section

Synthesis and physical characterization of MetNPs. Carboxylic acid-terminated iron oxide nanoparticles (FeOxNP) of 50 nm diameter and stabilized in deionized water were purchased from Ocean Nanotech (Springdale, AR). Varying surface chemistries were evaluated to achieve stabilized suspensions of FeOxNP in seawater exposure media. Ultimately, a surface coating consisting of amine-terminated polyethylene glycol (PEG) was selected for subsequent

exposures as it prolonged the stability of FeOxNP in seawater test media relative to an FeOxNP suspension that was not stabilized with PEG (Figure 5-1). PEG-FeOxNP were prepared by first activating the terminal carboxylic acid groups present on FeOxNP surfaces using carbodiimide and N-hydroxysuccinimide, followed by conjugation to a terminal amino group present on the PEG molecule. In addition to PEG-stabilization of FeOxNP, one experiment involved stabilization of FeOxNP by extended stirring of FeOxNP in humic acid (HA). The HA-FeOxNP were not stable in seawater test media, but their uptake by mussels was nevertheless investigated given the potential relevance of organic matter-stabilization of nanoscale particles to real-world environmental systems. Samples of PEG-FeOxNP suspended in 0.45 μm filtered Sequim Bay seawater (SW) were prepared for analysis by Transmission Electron Microscopy (TEM) by dropcasting onto carbon and Formvar coated copper grids. TEM analysis was carried out on a Zeiss 10CA TEM (60 kV) equipped with a high resolution (1024 \times 1024 pixel format) MT Advantage GR/HR-B CCD Camera System (Advanced Microscopy Techniques Corporation). Determination of the elemental composition of the PEG-FeOxNPs was performed as follows: 2.5 mg of the material was fully dissolved in 5 mL of concentrated (15.6 M) HNO_3 at room temperature after about 2 h contact time; the samples were then diluted 1600-fold in 1% (v/v) HNO_3 and analyzed for Fe using an inductively coupled plasma-mass spectrometer (ICP-MS, Agilent 7500ce, Agilent Technologies, CA).

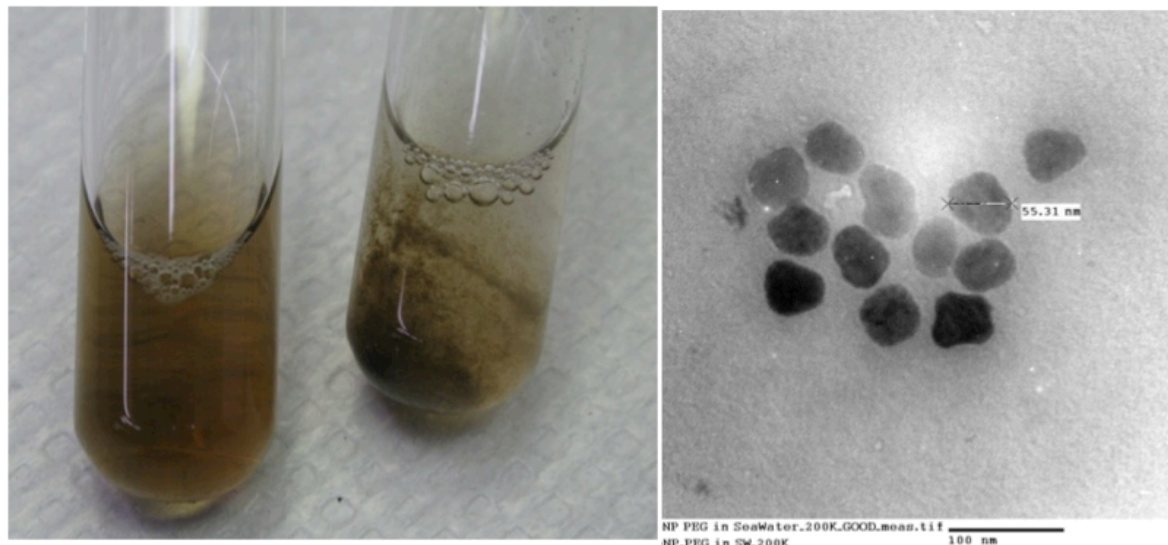


Figure 5-1. a) Suspensions of FeOxNP stabilized with PEG (left) and unstabilized (right) prepared in SW—note the visible aggregates in the unstabilized FeOxNP suspension on the right; b) TEM image of PEG-FeOxNP.

Carboxylic acid-terminated quantum dots (Qdot® ITK™) of approximately 8 nm length and 3 nm diameter comprised of a semiconducting CdSe core and ZnS shell were purchased from Invitrogen (Figure 5-2). The core-shell particles were coated with a PEG layer to permit facile dispersion and retention of their optical properties in common aqueous matrices. The particles exhibited a symmetric optical emission band with an emission maxima near 655 nm.

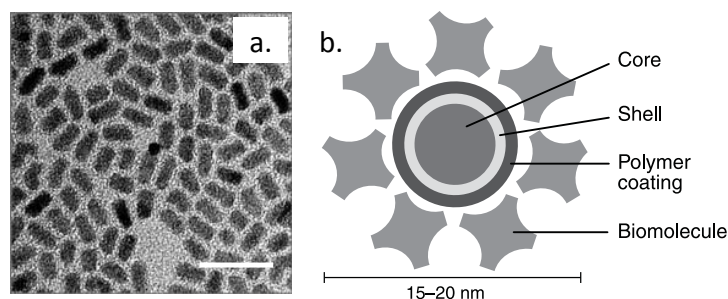


Figure 5-2. Manufacturer-reported information for Invitrogen Qdot® ITK 655 quantum dots: a) TEM image of core-shell Qdot® nanoparticles at 200,000x magnification—scale bar = 20 nm. b) Schematic of Qdot® conjugate structure. Image credit: Copyright © 2011, Invitrogen.

Water column exposures. Experiments were performed to focus on collecting a data set for nanoparticle accumulation and tissue distribution that allows for mass-balance determinations of a) nanoparticle transfer from the water column to the animal as well as b) nanoparticle fate within test organisms. Mediterranean mussels (*M. galloprovincialis*) were obtained from local Puget Sound growers (Penn Cove, Whidbey Island WA) and held in flowing raw seawater from Sequim Bay. We then used a static exposure system (Figure 5-3) similar to that used in previous toxicokinetic studies by Schultz and Hayton employing fish³⁶ and by others with bivalves and latex nano- and micron-sized particles.²⁷ Individual mussels were placed in one liter beakers partially filled (0.75 L) with sterile filtered Sequim Bay seawater (SW). The beakers were placed in a large (1 m wide × 2.5 m long × 0.3 m deep) water table flooded with SW providing a near constant temperature water bath during the experiment. Prior to placement of a mussel in the exposure beakers, each beaker was seeded with a specific quantity of PEG-FeOxNP, HA-FeOxNP, or PEG-Qdot. Constant aeration was provided to maintain desired dissolved oxygen levels and to help maintain circulation of the nanoparticles within the exposure tank. Next, a single mussel of 20-25 g total wet weight was added to each of three replicate beakers (n = 3) and observed for filtering behavior, which typically began within 5-20 minutes. Water samples were removed before and during filtering activity to assess uptake of MetNPs from the water column. At selected time points, groups of mussels were serially euthanized and hemolymph samples removed from the posterior adductor muscle sinus, along with gills, intestinal, and digestive gland tissues. Exposure beakers were also prepared that contained either a mussel shell or a mussel that had been banded closed to prevent filtering activity.

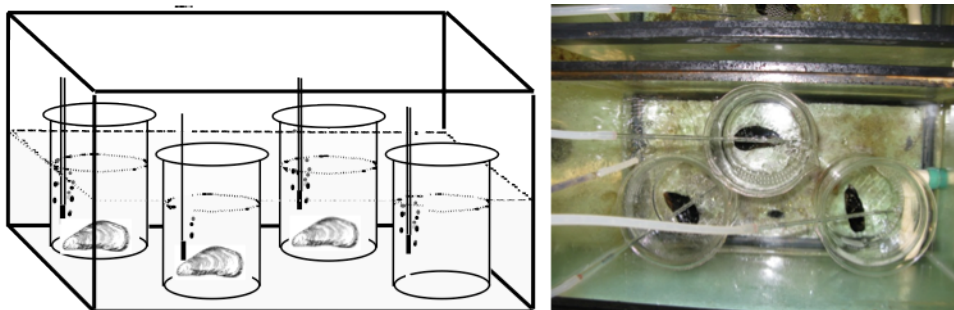


Figure 5-3. Experimental set-up for water column exposures.

Time-course analysis of MetNPs in dosing solutions and water column and tissue samples. The total metal content of water and tissue samples (corrected for background levels) collected from the mussel experiments was determined using inductively-coupled plasma optical emission spectroscopy (ICP-OES) for all FeOxNPs and inductively-coupled plasma emission mass spectrometry (ICP-MS) for the PEG-Qdots. These data were used to prepare time-course MetNP water column and tissue concentration profiles based on the concentration of each metal in the sample. These profiles were used in subsequent toxicokinetic analysis, as described below. Due to high Fe background levels in bivalve tissue, a magnetically-assisted clean-up procedure was used to separate FeOxNP fractions from dissolved Fe. Briefly, soft tissue dissected from euthanized mussels was homogenized with a ground glass mortar and Teflon® pestel, diluted with deionized water 1:10, vortexed and centrifuged at $12,000 \times g$ for 10 min. to remove solid material; the supernatant was then placed on top of a magnet for 15 mins. Next, to wash the samples, $\frac{3}{4}$ of the supernatant was removed and then replaced with deionized water. This process was repeated three times to remove as much soluble Fe as reasonably possible. Finally, the bottom portion of the supernatant fraction was processed for analysis of Fe by ICP-OES. The ICP-OES / ICP-MS detection limits for Fe and Cd were in the 0.002 to $0.5 \mu\text{g g}^{-1}$ dry wt. range. To prepare dosing solutions, and water column and tissue samples for analysis of

metals, the solutions and samples were digested in high purity acids in a pre-cleaned sealed Teflon® vials. The digestates were diluted with 2% nitric acid and appropriate internal standards were added. Blanks, duplicates, matrix spikes, and certified reference materials, such as NIST Mussel Tissue SRM-2976 were prepared with each analytical batch.

5.4 Results and Discussion

Uptake and partitioning of PEG- and HA-FeOxNPs. Figure 5-4 summarizes the clearance and uptake of 50 nm PEG-FeOxNPs by mussels during the water column exposures. Based on the time-course Fe concentration profiles measured by ICP-MS in test and control beakers for 2.5 h prior to the addition of mussels, PEG-FeOxNP is relatively stable in the seawater test media (Figure 5-4a). Following addition of test organisms, clearance of PEG-FeOxNP occurred rapidly, with water column Fe concentrations reduced to 50% of the initial delivered Fe concentration within 1-2 h following the introduction of test organisms, and >90% of the initial water column Fe mass removed within 18 h (Figure 5-4b). The rapid rate at which PEG-FeOxNPs were cleared from suspension by *M. galloprovincialis* is more than 20 times faster than clearance rates reported for *C. fluminea*, for protein-stabilized gold nanoparticles.²⁵ Despite the numerous experimental differences between the two studies, which prevent direct comparison of the two works (e.g., differences in particle composition, t_0 nanoparticle concentration, surface coatings, assay media, test organisms), the dramatic difference in clearance rates between the studies is noteworthy and suggests distinct differences in how different species of bivalves process different types of MetNPs. For example, clusters of nanoparticles are likely to be cleared more rapidly than individually-stabilized particles;³⁷ and,

depending on the size of the laterofontal cirri of the gill, which are thought to play an important role in particle retention,³⁸ some bivalve species may be better suited for filtration and retention of smaller particles than others.³⁹

In shell-only and banded live mussel control beakers, Fe levels decreased throughout the assay by ~30% and <20%, respectively, suggesting that some sorption of PEG-FeOxNP to shells or assay containers may have occurred. Despite these losses to the system, it is apparent that *M. galloprovincialis* is capable of rapidly removing PEG-FeOxNP from suspension. Post-exposure, test organisms were washed with fresh seawater, transferred to clean beakers containing seawater only, and permitted to depurate for >84 h. Water column Fe levels did not increase appreciably (Figure 5-4c), suggesting that Fe was either retained by the test organisms for an extended period, or biodeposited to the subsurface as solid fecal matter. Either of these scenarios is likely given previous studies demonstrating both the retention of MetNPs in bivalve organ systems (primarily the digestive tract and digestive gland) and biodeposition of MetNPs in solid feces.²⁵

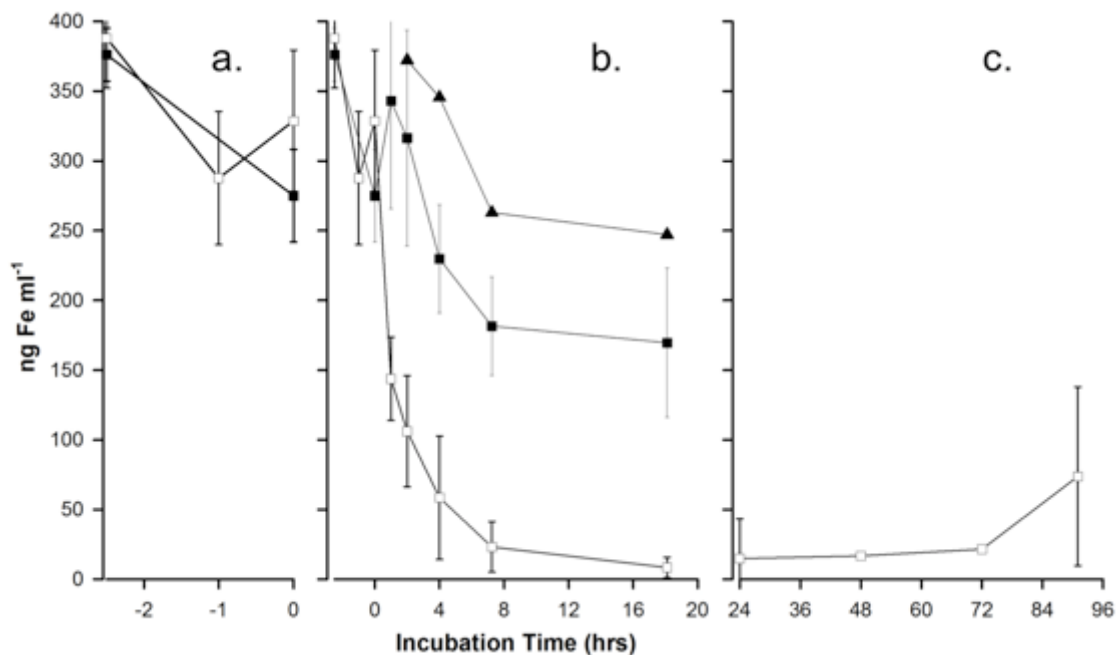


Figure 5-4. Uptake of 50 nm PEG-FeOxNPs from the water column by mussels. a) Pre-exposure evaluation of PEG-FeOxNP stability in SW. Total Fe was measured after PEG-FeOxNPs were isolated magnetically. b) Loss of Fe from water column after the addition of mussels to beakers (white squares, n = 3). Shell only beakers are black squares. Banded mussels (to prevent filtering) are represented by the black triangles. c) Fe measured in water column during depuration. After exposure, mussels were washed in clean SW and placed in new beakers with clean SW.

Following the termination of the exposure, levels of Fe were measured in the hemolymph, digestive gland and remaining carcass at exposure termination (18 h) and at 73 and 140 h post-exposure (mussels removed from PEG-FeOxNP exposure and allowed to depurate in fresh seawater). Immediately following termination, most of the Fe—greater than 90% of what was initially added to the exposure water—was retained within the digestive gland, while very little (2-4%) was retained within the remaining carcass (Figure 5-5a). These results suggest that the digestive gland of filter-feeding bivalves, and possibly ecologically similar biota, may serve as important organismal compartments for nanoparticle mass balances in aqueous systems.

Although Fe levels in the digestive gland decreased by $\approx 10\%$ after 73 h depuration, they remained elevated (Figure 5-5a).

Levels of Fe measured in hemolymph were greatest immediately following the uptake period, but decreased by nearly 50% after 73 h depuration (Figure 5-5b). Even after 73 h depuration, however, Fe levels in the actively-filtering mussels were 80% greater than those measured in the hemolymph of banded mussels that were allowed to depurate for the same period. After 140 h depuration, Fe levels decreased by nearly 70%, yet remained significantly greater than Fe levels measured in control mussels.

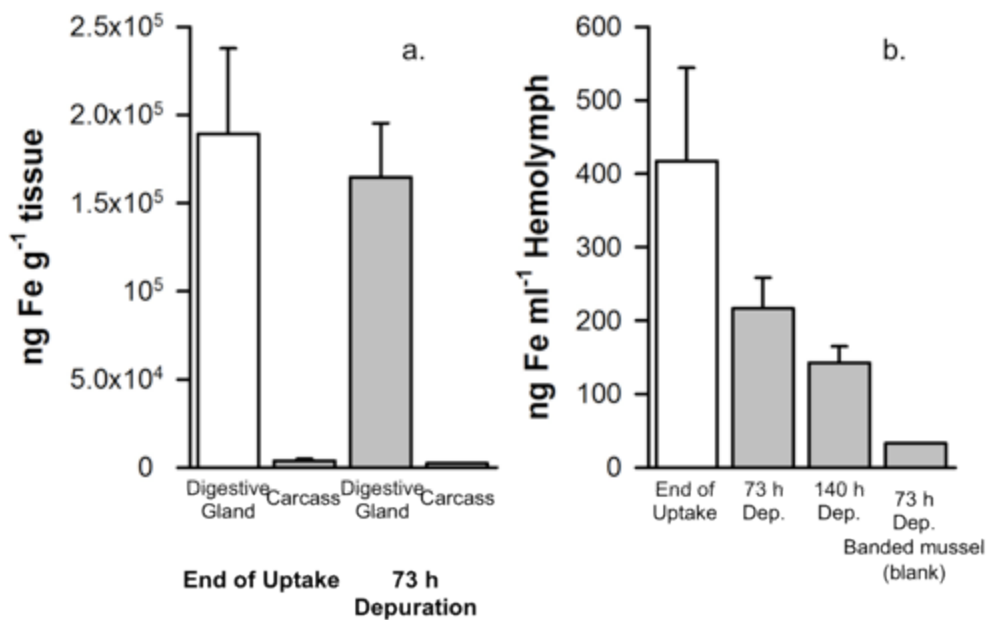


Figure 5-5. Levels of Fe in a) digestive gland and carcass at termination and after 18 and 73 h (n = 3), and b) hemolymph immediately following uptake plus 73 and 140 h depuration in fresh seawater. Note that most of the Fe, >90% of what was initially added to the exposure water is retained in the digestive gland. Very little Fe, 2-4 %, is retained in the remaining carcass.

In addition to investigating clearance of the polymer-stabilized iron particles (i.e., PEG-FeOxNP), we also evaluated the clearance and partitioning of humic-acid stabilized FeOxNP. As shown in Figure 5-6, the bioavailability of non-functionalized FeOxNPs was increased by the addition of humic acid (HA-FeOxNP), although this process is difficult to assess given that HA-FeOxNPs were unstable in seawater test media as evidenced by the dramatic decrease in water column Fe in shell-only controls. The instability of HA-FeOxNP in this test system is likely more indicative of the type of behavior displayed by most non-functionalized nanoscale materials, particularly upon addition to high ionic strength marine and estuarine waters. Thus, the loss of Fe in these exposures is likely attributable in part to aggregation and subsequent settling of the HA-FeOxNP. However, despite the overall instability of the test system, clearance rates for active mussels relative to shell-only controls indicate that the loss of Fe from the system was accelerated by mussel filtration (Figure 5-6). As shown in Figure 5-7, even though particles were aggregating, the accelerated clearance of HA-FeOxNP once again resulted in the disproportionate accumulation of Fe in the mussel digestive gland relative to the remaining carcass. Although clearance of HA-FeOxNPs via the independent processes of aggregation/settling and mussel filtration cannot be discerned separately in this case, these data nevertheless support our previous findings indicating that FeOxNPs are likely to accumulate in the digestive gland following uptake from the water column.

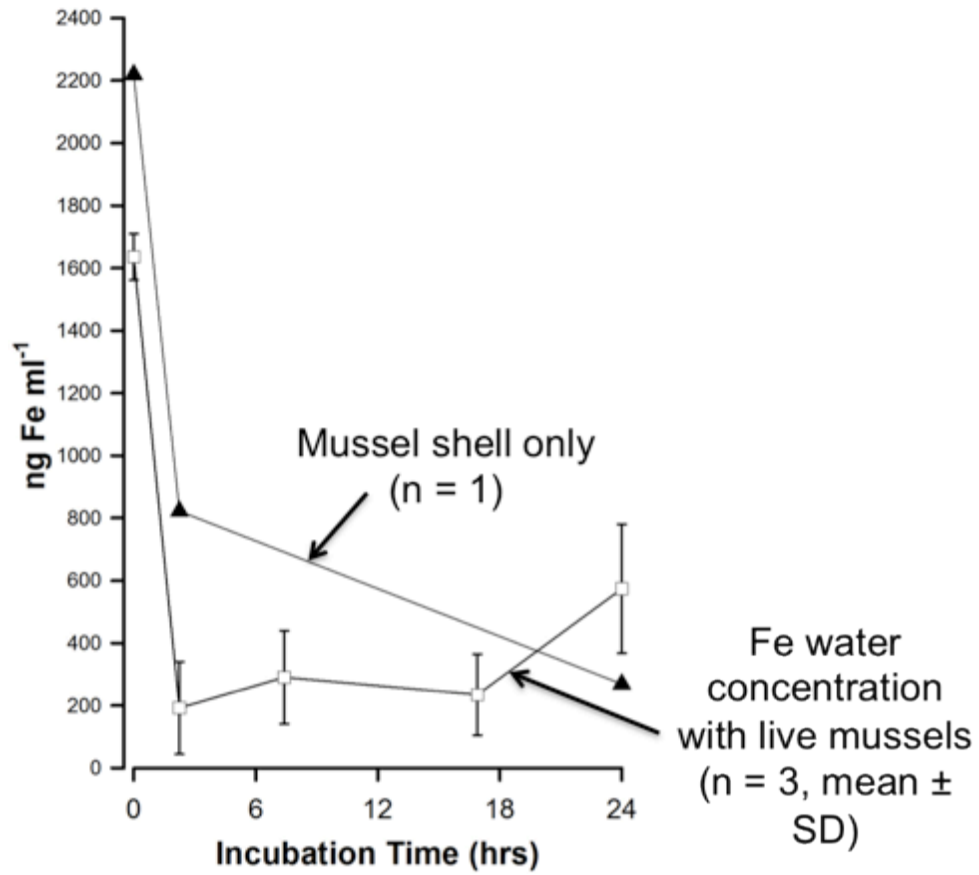


Figure 5-6. Loss of Fe from SW after adding mussels (white squares, n = 3). Black triangles indicate shell-only controls.

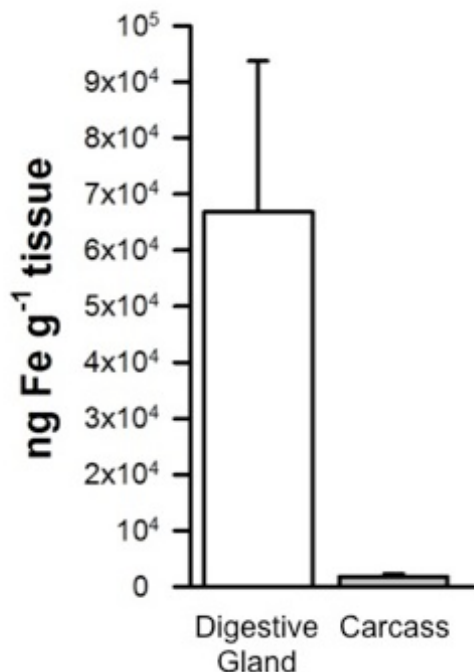


Figure 5-7. Total Fe in digestive gland and carcass following termination of mussel exposures to HA-FeOxNP.

Uptake and partitioning of PEG-Qdots. Similar to what was observed for PEG-FeOxNP, PEG-Qdots stabilized in seawater media (Figure 5-8a) were rapidly cleared from suspension and presumably accumulated by mussels during water column exposures (Figure 5-8b). During depuration, Cd was not detectable in the water column (Figure 5-8c), suggesting that like PEG- and HA-FeOxNP, PEG-Qdots either were retained within mussels or incorporated within feces and egested to the bottom of the test chamber.

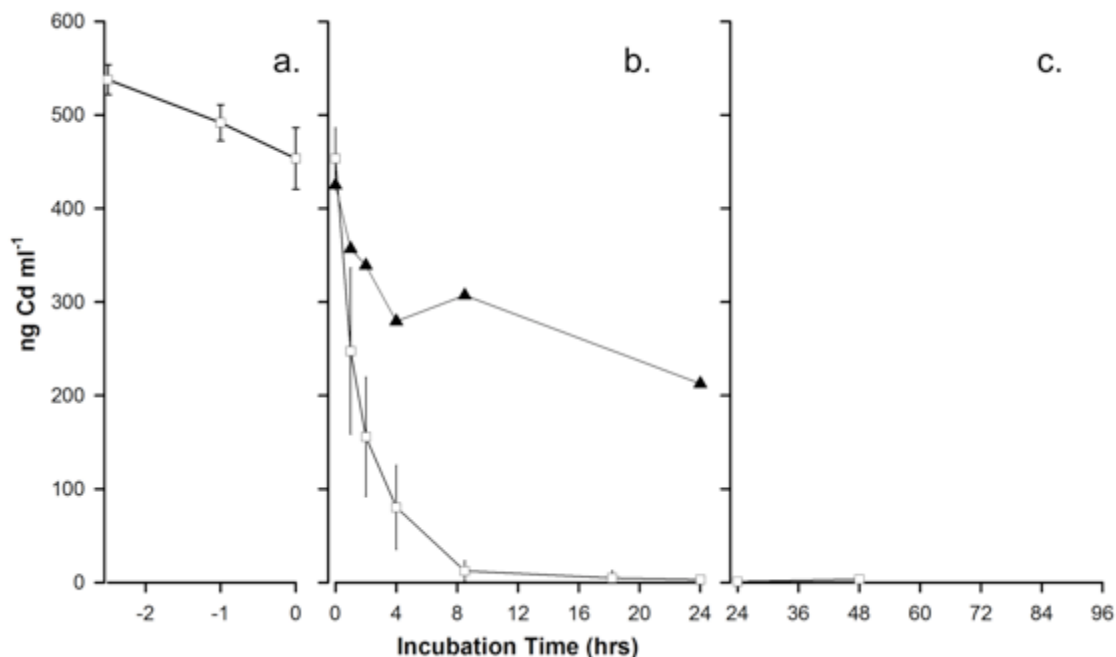


Figure 5-8. a) Pre-exposure tests for PEG-Qdot stability in solution as determined by levels of Cd. b) Uptake of PEG-Qdots into mussels (white squares n = 4). Beakers with only mussel shells are black squares (n = 2). c) PEG-Qdots in water during depuration. After exposure, mussels were washed in SW and placed in new beakers with fresh SW.

Following termination of the exposures, levels of Cd were measured in the hemolymph, digestive gland, and the remaining carcass at exposure termination (24 h) and after 72 h depuration. Approximately 25% of the total Cd dose that was initially in the exposure water partitioned to the digestive gland, while very little (1-2%) remained in the carcass (Figure 5-9). While the levels of Cd partitioning to the carcass represent a fraction similar to that observed for Fe (both were <4%), the fraction of Cd retained within the digestive gland is markedly reduced (25% versus >90% for Cd and Fe, respectively). Unlike the case of the FeOxNPs where we accounted for >90% of the added Fe mass within the *M. galloprovincialis* tissue (primarily the digestive gland), we accounted for only 25-27% of the Cd mass initially added to the system via PEG-Qdots. One possible explanation for the missing Cd is that while PEG-Qdots were filtered

and cleared from the water column, they may have been largely excreted in the feces of *M. galloprovincialis* test organisms prior to termination of the uptake phase of the exposure. We cannot test this hypothesis, however, as fecal material was not recovered and analyzed for Cd content in our study. Using radioisotopic techniques other researchers have shown that *M. galloprovincialis* rapidly eliminated foodborne ^{109}Cd in fecal pellets.⁴⁰ Related studies performed with other *Mytilus* species, *M. edulis*, *M. trossulus*, and *M. californianus*, present conflicting results suggesting that metal uptake and release kinetics, particularly for Cd, can vary considerably across species of *Mytilus*.⁴¹

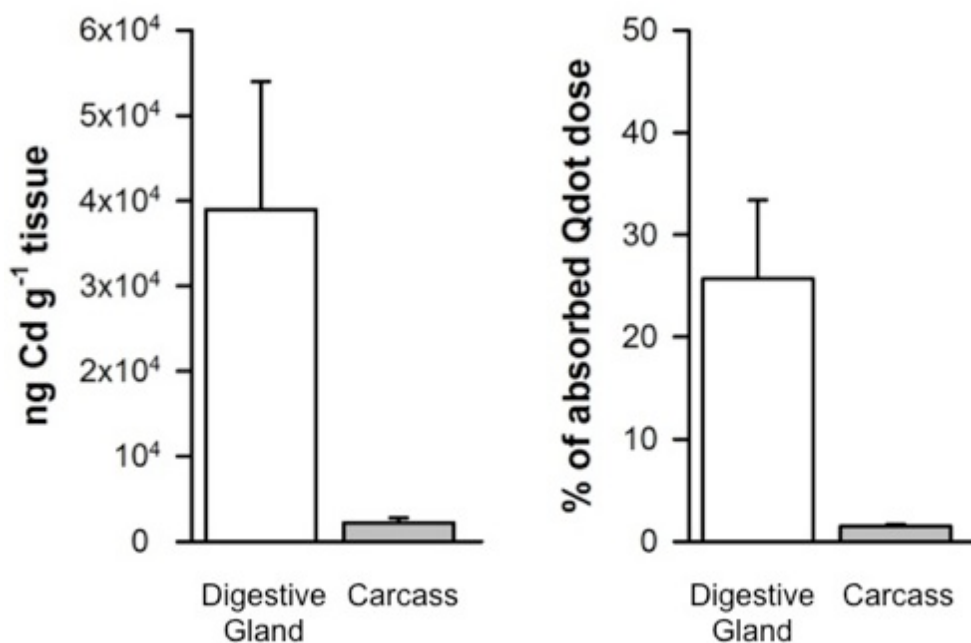


Figure 5-9. (left) PEG-Qdots in the digestive gland and remaining carcass after 72 h depuration. (right) % of PEG-Qdots in the tissue relative to the total loss of Cd from the exposure beaker.

Figure 5-10 shows depuration of Cd from the hemolymph upon exposure termination and after 24 and 72 h depuration. Most notable from these data is that upon termination, Cd levels in

hemolymph are nearly 100 times less than those measured for Fe (4 ng Cd mL⁻¹ versus 400 ng Fe mL⁻¹—Figures 5-10 and 5-5b, respectively). After 24 h depuration, Cd levels in hemolymph have decreased by nearly 60%, but remain near this level for the duration of the assay, indicating only minimal elimination beyond this point.

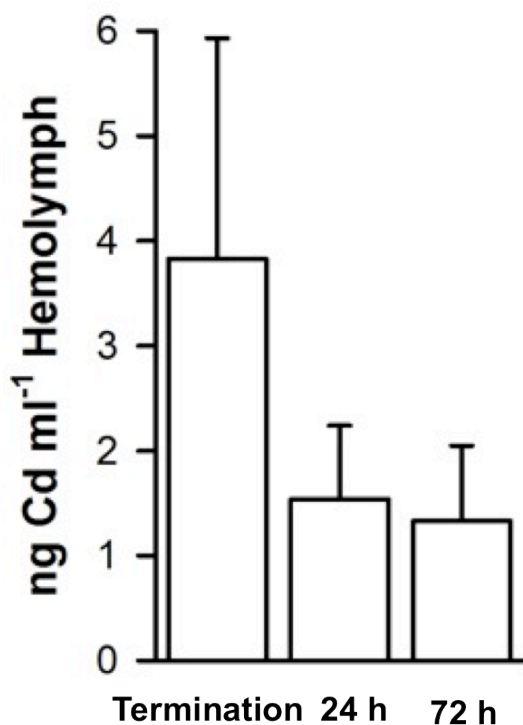


Figure 5-10. Depuration of Cd measured in hemolymph upon exposure termination and after 24 and 72 h depuration in fresh SW.

Despite comparable doses via water column exposures, the disproportionately high accumulation of PEG-FeOxNP relative to PEG-Qdot (in terms of measured Fe and Cd levels) may be attributable in part to the fact that Fe is an essential element with relatively low toxicity in waters of circumneutral pH,⁴² whereas Cd is widely regarded as a non-essential or trace

element with high toxicity.⁴³ Many species of marine and freshwater bivalves have evolved cellular detoxification mechanisms that facilitate the elimination of Cd and similar toxic metals.⁴²

Summary. In summary, mussels rapidly accumulated all MetNPs investigated during the present work through filtering activity. Surface functionalization with PEG prolonged stability of MetNPs in high ionic-strength filtered seawater test media, and facilitated the assessment of particle clearance by filtering mussels. Extended mixing of FeNP with humic acid minimally increased stability of FeNP in seawater, yet aggregation of HA-FeNP was evident based on dramatic decreases in Fe water column concentration-time profiles. Interestingly, aggregation of HA-FeNP coupled with mussel filtering accelerated the removal of Fe from the water column, implying that the bioavailability of some MetNPs can increase, at least temporarily, after environmental release and subsequent growth of MetNP aggregates to size regimes (e.g., micron-scale) more accessible to filter-feeding bivalves. Disposition studies indicated that the digestive gland was the predominant site of storage for all MetNPs after absorption by mussels with little evidence of MetNP migration to other organ systems.

5.5 Acknowledgments

We are grateful for funding support from the US Department of Energy National Security Internship Program, the Virginia Tech/National Science Foundation EIGER/IGERT program, and the Virginia Tech Institute for Critical Technology and Applied Science. We thank A. Bunn, A. Miracle, and J. Wood for assistance with data collection, analysis, and interpretation. This research was supported in part by the U. S. Department of Energy under contract DE-AC06-76RLO 1830 with Battelle PNNL.

5.6 References

1. Friedrichs, S.; Schulte, J., Environmental, health and safety aspects of nanotechnology - implications for the R&D in (small) companies. *Science and Technology of Advanced Materials* **2007**, 8, (1-2), 12-18.
2. Hood, E., Nanotechnology: looking as we leap. *Environmental Health Perspectives* **2004**, 112, (13), A740-A749.
3. Bruchez, M.; Moronne, M.; Gin, P.; Weiss, S.; Alivisatos, A. P., Semiconductor nanocrystals as fluorescent biological labels. *Science* **1998**, 281, (5385), 2013-2016.
4. Nohynek, G. J.; Lademann, J.; Ribaud, C.; Roberts, M. S., Grey goo on the skin? Nanotechnology, cosmetic and sunscreen safety. *Critical Reviews in Toxicology* **2007**, 37, (3), 251-277.
5. Yantasee, W.; Warner, C. L.; Sangvanich, T.; Addleman, R. S.; Carter, T. G.; Wiacek, R. J.; Fryxell, G. E.; Timchalk, C.; Warner, M. G., Removal of heavy metals from aqueous systems with thiol functionalized superparamagnetic nanoparticles. *Environmental Science and Technology* **2007**, 41, 5114-5119.
6. Moore, K.; Pantoya, M. L., Combustion of environmentally altered molybdenum trioxide nanocomposites. *Propellants Explosives Pyrotechnics* **2006**, 31, (3), 182-187.
7. Wagner, J. B.; Othman, N. D.; Su, D. S.; Hamid, S. B. A.; Schlogl, R., Characterization of nanostructured binary molybdenum oxide catalyst precursors for propene oxidation. *Journal of Microscopy-Oxford* **2006**, 223, 216-219.
8. Chen, G.; White, P., The mutagenic hazards of aquatic sediments: a review. *Mutation Research/Reviews in Mutation Research* **2004**, 567, (2-3), 151-225.
9. Rainbow, P. S., Trace metal concentrations in aquatic invertebrates: why and so what? *Environmental Pollution* **2002**, 120, (3), 497-507.
10. Sericano, J. L., The Mussel Watch approach and its applicability to global chemical contamination monitoring programmes. *International Journal of Environment and Pollution* **2000**, 13, (1-6), 340-350.
11. Marigomez, I.; Soto, M.; Cajaraville, M. P.; Angulo, E.; Giamberini, L., Cellular and subcellular distribution of metals in molluscs. *Microscopy Research and Technique* **2002**, 56, (5), 358-392.
12. Ballan-Dufrançais, C.; Jeantet, A. Y.; Coulon, J., Cytological features of mussels (*Mytilus edulis*) in situ exposed to an effluent of the titanium dioxide industry. *Annales de l'Institut Oceanographique* **1990**, 66, (1-2), 1-18.

13. Ballan-Dufrancais, C.; Jeantet, A. Y.; Feghali, C.; Halpern, S., Physiological features of heavy-metal storage in bivalve digestive cells and amebocytes - Epma and factor analysis of correspondences. *Biology of the Cell* **1985**, 53, (3), 283-292.
14. Chassardbouchaud, C.; Boutin, J. F.; Hallegot, P.; Galle, P., Chromium uptake, distribution and loss in the mussel *Mytilus edulis* - a structural, ultrastructural and microanalytical study. *Diseases of Aquatic Organisms* **1989**, 7, (2), 117-136.
15. Coulon, J.; Truchet, M.; Martoja, R., Chemical features of mussels (*Mytilus edulis*) in situ exposed to an effluent of the titanium dioxide industry. *Annales de l Institut Oceanographique* **1987**, 63, (2), 89-99.
16. George, S. G.; Pirie, B. J. S.; Calabrese, A.; Nelson, D. A., Biochemical and ultrastructural observations of long-term silver accumulation in the mussel, *Mytilus edulis*. *Marine Environmental Research* **1986**, 18, (4), 255-265.
17. Vogt, G.; Qunitio, E. T., Accumulation and excretion of metal granules in the prawn, *Penaeus monodon* exposed to water-borne copper, lead, iron and calcium. *Aquatic Toxicology* **1994**, 28, (3-4), 223-241.
18. Cheung, M. S.; Wang, W. X., Influence of subcellular metal compartmentalization in different prey on the transfer of metals to a predatory gastropod. *Marine Ecology Progress Series* **2005**, 286, 155-166.
19. Rainbow, P. S.; Geffard, A.; Jeantet, A. Y.; Smith, B. D.; Amiard, J. C.; Amiard-Triquet, C., Enhanced food-chain transfer of copper from a diet of copper-tolerant estuarine worms. *Marine Ecology Progress Series* **2004**, 271, 183-191.
20. Wallace, W. G.; Luoma, S. N., Subcellular compartmentalization of Cd and Zn in two bivalves, II: significance of trophically available metal (TAM). *Marine Ecology Progress Series* **2003**, 257, 125-137.
21. Berry, C. C.; Curtis, A. S. G., Functionalisation of magnetic nanoparticles for applications in biomedicine. *Journal of Physics D- Applied Physics* **2003**, 36, (13), R198-R206.
22. Gref, R.; Minamitake, Y.; Peracchia, M. T.; Trubetskoy, V.; Torchilin, V.; Langer, R., Biodegradable long-circulating polymeric nanospheres. *Science* **1994**, 263, (5153), 1600-1603.
23. Owens, D. E.; Peppas, N. A., Opsonization, biodistribution, and pharmacokinetics of polymeric nanoparticles. *International Journal of Pharmaceutics* **2006**, 307, (1), 93-102.
24. Moghimi, S. M.; Szebeni, J., Stealth liposomes and long circulating nanoparticles: critical issues in pharmacokinetics, opsonization and protein-binding properties. *Progress in Lipid Research* **2003**, 42, (6), 463-478.

25. Hull, M.; Chaurand, P.; Rose, J.; Auffan, M.; Bottero, J.; Jones, J.; Schultz, I.; Vikesland, P., Filter-feeding bivalves store and biodeposit colloiddally stable gold nanoparticles. *Environmental Science and Technology* **2011**, Epub ahead of print.
26. Smith, L. C.; Azumi, K.; Nonaka, M., Complement systems in invertebrates: the ancient alternative and lectin pathways. *Immunopharmacology* **1999**, 42, (1-3), 107-120.
27. Haye, J. M.; Santschi, P. H.; Roberts, K. A.; Ray, S., Protective role of alginic acid against metal uptake by American oyster (*Crassostrea virginica*). *Environmental Chemistry* **2006**, 3, (3), 172-183.
28. Rickerby, D.; Morrison, M., Nanotechnology and the environment: a European perspective. *Science and Technology of Advanced Materials* **2007**, 8, (1-2), 19-24.
29. Pagenkopf, G. K., Gill surface interaction model for trace-metal toxicity to fishes - role of complexation, pH, and water hardness. *Environmental Science and Technology* **1983**, 17, (6), 342-347.
30. Reinfelder, J. R.; Fisher, N. S., The assimilation of elements ingested by marine copepods. *Science* **1991**, 251, (4995), 794-796.
31. Lyon, R.; Taylor, M.; Simkiss, K., Ligand activity in the clearance of metals from the blood of the crayfish (*Austropotamobius pallipes*). *Journal of Experimental Biology* **1984**, 113, 19-27.
32. Lewis, D. F. V.; Dobrota, M.; Taylor, M. G.; Parke, D. V., Metal toxicity in two rodent species and redox potential: evaluation of quantitative structure-activity relationships. *Environmental Toxicology and Chemistry* **1999**, 18, (10), 2199-2204.
33. Newman, M. C.; McCloskey, J. T., Predicting relative toxicity and interactions of divalent metal ions: Microtox(R) bioluminescence assay. *Environmental Toxicology and Chemistry* **1996**, 15, (3), 275-281.
34. Tantara, C. P.; Newman, M. C.; McCloskey, J. T.; Williams, P. L., Predicting relative metal toxicity with ion characteristics: *Caenorhabditis elegans* LC50. *Aquatic Toxicology* **1997**, 39, (3-4), 279-290.
35. Walker, J. D.; Enache, M.; Dearden, J. C., Quantitative cationic-activity relationships for predicting toxicity of metals. *Environmental Toxicology and Chemistry* **2003**, 22, (8), 1916-1935.
36. Schultz, I. R.; Hayton, W. L., Interspecies scaling of the bioaccumulation of lipophilic xenobiotics in fish: an example using trifluralin. *Environmental Toxicology and Chemistry* **1999**, 18, (7), 1440-1449.

37. Ward, J.; Kach, D., Marine aggregates facilitate ingestion of nanoparticles by suspension-feeding bivalves. *Marine Environmental Research* **2009**, 68, (3), 137-142.
38. Silvester, N.; Sleight, M., Hydrodynamic aspects of particle capture by *Mytilus*. *Journal of the Marine Biological Association of the United Kingdom* **1984**, 64, 859-879.
39. Riisgard, H., Efficiency of particle retention and filtration rate in 6 species of Northeast American bivalves. *Marine Ecology Progress Series* **1988**, 45, 217-223.
40. Fisher, N.; Teysse, J.; Fowler, S.; Wang, W., Accumulation and retention of metals in mussels from flood and water: a comparison under field and laboratory conditions. *Environmental Science and Technology* **1996**, 30, 3232-3242.
41. Lares, M.; Orians, K., Differences in Cd elimination from *Mytilus californianus* and *Mytilus trossulus* soft tissues. *Environmental Pollution* **2001**, 112, 201-207.
42. Bebianno, M.; Langston, W., Cadmium induction of metallothionein synthesis in *Mytilus galloprovincialis*. *Comparative Biochemistry and Physiology Part C: Comparative Pharmacology* **1992**, 103, (1), 79-85.
43. Green, D.; Williams, K.; Pascoe, D., The acute and chronic toxicity of cadmium to different life history stages of the freshwater crustacean *Asellus aquatic* (L). *Archives of Environmental Contamination and Toxicology* **1986**, 15, 465-471.

Chapter 6. Conclusions

6.1 Conclusions and Implications

Given their colloidal stability in high ionic-strength matrices, functionalized MetNPs are anticipated to be persistent aquatic contaminants. Despite their potential environmental significance, the persistence of surface-functionalized MetNPs as individually-stabilized nanoparticles in aquatic environments is largely unknown. Further, few studies have investigated the fundamental factors influencing MetNP uptake and fate/transport processes in ecologically susceptible aquatic biota, such as filter-feeding bivalves, which ingest and accumulate a broad range of dissolved- and particulate-phase contaminants.

We investigated the influence of size and surface chemistry on the uptake and biological fate and transport of MetNPs in two species of filter-feeding bivalves: *C. fluminea*, a freshwater clam, and *M. galloprovincialis*, a marine mussel. An important objective of our work was to prepare well-characterized nanoparticle test suspensions and apply complementary characterization techniques that facilitated understanding of nanoparticle disposition in exposure media and within bivalve test organisms and biodeposited feces. This comprehensive approach was warranted since much of the published literature offers limited understanding of the relationships between physicochemical properties of nanoscale particles and their uptake by aquatic biota. In particular, many published studies fail to describe the persistence of nanoscale test materials in exposure media as individually stabilized nanoscale particles. In theory, the existence of nanoscale materials as either individually-stabilized, monodisperse particles or as clusters or aggregates of varying size and shape would likely have significant effects on the nature of nanoparticle interactions with biological and environmental systems. Thus, our research objectives were focused on investigating the validity of four hypotheses relevant to

understanding MetNP aggregation in aquatic systems and the subsequent uptake and fate of MetNPs by filter-feeding bivalves. Findings and conclusions stemming from each of our four hypothesis statements are presented in the following sections.

Hypothesis 1. Integrated characterization techniques are necessary to evaluate the stability and persistence of MetNP suspensions in aquatic media, and to effectively interpret the bioavailability of nanoscale particles to filter-feeding biota. In studies of MetNP aggregation to date, researchers typically use time-resolved dynamic light scattering (TR-DLS) to measure increases in hydrodynamic diameter over time, with UV-Vis spectroscopy being employed sparingly to verify the size or concentration of the pristine MetNP, or to confirm the presence of the classic red-shift of the localized surface plasmon resonance (LSPR) band known to occur when MetNPs aggregate.¹⁻⁹ As we demonstrate in **Chapter 2**, the integration of DLS and UV-Vis measurements provides an important technique to characterize two distinct aggregation regimes that occur when optically-active MetNPs become destabilized. *Regime 1* represents the initial decrease in interparticle spacing that occurs as the double layer surrounding individual MetNPs contracts and monomers begin to interact and form clusters.¹⁰ *Regime 1* is most effectively characterized through kinetic UV-Vis measurements and the subsequent calculation of the ratio of the absorbance at the primary LSPR band of the pristine MetNP suspension relative to the absorbance at a second LSPR band that occurs and intensifies as interparticle spacing decreases.¹⁰ *Regime 2* occurs when interparticle spacing has effectively reached '0' nm and cluster growth becomes the dominant process. *Regime 2* can be suitably characterized using TR-DLS to measure hydrodynamic diameter over time, which, as noted above, has been the primary means to evaluate this process in previous studies.^{2, 11}

Employing the complementary techniques of TR-DLS and TR-UV-Vis allows us to develop a

unique approach for quantifying the persistence of optically-active MetNPs as NNI-defined ‘nanoscale’ materials, which we discuss in detail in **Chapter 3**. Understanding the persistence of NPs, particularly MetNPs, in environmental systems is critical to environmental risk assessments of nanoscale materials and subsequent determinations of unique nanoscale hazards. During the earliest stages of aggregation—which we define as *Regime 1* in **Chapter 2**—UV-Vis measurements provide a rapid and cost-efficient means for characterizing the destabilization and subsequent loss of nano-unique properties (e.g., LSPR behavior) of MetNP suspensions before such events can be measured by DLS. The rate at which these properties are lost can be used to define and relate the persistence of MetNPs as individually-stabilized nanoparticles with different surface coatings and upon addition to media of varying chemical composition. Additionally, the integration of both UV-Vis and DLS measurements can enhance understanding of MetNP disposition in exposure media, and provide critical insights about the effects of MetNP size, shape, aggregation state, and stability, on uptake, toxicity, and biological fate/transport in exposures with aquatic test organisms (such as we report in **Chapter 4**).

Hypothesis 2. Uptake of MetNPs by filter-feeding bivalves should be modulated by particle size, with larger particles being cleared from suspension more rapidly than smaller particles. Previous studies have shown that micron-sized particles are cleared from suspension by filter-feeding bivalves relatively rapidly (within 30 minutes to a few hours).¹²⁻¹⁶ Particle clearance rates are typically positively related to initial particle concentration and particle diameter. However, studies of sub-micron particles are lacking in the peer-reviewed literature. We observed that clearance rates for bovine serum albumin-stabilized gold nanoparticles (BSA-AuNP) were positively related to initial AuNP concentration in the range of 2 to 8 mg L⁻¹ (as [Au]). These results are consistent with experimental results showing that filter-feeding bivalves

increase filtration rates to maximize particle clearance. Further, in support of our hypothesis that the positive relationship between particle size and clearance rate observed for micron-scale particles would extend into the nano domain, we observed that 46 nm BSA-AuNP were cleared from suspension by *C. fluminea* more rapidly than particles of either 7.8 or 15 nm in diameter. In contrast to these results, however, the marine mussel *M. galloprovincialis* cleared polymer-coated FeOxNPs and Qdots ranging in size from 2-50 nm diameter equally rapidly. Collectively, these results suggest that clearance rates for MetNPs by filter-feeding bivalves are expected to be a function of numerous factors including MetNP composition, concentration, primary particle diameter, dispersing media, and bivalve species.

Hypothesis 3. Biological fate and transport of MetNPs in filter-feeding bivalves should follow established bivalve models and localize primarily in the gills, mantle, and digestive gland; non-compartmental toxicokinetic models may be useful for predicting MetNP fate in bivalves. In clearance studies with both *C. fluminea* and *M. galloprovincialis*, we observed that MetNPs partitioned primarily to the digestive tract and/or the digestive gland. These results were confirmed using three different techniques to analyze metals in tissue and organ systems including x-ray fluorescence microscopy (μ -XRF), inductively coupled plasma emission mass spectroscopy (ICP-MS), and optical emission spectroscopy (ICP-OES). In general, there was little evidence suggesting that MetNPs were translocated to other organ systems, but in-depth histological and electron microscopy studies with additional MetNP types varying in diameter and surface coating are required to better understand the potential for MetNPs to pass through the digestive epithelium and accumulate in biological compartments beyond the digestive system. Nevertheless, our observation that three different types of MetNPs partitioned primarily to the digestive glands of two different bivalve species is compelling evidence that the biological

fate of MetNPs in bivalves is likely to be similar to that observed for dissolved metals. Finally, although we cannot yet definitively conclude that non-compartmental toxicokinetic models are useful for predicting MetNP fate in bivalves, we have collected a preliminary dataset with *M. galloprovincialis* (Chapter 5) that can be used to inform future efforts to develop such models.

Hypothesis 4. Biodeposition will factor prominently in the transference of MetNPs from the water column to the benthic zone, and patterns of uptake and biodeposition may be useful for biomonitoring of AuNP as well as other nanoparticles discharged to aquatic systems. Biodeposition, or the biologically-mediated process of transferring particulates suspended in the water column to subsurface environments, is an important ecological function performed by filter-feeding bivalves. To our knowledge, no other studies have investigated the influence of biodeposition on the environmental fate and transport of NPs in general and MetNPs in particular. Further, no studies have examined the effects of bivalve digestive processes on the physicochemical properties of biodeposited MetNPs versus pristine MetNPs. Our results, which clearly show that AuNPs were concentrated in *C. fluminea* feces in both free and aggregated forms, demonstrate that biodeposition is likely to factor significantly in transferring physicochemically-altered forms of MetNPs from the water column to the benthic zone. The ultimate biological fate and toxicity of these altered MetNPs to benthic-dwelling organisms is largely unknown, but is expected to differ from the fate and toxicity of pristine MetNPs. Finally, the observation that colloidally stable MetNPs can be accumulated and concentrated by filter-feeding bivalves in tissue and feces indicates that in addition to their long-held utility as indicators of dissolved chemical pollutants, bivalves should serve as useful biomonitors for MetNPs discharged to aquatic systems. Further studies are needed, however, to investigate such utility at environmentally relevant concentrations (e.g., $<100 \mu\text{g L}^{-1}$).

6.2 A Simplified Conceptual Framework for Bivalve-Mediated Uptake and Fate/ Transport of MetNPs

Figure 6-1 presents a simplified conceptual framework for the bivalve-mediated uptake and fate/transport of MetNPs in aquatic systems. Based upon our studies and a synthesis of the current literature,^{2, 11} dependent on their surface chemistry and the chemistry of aquatic receiving systems, pristine MetNPs will either aggregate rapidly ('Unstable') or remain suspended in the water column for indefinite periods ('Stable'). Aggregation and settling processes of MetNPs and numerous other colloidal materials have been studied extensively (e.g., **Chapter 2**), and a range of parameters including our proposed metric for measuring the persistence of optically-active MetNPs as individually-stabilized nanoparticles (**Chapter 3**) can be used to describe these processes quantitatively. While unstable MetNPs are likely to be transferred from the water column to subsurface environments via gravitational settling, some researchers suggest that aggregate formation and a subsequent increase in particle size is likely to accelerate clearance of nanoscale particles by filter-feeding bivalves.¹⁷ Although our work cannot directly confirm or refute such claims, our observation that clearance rates were positively related to primary particle diameter (d_{TEM}) indirectly supports this possibility. More importantly, however, our results confirm that bivalves are capable of filtering and removing from the water column individually stabilized nanoscale particles (**Chapters 4 and 5**). Once filtered by bivalves, MetNP are expected to partition primarily to the digestive gland and digestive tract, where they are altered physicochemically and excreted in feces. Thus, biodeposition is expected to be an important mechanism whereby MetNPs are transferred by filter-feeding bivalves from the water column to subsurface environments.

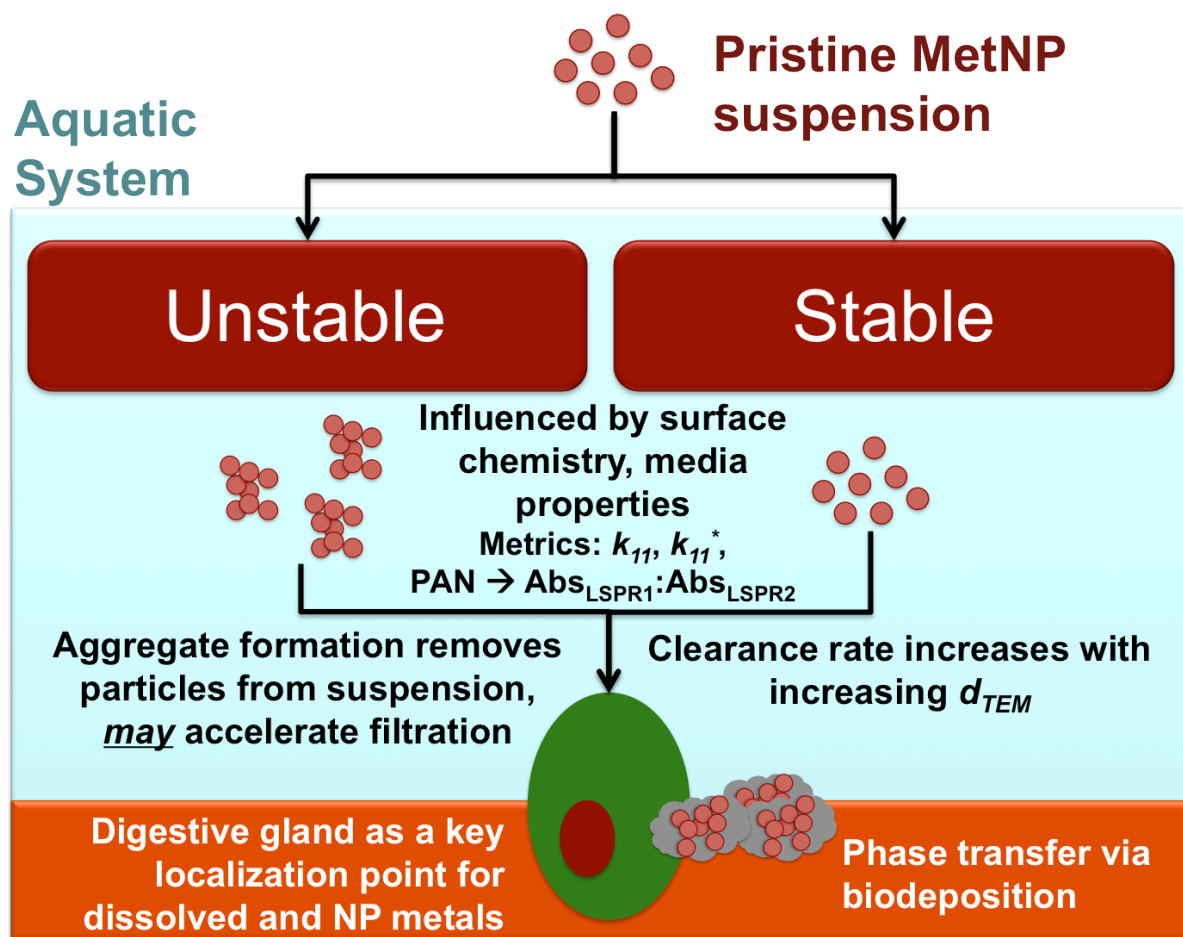


Figure 6-1. Simplified conceptual framework for bivalve-mediated uptake and fate/transport of MetNPs in aquatic systems.

6.3 Summary and Future Work

In summary, the present study describes a comprehensive approach to prepare and rigorously characterize MetNP test suspensions to facilitate fundamental examinations of nanoparticle uptake and fate/transport processes in freshwater and marine bivalves. We demonstrate the importance of accurately characterizing test suspensions in order to better understand MetNP persistence as individually-stabilized nanoparticles within aquatic test media, and define an

optical-activity metric suitable for quantifying and comparing the persistence of variable MetNP formulations as National Nanotechnology Initiative (NNI) definable nanoscale materials. We also show that individually-stabilized MetNPs of variable elemental composition, particle diameter, and surface coating are accessible to bivalves in both freshwater and marine environments. Clearance rates for MetNPs are positively related to the diameter and initial concentration of MetNP suspensions. The observed size-dependence of particle filtration rates facilitates ‘size-selective biopurification’ of particle suspensions with nanoscale resolution, and may have applicability in future sustainable nanomanufacturing processes. Filtered MetNPs are retained for extended periods post-exposure primarily within the bivalve digestive tract and digestive gland, but migration to other organ systems was not observed. Clusters of MetNPs were recovered in concentrated form from excreted feces, suggesting that biotransformation and biodeposition processes will play an important role in transferring MetNPs from the water column to benthic environments.

Prospects for future research have been noted in the preceding sections, but in general should include the following:

- Studies of MetNP uptake, fate/transport should be expanded to include smaller particle diameters (e.g., < 5 nm) and additional surface coatings to determine the potential for MetNPs to cross the digestive epithelium and partition to organ systems beyond the digestive gland and digestive tract.
- Although the MetNPs investigated in the current study were not acutely toxic to test organisms (i.e., survivorship was 100% in all experiments), studies are needed to assess the sublethal toxicity of MetNPs.
- Physicochemical transformation (e.g., aggregation, dissolution) of MetNPs that could

potentially occur during filtering, digestion, and subsequent biodeposition should be characterized more extensively to facilitate understanding of the potential impacts of biodeposited MetNPs on other benthic-dwelling organisms.

- The utility of bivalves for biomonitoring of NPs in general and MetNPs in particular should be investigated at environmentally-relevant concentrations below 100 $\mu\text{g L}^{-1}$.

6.4 References

1. Burns, C.; Spendel, W.; Puckett, S.; Pacey, G., Solution ionic strength effect on gold nanoparticle solution color transition. *Talanta* **2006**, 69 (4), 873-876.
2. Chen, K.; Mylon, S.; Elimelech, M., Aggregation kinetics of alginate-coated hematite nanoparticles in monovalent and divalent electrolytes. *Environmental Science & Technology* **2006**, 40 (5), 1516-1523.
3. Diegoli, S.; Manciuola, A.; Begum, S.; Jones, I.; Lead, J.; Preece, J., Interaction between manufactured gold nanoparticles and naturally occurring organic macromolecules. *Science of the Total Environment* **2008**, 402, 51-61.
4. He, T.; Wan, J.; Tokunaga, T., Kinetic stability of hematite nanoparticles: the effect of particle sizes. *Journal of Nanoparticle Research* **2008**, 10, 321-332.
5. Kim, T.; Lee, C.-H.; Joo, S.-W.; Lee, K., Kinetics of gold nanoparticle aggregation: experiments and modeling. *Journal of Colloid and Interface Science* **2008**, 318, 238-243.
6. Laaksonen, T.; Ahonen, P.; Johans, C.; Kontturi, K., Stability and electrostatics of mercaptoundecanoic acid capped gold nanoparticles with varying counter-ion sizes. *ChemPhysChem* **2006**, 7 (10), 2143-2149.
7. Liu, J.; Hurt, R. H., Ion release kinetics and particle persistence in aqueous nano-silver colloids. *Environmental Science & Technology* **2010**, 44, 2169-2175.
8. MacCuspie, R., Colloidal stability of silver nanoparticles in biologically relevant conditions. *Journal of Nanoparticle Research* **2010**, 13 (7), 2893-2908.
9. MacCuspie, R.; Allen, A.; Hackley, V., Dispersion stabilization of silver nanoparticles in synthetic lung fluid studied under in situ conditions. *Nanotoxicology* **2010**, 5 (2), 140-156.
10. Zhong, Z.; Patskovskyy, S.; Bouvrette, P.; Luong, J.; Gedanken, A., The surface chemistry of Au colloids and their interactions with functional amino acids. *Journal of Physical Chemistry B* **2004**, 108 (13), 4046-4052.

11. Mylon, S.; Chen, K.; Elimelech, M., Influence of natural organic matter and ionic composition on the kinetics and structure of hematite colloid aggregation: implications to iron depletion in estuaries. *Langmuir* **2004**, 20, 9000-9006.
12. Mohlenberg, F.; Riisgard, H. U., Efficiency of particle retention in 13 species of suspension feeding bivalves. *Ophelia* **1978**, 17, 239-246.
13. Riisgard, H., Efficiency of particle retention and filtration rate in 6 species of Northeast American bivalves. *Marine Ecology Progress Series* **1988**, 45, 217-223.
14. Silverman, H.; Achberger, E. C.; Lynn, J. W.; Dietz, T. H., Filtration and utilization of laboratory-cultured bacteria by *Dreissena polymorpha*, *Corbicula fluminea*, and *Carunculina texasensis*. *Biological Bulletin* **1995**, 189, 308-319.
15. Silverman, H.; Lynn, J. W.; Beninger, P. G.; Dietz, T. H., The role of the latero-frontal cirri in particle capture by the gills of *Mytilus edulis*. *Biological Bulletin* **1999**, 197, 368-376.
16. Silvester, N. R.; Sleight, M. A., Hydrodynamic aspects of particle capture by *Mytilus*. *Journal of the Marine Biological Association of the UK* **1984**, 64, 859-879.
17. Ward, J. E.; Kach, D. J., Marine aggregates facilitate ingestion of nanoparticles by suspension-feeding bivalves. *Marine Environmental Research* **2009**, 68, 137-142.